

Nonlinear Optics of Split-Ring Resonators and their Application as a Thermal Detector

Zur Erlangung des akademischen Grades eines
DOKTORS DER NATURWISSENSCHAFTEN
der Fakultät für Physik des
Karlsruher Instituts für Technologie (KIT)

genehmigte

Dissertation

von

Dipl.-Phys. Fabian Bernd Peter Niesler
aus Pforzheim

Tag der mündlichen Prüfung: 19. Oktober 2012

Referent: Prof. Dr. Martin Wegener

Korreferent: Prof. Dr. Kurt Busch

Contents

1	Introduction	1
2	Basics of Optics	5
2.1	From Maxwell's Equations ...	5
2.2	... to Light Propagation	7
2.3	Metal Optics	9
2.3.1	The Drude Free-Electron Model	9
2.4	Optics of Dielectrics	11
2.5	Optics of Small Metal Particles	12
2.6	Nonlinear Optics	15
2.6.1	Symmetry Properties	16
2.6.2	Nonlinear Optics of Dielectrics - The Anharmonic-Oscillator Model	18
2.6.3	Nonlinear Optics of Metals	21
2.6.3.1	The Nonlinear Drude Model	22
2.7	Optical Metamaterials	24
2.7.1	The Split-Ring Resonator	24
2.7.1.1	Excitation Configurations	26
2.7.1.2	Higher-Order Resonances	27
3	Materials and Methods	29
3.1	Sample Fabrication	29
3.2	Sample Characterization	33
3.2.1	Linear Optical Characterization	33

CONTENTS

4	Nonlinear Optical Experiments	35
4.1	SHG from Split-Ring Resonators on GaAs Substrate	36
4.1.1	Nonlinear Optical Characterization	38
4.1.2	Experimental Results and Discussion	41
4.1.3	Conclusions	45
4.2	SHG Spectroscopy on Split-Ring-Resonator Arrays	46
4.2.1	Sample Fabrication and Linear Optical Characterization	46
4.2.2	Nonlinear Optical Characterization	47
4.2.3	Experimental Results and Discussion	50
4.2.4	Conclusions	54
4.3	Collective Effects in Second-Harmonic Generation from Split-Ring-Resonator Arrays	55
4.3.1	Sample Fabrication and Linear Optical Characterization	55
4.3.2	Experimental Results and Discussion	56
4.3.3	Conclusions	64
5	Thermal Detectors	65
5.1	Thermal Model	67
5.1.1	Heat Exchange Mechanisms	68
5.1.2	Thermal Capacity	71
6	Metamaterial Metal Bolometer	73
6.1	Basics of Metal Bolometers	74
6.2	Thermal Characterization of the Bolometer	76
6.3	Experimental Setup	79
6.4	Experimental Results	83
6.4.1	Conclusions	89
7	Conclusions and Outlook	91
	References	95

Publications

Parts of this work have already been published...

...in peer reviewed scientific journals:

- F.B.P. Niesler, N. Feth, S. Linden, J. Niegemann, J. Gieseler, K. Busch, and M. Wegener, “Second-harmonic generation from split-ring resonators on a GaAs substrate,” *Opt. Lett.* **34**, 1997 (2009).
- F.B.P. Niesler, N. Feth, S. Linden, and M. Wegener, “Second-harmonic optical spectroscopy on split-ring-resonator arrays,” *Opt. Lett.* **36**, 1533 (2011).
- F.B.P. Niesler, J.K. Gansel, S. Fischbach, and M. Wegener, “Metamaterial metal-based bolometers,” *Appl. Phys. Lett.* **100**, 203508 (2012).
- S. Linden, F.B.P. Niesler, J. Förstner, Y. Grynko, T. Meier, and M. Wegener, “Collective Effects in Second-Harmonic Generation from Split-Ring-Resonator Arrays,” *Phys. Rev. Lett.* **109**, 015502 (2012).

...at scientific conferences (only own presentations):

- F.B.P. Niesler, S. Linden, N. Feth, and M. Wegener, “Second-harmonic spectroscopy on split-ring-resonator arrays,” in “Conference on Lasers and Electro-Optics / Quantum Electronics and Laser Science Conference (San Jose, USA),” talk QTuA (2009).
- F.B.P. Niesler and M. Wegener, “Metamaterial bolometers,” in “Conference on Lasers and Electro-Optics / Quantum Electronics and Laser Science Conference (San Jose, USA),” talk QM3F (2012).

- F.B.P. Niesler, S. Linden, J. Förstner, Y. Grynko, T. Maier, and M. Wegener, “Collective effects in second-harmonic generation from split-ring-resonator arrays,” in “Conference on Lasers and Electro-Optics / Quantum Electronics and Laser Science Conference (San Jose, USA),” talk QTh3E (2012).

Additional work on other topics has been published in peer reviewed scientific journals:

- N. Feth, S. Linden, M.W. Klein, M. Decker, F.B.P. Niesler, Y. Zeng, W. Hoyer, J. Liu, S.W. Koch, J.V. Moloney, and M. Wegener, “Second-harmonic generation from complementary split-ring resonators,” *Opt. Lett.* **33**, 1975 (2008).

1

Introduction

A precise control of light propagation is one of the main driving forces of research in the field of optics. The performance of optical elements for the alteration of light propagation is determined by the optical properties of the materials available. However, all natural existing optical materials are limited to only control the electric-field component of the light. The development of metamaterials in recent years made a new material class available that allows the control of the electric- as well as the magnetic-field component of the light independently. This new degree of freedom allows in principle the design of novel and unprecedented optical devices.

Metamaterials are artificial composite materials constructed from fundamental building blocks. These blocks are arranged in a lattice with a period smaller than the corresponding wavelength of light that they were synthesized for. The optical properties of the material are given by the geometrical shape of the blocks and the materials used, often a combination of metals and dielectrics. Its optical behavior can well be described by effective material parameters such as an electric permittivity ϵ and a magnetic permeability μ .

The theoretical framework for this material class was founded by Veselago in 1968 [1] who studied the qualities of a, at that time purely fictitious, material which exhibits a negative magnetic- and electric response $\epsilon, \mu < 0$. He discovered dramatically different propagation characteristics of light within this material such as a negative index of refraction. These novel optical phenomena sparked further research. In 2000, the concept of a perfect lens was proposed by Pendry [2] as a possible application for a negative refractive index material.

1. INTRODUCTION

On the way to a practical realization of such a material, a design of the fundamental building block providing a magnetic response had to be found. In 1999, Pendry *et al.* [3] came up with the split-ring resonator (SRR). The basic design consists of a metal ring with a small gap. Light impinging on this structure induces an oscillating ring current which generates an oscillating magnetic dipole moment. A negative index of refraction for a periodic arrangement of single SRRs was demonstrated in 2001 by Shelby *et al.* [4] in the microwave region. In later years, this concept was then brought to the optical domain through a miniaturization of the SRRs down to dimensions on the nanometer scale using advanced nano-fabrication techniques [5, 6].

Metamaterials are also the foundation for transformation optics [7]. By spatially varying the effective material parameters ϵ, μ within the material, the flow of light can be controlled. It can even be bent around objects to render them invisible. The idea of the electromagnetic cloak goes back to work of Pendry *et al.* [8] and Leonhard [9]. Through a vast improvement of 3D fabrication techniques, this concept could be experimentally demonstrated at optical wavelengths only recently [10].

Current research in the field of metamaterials is characterized by the search for applications [11]. For example, perfect absorbers, neither transmitting or reflecting light in a certain wavelength range, have been demonstrated [12]. This concept was then adapted for sensing and detection applications [13, 14]. Thermal emitters, which provide a tailored emission spectrum [15, 16] also build up on this idea. An investigation of the nonlinear optical properties of metamaterial structures is of scientific as well as technological interest. The research in this area is motivated by the idea of developing efficient frequency converters or optical switches using metamaterials, which outperform today's state-of-the-art technologies. To reach this ambitious goal, a deeper understanding of the underlying physics is needed which can only be achieved through a sufficient amount of experimental data, providing a test-ground for theory.

The experiments presented in this thesis aim to provide a contribution to the progress in the field of linear and nonlinear optics of metamaterials and their applications. The nonlinear optical experiments are focussed on second-harmonic generation of gold split-ring resonator arrays as a paradigmatic building block of

metamaterials . Second-harmonic optical spectroscopy on these arrays, using a sophisticated optical setup with a tunable light source, provides a deeper insight on the role of the different resonances of the SRR as well as the spacing between individual SRR on the generation of frequency doubled light.

In addition, this thesis presents a thermal detector based on a modified splitting resonator structure. This metamaterial metal-based bolometer is fabricated and fully experimentally characterized. The proof of concept adds up to the list of possible applications using metamaterials.

Outline of this Thesis

The first part of this thesis deals with experiments on second-harmonic generation from split-ring resonator arrays. In the second part, the experimental demonstration of a metamaterial metal-based bolometer is presented.

In chapter 2, the thesis starts with a presentation of the basics of linear and nonlinear optics. These are provided to the reader for a deeper understanding of the experimental results in the later chapters. In addition, the working-horse of this thesis, the split-ring resonator is elucidated.

Chapter 3 discusses the methods used for the fabrication and the linear optical characterization of all samples in this thesis.

The experimental details and results for the nonlinear optical experiments on SRR arrays are presented in chapter 4. In the first part, we study the interaction of an SRR array with a substrate possessing a strong optical second-order nonlinearity and compare the results with a theoretical modeling. In the second part, second-harmonic-generation spectroscopy on gold SRR arrays fabricated on glass substrates is presented. A tunable light-source in combination with lithographic tuning of the individual SRR within the arrays was used to provide a deeper insight onto the role of the individual resonances on the second-harmonic generation. The third part finally studies the role of the spacing between individual SRRs within an array on the second-harmonic generation intensity. The experimental result is compared to numerical calculations.

In chapter 5, the basic working principles of thermal detectors are illustrated to provide the basis for the later presentation of the metamaterial metal-bolometer concept in chapter 6. A full experimental characterization of the fabricated bolometer is presented and compared to numerical calculations. This work

1. INTRODUCTION

is intended to provide a proof of concept of a thermal detector with build-in spectral and polarization filters.

The thesis is finally concluded in chapter 7.

2

Basics of Optics

In this chapter, the basics of linear and nonlinear optics are treated. We start by introducing the Maxwell equations for a basic description of light-matter interaction. Then, the models for the linear optical response of metals and dielectrics are presented. In a next step, an introduction to nonlinear optics and the nonlinear optical response of metals and dielectrics is presented. Finally, the split-ring resonator and its optical properties are introduced.

2.1 From Maxwell's Equations ...

To start our journey into the interaction of light with matter, we begin with the set of macroscopic Maxwell equations describing electromagnetic phenomena in general. They read

$$\nabla \cdot \mathbf{D} = \rho_{\text{ext}}, \quad (2.1)$$

$$\nabla \cdot \mathbf{B} = 0, \quad (2.2)$$

$$\nabla \times \mathbf{E} = -\frac{\partial \mathbf{B}}{\partial t}, \quad (2.3)$$

$$\nabla \times \mathbf{H} = \mathbf{j}_{\text{ext}} + \frac{\partial \mathbf{D}}{\partial t}, \quad (2.4)$$

with the macroscopic fields \mathbf{D} (the dielectric displacement), \mathbf{E} (the electric field), \mathbf{H} (the magnetic field) and \mathbf{B} (the magnetic induction), the external charge density ρ_{ext} and the current density \mathbf{j}_{ext} .

When the electric and magnetic fields \mathbf{E} , \mathbf{H} act on materials, they can induce or reorient electric and magnetic dipoles. The polarization \mathbf{P} describes the electric

2. BASICS OF OPTICS

dipole moment per unit volume inside the material, while the magnetization \mathbf{M} depicts the magnetic moment per unit volume. The constitutive relations account for the presence of materials and have the form

$$\mathbf{D} = \epsilon_0 \mathbf{E} + \mathbf{P}, \quad (2.5)$$

$$\mathbf{H} = \frac{1}{\mu_0} \mathbf{B} - \mathbf{M}, \quad (2.6)$$

with the electric permittivity ϵ_0 and magnetic permeability μ_0 of the vacuum.

In the following, we consider a linear response of the materials, and the fields \mathbf{P} , \mathbf{M} are connected with the corresponding response functions through

$$\mathbf{P}(\mathbf{r}, t) = \int \epsilon_0 \bar{\chi}_e(\mathbf{r} - \mathbf{r}', t - t') \mathbf{E}(\mathbf{r}', t') dt' d^3 r', \quad (2.7)$$

$$\mathbf{M}(\mathbf{r}, t) = \int \mu_0 \bar{\chi}_m(\mathbf{r} - \mathbf{r}', t - t') \mathbf{H}(\mathbf{r}', t') dt' d^3 r'. \quad (2.8)$$

Here, \mathbf{r} denotes the spatial coordinate, and the electric and magnetic susceptibility, $\bar{\chi}_e$ and $\bar{\chi}_m$ respectively, represent second-rank tensors.

The above general form of the susceptibilities can be simplified if special material properties are fulfilled. In isotropic media, the tensors reduce to scalar quantities because the dipoles are oriented parallel or antiparallel to the applied fields. Homogenous media with a spatially local response remove the tensors dependence on the space coordinate. No explicit time dependence and causality results in a simplified representation

$$\mathbf{P}(\mathbf{r}, t) = \epsilon_0 \int_{-\infty}^t \chi_e(t - t') \mathbf{E}(\mathbf{r}, t') dt', \quad (2.9)$$

$$\mathbf{M}(\mathbf{r}, t) = \mu_0 \int_{-\infty}^t \chi_m(t - t') \mathbf{M}(\mathbf{r}, t') dt'. \quad (2.10)$$

We now do a Fourier transformation of the above equations to go from the time domain to the frequency domain. Finally, the expressions

$$\mathbf{P}(\omega) = \epsilon_0 \chi_e(\omega) \mathbf{E}(\omega), \quad (2.11)$$

$$\mathbf{M}(\omega) = \mu_0 \chi_m(\omega) \mathbf{H}(\omega), \quad (2.12)$$

are obtained and the material equations 2.8 can be rewritten as

$$\mathbf{D} = \epsilon_0 (1 + \chi_e(\omega)) \mathbf{E} = \epsilon_0 \epsilon(\omega) \mathbf{E}, \quad (2.13)$$

$$\mathbf{B} = \mu_0 (1 + \chi_m(\omega)) \mathbf{H} = \mu_0 \mu(\omega) \mathbf{H}, \quad (2.14)$$

with the relative electric permittivity $\epsilon_r = \epsilon(\omega)$ and the relative permeability $\mu_r = \mu(\omega)$, which describe the response of the material.

In usual textbooks, a magnetization of materials through electromagnetic fields at optical frequencies is often neglected, as natural existing materials show no magnetic response for wavelengths in the visible. The excitement about optical metamaterials is the idea of engineering values for ϵ_r, μ_r to change the materials response to light waves, leading to unusual optical phenomena.

2.2 ... to Light Propagation

So far we have only processed the foundation of the interaction of magnetic and electric fields with matter. But light as an electromagnetic wave is still hidden in Maxwell's equations. To reveal the traveling wave as a solution to the Maxwell equations, we can rewrite them in the form

$$\left(\nabla^2 - \mu_0 \epsilon_0 \frac{d^2}{dt^2} \mu_r \epsilon_r \right) \mathbf{E} = 0, \quad (2.15)$$

$$\left(\nabla^2 - \mu_0 \epsilon_0 \frac{d^2}{dt^2} \mu_r \epsilon_r \right) \mathbf{B} = 0. \quad (2.16)$$

By using the ansatz for a plane wave for the electric and the magnetic field

$$\mathbf{E}(\mathbf{r}, t) = \mathbf{E}_0 e^{i(\mathbf{k}\mathbf{r} - \omega t)} + c.c., \quad (2.17)$$

$$\mathbf{B}(\mathbf{r}, t) = \mathbf{B}_0 e^{i(\mathbf{k}\mathbf{r} - \omega t)} + c.c., \quad (2.18)$$

with *c.c.* denoting the complex conjugate, we get the dispersion relation

$$\mathbf{k} \cdot \mathbf{k} = \mu(\omega) \epsilon(\omega) \omega^2 \mu_0 \epsilon_0 = \tilde{n}(\omega)^2 \frac{\omega^2}{c_0^2} = \tilde{n}^2(\omega) \mathbf{k}_0^2, \quad (2.19)$$

which connects the frequency ω of the wave with the wave vector \mathbf{k} through the vacuum speed of light $c_0 = 1/\sqrt{\mu_0 \epsilon_0}$ and the complex refractive index

$$\tilde{n}(\omega) = \sqrt{\epsilon(\omega) \mu(\omega)}. \quad (2.20)$$

In most naturally occurring materials, the magnetic response at optical frequencies can be neglected and setting $\mu_r = 1$ is justified. The behavior of the refractive index is therefore solely determined by the complex permittivity $\epsilon(\omega) = \epsilon_{Re}(\omega) + i\epsilon_{Im}(\omega)$ through

$$\tilde{n}(\omega) = \sqrt{\epsilon(\omega)_{Re} + i\epsilon(\omega)_{Im}} \quad (2.21)$$

2. BASICS OF OPTICS

with

$$\epsilon_{\text{Re}} = n^2 - \kappa^2 \quad (2.22)$$

$$\epsilon_{\text{Im}} = 2n\kappa \quad (2.23)$$

$$n^2 = \frac{\epsilon_{\text{Re}}}{2} + \frac{1}{2} \sqrt{\epsilon_{\text{Re}}^2 + \epsilon_{\text{Im}}^2}, \quad (2.24)$$

$$\kappa = \frac{\epsilon_{\text{Im}}}{2n} \quad (2.25)$$

The propagation of light is obviously strongly affected by the refractive index, as it directly influences the wavevector \mathbf{k} . The wave vector for a plane wave propagating in z -direction has the form

$$\mathbf{k}_z = \frac{\omega}{c_0} \tilde{n} \hat{\mathbf{e}}_z = \frac{\omega}{c_0} (n + i\kappa) \hat{\mathbf{e}}_z \quad (2.26)$$

where $\hat{\mathbf{e}}_z$ denotes the unit vector in z -direction. For the electrical field of a plane wave 2.18 we then get

$$\mathbf{E}(z, t) = \mathbf{E}_0 \cdot \overbrace{e^{i\omega(n(\omega)z/c_0 - t)}}^{\text{propagation}} \cdot \underbrace{e^{-(\omega\kappa(\omega)z/c_0)}}_{\text{attenuation}}. \quad (2.27)$$

Here we see that the real part $n(\omega)$ of the refractive index determines the wave propagation, while the imaginary part $\kappa(\omega)$ accounts for a attenuation of the wave and is therefore called the extinction coefficient. It is linked to the absorption coefficient α of Beer's law,

$$I(z) = I_0 e^{-\alpha z}. \quad (2.28)$$

It describes the exponential decay of the intensity $I(z)$ of a beam propagation through an absorbing medium along the z -direction. This can be easily seen by using $I(z, t) \propto |\mathbf{E}(z, t)|^2$ on 2.27 and comparing the result with 2.28. We obtain

$$\alpha(\omega) = \frac{2\omega\kappa(\omega)}{c_0}. \quad (2.29)$$

One can define a characteristic length scale on which the intensity of the wave dropped to a value of $1/e$ of its initial intensity. This so called skin depth is given by $\delta_z = 1/\alpha(\omega)$.

2.3 Metal Optics

To describe the optical response of metals, we introduce the Drude free-electron model. We will see that the dielectric function of this model is strongly linked to the electrical conductivity of the metal.

2.3.1 The Drude Free-Electron Model

The model of free electrons is a classical model described in principle by Drude in 1900. Within this model he was able not only to explain the conduction of both, electricity and heat, but also the optical properties of metals. It is based on the following assumptions. First of all, the metal consist of electrons that can move freely. The movement of these conduction electrons is disturbed by instantaneous and uncorelated collision processes with ions and impurities within the metal. The probability of such a collision during a time interval dt is given by dt/τ , where τ describes the relaxation time. An electron-electron interaction process is neglected at all in this model.

The equation of motion for one electron with the mass m_e is given by

$$m_e \frac{d^2}{dt^2} \mathbf{r} + \frac{m_e}{\tau} \frac{d}{dt} \mathbf{r} = -e\mathbf{E}(t), \quad (2.30)$$

where the electric field acts as a driving force. Now we apply a harmonic time dependent field $\mathbf{E}(t) = \mathbf{E}_0 e^{-i\omega t}$ which leads to the solution for the displacement of the electron

$$\mathbf{r}(t) = \frac{e}{m(\omega^2 + i\gamma\omega)} \mathbf{E}(t), \quad (2.31)$$

with $\gamma = 1/\tau$ denoting the collision frequency and $\mathbf{r}(t) = \mathbf{x}_0 e^{-i\omega t}$.

The macroscopic polarization \mathbf{P} is then given as a product of n electrons in the unit volume:

$$\mathbf{P} = -ner = -\frac{ne^2}{m(\omega^2 + i\gamma\omega)} \mathbf{E}. \quad (2.32)$$

The constitutive relation reads

$$\mathbf{D} = \epsilon_0 \left(1 - \frac{\omega_{\text{pl}}^2}{\omega^2 + i\gamma\omega} \right) \mathbf{E}, \quad (2.33)$$

2. BASICS OF OPTICS

with the plasma frequency $\omega_{\text{pl}}^2 = \frac{ne^2}{\epsilon_0 m}$. By comparing this with equation 2.13, we have the dielectric function of the Drude free-electron gas given by

$$\epsilon(\omega) = 1 - \frac{\omega_{\text{pl}}^2}{\omega^2 + i\gamma\omega}. \quad (2.34)$$

We now take a closer look on the current density. The electrical current I is defined as

$$I = \frac{dQ}{dt} \quad (2.35)$$

where Q denotes the amount of charge. The charge density is defined as $j = I/A$ and we get

$$j = -nev_d, \quad (2.36)$$

with v_d denoting the drift velocity of electrons. Writing the equation of motion 2.30 using the impulse $p = m\dot{x}$, we have

$$\dot{p} + \frac{p}{\tau} = -eE_0 e^{-i\omega t}. \quad (2.37)$$

Using the ansatz $p = p_0 \cdot e^{-i\omega t}$, we obtain the solution

$$v_d = \dot{x} = \frac{-e\tau}{m} \frac{1}{1-i\omega\tau} E_0. \quad (2.38)$$

Now we insert this result in equation 2.36 to obtain

$$j = \frac{ne^2\tau}{m} \frac{1}{1-i\omega\tau} E_0 \quad (2.39)$$

$$= \frac{\sigma_0}{1-i\omega\tau} E_0 \quad (2.40)$$

$$= \sigma(\omega) E_0 \quad (2.41)$$

which is Ohm's law with the AC conductivity $\sigma(\omega)$ and DC conductivity $\sigma(0) = \sigma_0$. If we insert this into 2.34, we get

$$\epsilon(\omega) = 1 + i \frac{\sigma(\omega)}{\epsilon_0 \omega}, \quad (2.42)$$

where we see, that the metals dielectric function is linked to its frequency dependent conductivity.

2.4 Optics of Dielectrics

In dielectrics, the electrons are bound to the atomic cores and cannot move freely like in metals. An applied static electric field leads to a deviation of the electrons position from the rest position. The response is therefore different compared to metals, where a static electric field leads to a drift velocity of the electrons. The model of a damped harmonic oscillator (Lorentz oscillator), driven by an external harmonic electric field, is

$$m_e \frac{d^2}{dt^2} \mathbf{r} + m_e \Gamma \frac{d}{dt} \mathbf{r} + m_e \omega_0^2 \mathbf{r} = -e E_0 e^{-i\omega t}, \quad (2.43)$$

where $\Gamma = 1/\gamma$ describes the damping of the electron's movement. The damping factor accounts for an energy loss of the electron due to radiation and electron-phonon interaction. With the same reasoning as for the free-electron model in metals, we get the electric dipole moment per unit volume through multiplying all n electrons

$$\mathbf{P} = -n e \mathbf{r}(t) = \frac{n e^2}{m_e} \frac{1}{\omega_0^2 - \omega^2 - i\Gamma\omega} \mathbf{E}_0 e^{-i\omega t}. \quad (2.44)$$

We get the same result with the plasma frequency ω_{pl}

$$\mathbf{D} = \epsilon_0 \left(1 + \frac{\omega_{pl}^2}{\omega_0^2 - \omega^2 - i\omega\Gamma} \right) \mathbf{E}. \quad (2.45)$$

Now that we have analytical expressions for the response of the material, we will take a closer look on the influence on the propagation of light. We have seen, that the absorption coefficient of the material depends on the imaginary part of the dielectric function.

In figure 2.1 (a) the real and imaginary parts of the dielectric function for metals, as obtained by the free electron model, are plotted. For frequencies below the plasma frequency, $\omega \ll \omega_{pl}$, the imaginary part of the dielectric function leads to an absorption of the electromagnetic wave. In this regions, the light wave is attenuated on the length-scale of the skin depth. The absorption coefficient 2.29 is

$$\alpha(\omega) = \sqrt{\frac{2\omega_{pl}^2 \tau \omega}{c_0}}. \quad (2.46)$$

2. BASICS OF OPTICS

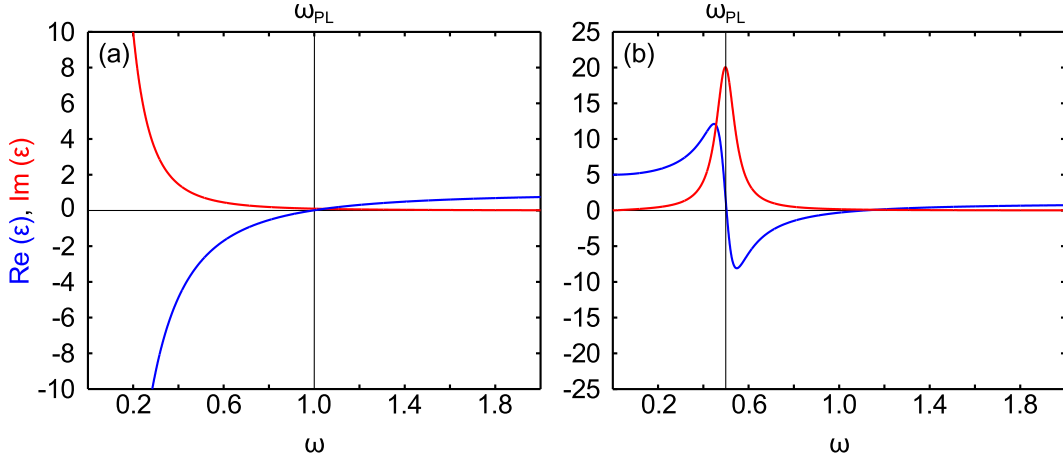


Figure 2.1: Dielectric functions in the Drude and Lorentz model - Both plots show the real (blue line) and imaginary (red line) part of the dielectric function. In (a), permittivity for metals, as obtained from the free electron model, is depicted. In (b), a dielectric described with the damped oscillator model is presented. For both figures, a plasma frequency of $\omega_{pl} = 1$ and a damping constant of $\gamma = 0.1$ is chosen. The resonance frequency in (b) is $\omega_0 = 0.5$.

For frequencies above the plasma frequency $\omega \gg \omega_{pl}$, the real part of the dielectric function dominates. Here, a wave propagation through the metal is possible and they become transparent.

With the same reasoning, dielectrics in figure 2.1 (b) show the same behavior for frequencies above and below the resonance frequency $\omega \gg \omega_0$ and $\omega \ll \omega_0$. In this region, they are transparent to light waves. But near the resonance $\omega \approx \omega_0$, the dominant imaginary part of the dielectric function leads to a strong absorption of waves.

2.5 Optics of Small Metal Particles

In the previous chapters, we have modeled the reaction of electrons in bulk matter to an external electric field. When bulk metals are drastically reduced in size and reach dimensions smaller than the wavelength of light, their optical response can no longer be described by the Drude free-electron model. In this case the electromagnetic wave has a constant spatial phase along the particle and the electric field can be assumed as static (quasi-static approximation). The electromagnetic

wave shifts the electrons inside the particle relative to the fixed positive ions of the lattice. This leads to a charge separation resulting in a restoring force acting on the deviated electrons. The equation of motion for the electrons is now given by a driven harmonic oscillator, as described before with the Lorentz oscillator model. An external field in resonance with the eigenfrequency of the particle then leads to a collective electron oscillation, called particle plasmon.

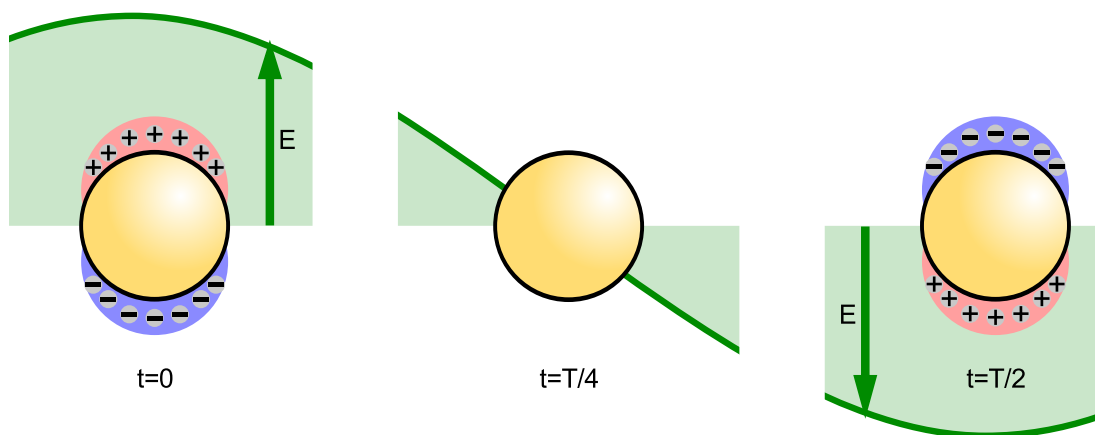


Figure 2.2: Particle plasmon - Illustration of a particle plasmon excited by an sinusoidal oscillating external electric field with the period T .

Within the quasi static approximation, analytical expressions for spherical and elliptical particles can be found. For a metal sphere, the polarizability $\alpha(\omega)$ describing the electric dipole moment of the particle $\mathbf{p} = \epsilon_0 \epsilon_{\mathbf{m}} \alpha \mathbf{E}$, is given by [17]

$$\alpha(\omega) = 4\pi a^3 \frac{\epsilon(\omega) - \epsilon_s}{\epsilon(\omega) + 2\epsilon_s}, \quad (2.47)$$

where a denotes the radius of the sphere. $\epsilon(\omega)$ is the metals dielectric function and ϵ_s describes the dielectric constant of the surrounding material. The resonance condition is fulfilled when the denominator $|\epsilon + 2\epsilon_s|$ is minimized. For a vanishing imaginary part of the dielectric constant $\Im[\epsilon]$, this corresponds to the Frölich condition:

$$\Re[\epsilon(\omega)] = -2\epsilon_s. \quad (2.48)$$

When we now use the dielectric function as obtained from the Drude model, we can deduce the resonance condition for a metal sphere as

$$\omega_0 = \frac{\omega_{\text{pl}}}{\sqrt{-(2\epsilon_s + 1)}}. \quad (2.49)$$

2. BASICS OF OPTICS

Here we see that the resonance position strongly depends on the plasma frequency ω_{pl} of the metal and the dielectric constant ϵ_s of the surrounding material but it does not depend from the size of the nano-sphere. This makes metal nanoparticles an ideal tool for sensing applications, as any change of the surrounding dielectric leads to an altered resonance frequency of the particle that can be monitored optically [18].

For elliptical particles, the polarizability becomes a tensor accounting for the different geometry of the particle. The expressions for the polarizability along the particle's principal axes $i \in 1, 2, 3$ is given by [17, 19]

$$\alpha_i = V \frac{\epsilon(\omega) - \epsilon_m}{\epsilon_m + F_i(\epsilon(\omega) - \epsilon_m)}, \quad (2.50)$$

with V representing the volume of the ellipsoid. Here the Frölich condition does give a size dependent resonance frequency of the particle due to the geometry factor F_i .

If the particle size no longer satisfies the quasi static approximation, an analytical solution can still be found in the special case of spherical particles. The so-called Mie theory is a more general expression for the optical properties of metal nanoparticles [19, 20], but will not be discussed in greater detail here. For arbitrarily shaped particles, numerical modeling of the optical properties has been used.

Another inherent feature connected with the plasmonic resonances of metal nanoparticles is the enhancement of the near field around the particle. The intensity of the local field $I_{\text{loc}} = |E_{\text{loc}}|$ compared to the incoming field $I_0 = |E_0|$ differs by the frequency dependent enhancement factor $L(\omega)$ [17]

$$I_{\text{loc}} = L(\omega) \cdot I_0 = L(\omega)_{\text{SP}} L_{\text{LR}} I_0. \quad (2.51)$$

Two physical effects are responsible for the field enhancement. The so-called lightning rod effect is responsible for the frequency independent contribution L_{LR} and is strongly depending on the geometrical shape of the particle. The electric field on the surface of a perfect conductor points perpendicular to the surface normal, therefore leading to a concentration of the electromagnetic field to areas of sharp edges or tips. The frequency dependent part $L(\omega)_{\text{SP}}$ is due to the resonant

excitation of localized surface plasmons in the structure and essentially resembles the polarizability α . For a spherical particle in vacuum this reads

$$L(\omega)_{SP} \propto \frac{\epsilon(\omega) - 1}{\epsilon(\omega) + 2}. \quad (2.52)$$

The frequency dependent enhancement can also be expressed by the quality factor of the damped linear oscillator with the resonance frequency ω_0

$$Q = \frac{\omega_0}{\gamma}, \quad (2.53)$$

where γ describes the damping of the oscillator. The quality factor is also known as the resonant amplification factor of the oscillator and describes the enhancement of the oscillation amplitude of a driven oscillator system with respect to the driving amplitude. This corresponds to the local-field enhancement in the case of a particle plasmon.

2.6 Nonlinear Optics

The wave theory of light is based on the superposition principle. Light beams which travel in a linear medium can pass through one another without disturbing each other. However, in nonlinear media things are a bit different rendering Huygen's principle of superposition invalid.

The description of the material's response to electromagnetic fields in the former chapters is only valid in the case of low field intensities. In the presence of very strong optical fields, the dielectric polarization now responds nonlinearly to the electric field of light. This leads to an interaction of optical fields mediated by the material. In contrast to linear optics, the fields are now no longer linearly superimposable. With the invention of the laser, making strong electrical fields experimentally accessible, these effects became observable in the lab [21].

To describe this behavior theoretically, we can expand the dielectric polarization density as a Taylor series in the electric field

$$\mathbf{P}(\omega) = \epsilon_0 \chi^{(1)}(\omega, \omega_1) \mathbf{E}(\omega_1) \quad (2.54)$$

$$+ \epsilon_0 \chi^{(2)}(\omega, \omega_1, \omega_2) \mathbf{E}(\omega_1) \mathbf{E}(\omega_2) \quad (2.55)$$

$$+ \epsilon_0 \chi^{(3)}(\omega, \omega_1, \omega_2, \omega_3) \mathbf{E}(\omega_1) \mathbf{E}(\omega_2) \mathbf{E}(\omega_3) \quad (2.56)$$

$$+ \dots, \quad (2.57)$$

2. BASICS OF OPTICS

where the $\chi^{(i)}$, $i > 1$ denote the nonlinear optical susceptibilities of i -th order and represent tensors of rank $i + 1$.

Splitting of the polarization in its linear and nonlinear parts

$$\mathbf{P}(\omega) = \mathbf{P}_{\text{linear}}(\omega) + \mathbf{P}_{\text{nonlinear}}(\omega) \quad (2.58)$$

then leads to a wave equation representation in the frequency domain [22]

$$\nabla^2 \mathbf{E}(\omega) + \frac{\omega^2 \epsilon(\omega)}{c^2} \mathbf{E}(\omega) = \frac{\omega^2}{c^2} \mathbf{P}_{\text{nonlinear}}(\omega). \quad (2.59)$$

The nonlinear polarization on the right hand side of this inhomogenous wave equation acts as a driving force.

2.6.1 Symmetry Properties

We will take a closer look on the symmetry properties of the $\chi^{(2)}$ tensor, but similar arguments can be found for the tensors of higher orders. In the most general case for the nonlinear polarization of second order,

$$P_i^{(2)}(\omega_n + \omega_m) = \epsilon_0 \sum_{jk} \sum_{(nm)} \chi_{ijk}^{(2)}(\omega_n + \omega_m, \omega_n, \omega_m) E_j(\omega_n) E_k(\omega_m), \quad (2.60)$$

the nonlinear susceptibility consists of 324 different complex numbers, that need to be defined. Fortunately, by using symmetry arguments, this number can be greatly reduced.

The fact that the polarization as well as the electric fields represent physical measurable quantities and therefore must be real, results in

$$P_i^{(2)}(-\omega_n - \omega_m) = P_i(\omega_n + \omega_m)^*, \quad (2.61)$$

$$E_j(-\omega_n) = E_j(\omega_n)^*, \quad (2.62)$$

$$E_k(-\omega_m) = E_k(\omega_m)^*, \quad (2.63)$$

that leads to equal tensor components

$$\chi_{ijk}^{(2)}(-\omega_n - \omega_m, -\omega_n, -\omega_m) = \chi_{ijk}^{(2)}(\omega_n + \omega_m, \omega_n, \omega_m)^*. \quad (2.64)$$

In addition, the order of the fields on the right hand side of 2.60 is arbitrary. This intrinsic permutation symmetry gives

$$\chi_{ijk}^{(2)}(\omega_n + \omega_m, \omega_n, \omega_m) = \chi_{ikj}^{(2)}(\omega_n + \omega_m, \omega_m, \omega_n). \quad (2.65)$$

When the material can be considered lossless, two more symmetries can be applied. We then can require the nonlinear susceptibility to be real which expresses as

$$\chi_{ijk}^{(2)}(\omega_n + \omega_m, \omega_n, \omega_m) = \chi_{ijk}^{(2)}(\omega_n + \omega_m, \omega_n, \omega_m), \quad (2.66)$$

and the full permutation symmetry leads then to a free interchange of the frequency arguments as long as the corresponding spatial coordinates are interchanged as well:

$$\chi_{jik}^{(2)}(\omega_n + \omega_m, \omega_n, \omega_m) = \chi_{kij}^{(2)}(\omega_m, \omega_n + \omega_m, -\omega_n). \quad (2.67)$$

In case of a neglectable frequency dispersion of $\chi^{(2)}$ we can even permute the spatial indices and frequency arguments independently, which is called the Kleinman symmetry.

The occurrence of nonlinear optical effects strongly depends on the symmetry class of the material, because the crystal symmetry also influences the symmetry of its physical properties. This fact is known as the Neumann's principle. It states, that a tensor, which represents a physical property, is invariant under symmetry operations which leave the crystal itself invariant [23]. Spatial symmetry therefore can further reduce the number of independent tensor elements.

The transformation behavior for the components m_{lmn} of a tensors of rank three is

$$m'_{ijk} = \sum_l \sum_m \sum_n A_{il} A_{jm} A_{kn} m_{lmn}, \quad (2.68)$$

where A denotes the transformation matrix. We now apply this rule to the $\chi^{(2)}$ tensor of an inversion symmetric medium. In this case, the symmetry operation is

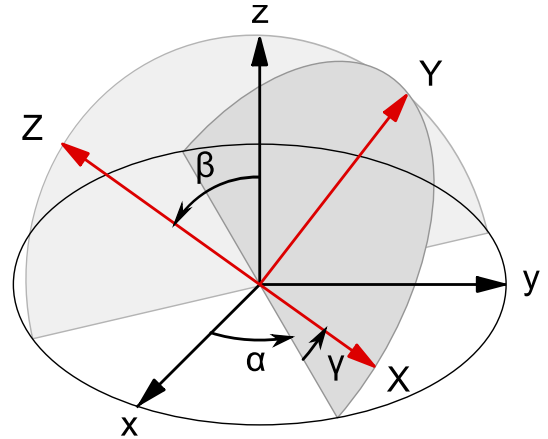


Figure 2.3: Euler Angles - Illustration of the Euler angles to get from an initial coordinate system xyz (black arrows) to a rotated system XYZ (red arrows).

2. BASICS OF OPTICS

given by the transformation matrix with the only nonzero elements $A_{11} = A_{22} = A_{33} = -1$. This results in vanishing tensor components, $(\chi_{ijk}^{(2)})' = -\chi_{ijk}^{(2)} = 0$. Therefore, nonlinear optical effects of second order, or more general of even order, are not found in inversion symmetric media.

When the crystal is rotated in the laboratory frame of reference, the transformation matrix can be obtained using the Euler angles which describe the crystals rotation. The matrix is given by

$$A(\alpha, \beta, \gamma) = \begin{pmatrix} \cos \alpha & \sin \alpha & 0 \\ -\sin \alpha & \cos \alpha & 0 \\ 0 & 0 & 1 \end{pmatrix} \quad (2.69)$$

$$\cdot \begin{pmatrix} 1 & 0 & 0 \\ 0 & \cos \beta & -\sin \beta \\ 0 & \sin \beta & \cos \beta \end{pmatrix} \quad (2.70)$$

$$\cdot \begin{pmatrix} \cos \gamma & -\sin \gamma & 0 \\ \sin \gamma & \cos \gamma & 0 \\ 0 & 0 & 1 \end{pmatrix} \quad (2.71)$$

using the set of angles α, β, γ according to figure 2.3. This principle will be used to interpret the experimental results in chapter 4.1.

2.6.2 Nonlinear Optics of Dielectrics - The Anharmonic-Oscillator Model

We have already seen that the Lorentz model is adequate in describing the optical properties of dielectric materials. Therefore it is obvious to extend this model to describe the nonlinear response to find an expression for the nonlinear optical susceptibility.

The equation of motion for the electron is described using a nonlinear restoring force $F_{\text{nonlinear}}$ caused by an anharmonic potential. The equation of motion can then be written in a generic form

$$\ddot{x} + 2\gamma\dot{x} - F_{\text{restoring}} = -eE(t)/m. \quad (2.72)$$

To describe the potential mathematically, we use a Taylor series expansion of the restoring force with respect to the displacement x of the electron [22].

$$U(x) = - \int F_{\text{restoring}} dx = \frac{1}{2}m\omega_0^2 x^2 + \frac{1}{3}max^3 - \frac{1}{4}mbx^4 \quad (2.73)$$

With this representation, we have restricted ourselves to displacements that are small enough to not include higher terms in the series for an adequate description of the potential and $a > b$.

The first term represents the harmonic potential and reproduces the restoring force $F_{\text{restoring}} = -m\omega_0^2 x^2$ used in equation 2.43. The latter terms account for the deviation of the potential from the perfect parabolic shape and are responsible for the nonlinear restoring force.

To find the solutions to 2.72 we first have to consider the exact form of the potential which depends on the symmetry of the medium. In case of centrosymmetric media, it is required that $U(x) = U(-x)$, therefore leading to $a = 0$ and $b \neq 0$. The lowest nonlinear optical susceptibility in this case is of third order and nonlinear susceptibilities of even order vanish. In contrast, non-centrosymmetric media, described by $U(x) = -U(-x)$, possess even and odd orders for the nonlinear optical susceptibility.

The equation of motion for non-centrosymmetric media is then

$$\ddot{x} + \gamma\dot{x} + \omega_0^2 x + ax^2 = -eE(t)/m \quad (2.74)$$

and the electric field, acting on the electron is assumed to be two plane waves of different frequencies, described by

$$E(t) = E_1 e^{-i\omega_1 t} + E_2 e^{-i\omega_2 t} + c.c. \quad (2.75)$$

where *c.c.* denotes the complex conjugate. To solve the equation of motion 2.74 we use perturbation theory, known from quantum mechanics, where we replace $E(t)$ with $\lambda E(t)$, with $0 \leq \lambda \leq 1$ as an expansion parameter. We now have

$$\ddot{x} + \gamma\dot{x} + \omega_0^2 x + ax^2 = -\lambda eE(t)/m \quad (2.76)$$

and we will try to find solutions using the power series ansatz

$$x = \lambda x^{(1)} + \lambda^2 x^{(2)} + \lambda^3 x^{(3)} + \dots \quad (2.77)$$

Insertion and sorting by powers of the expansion parameter results in the equations

$$\ddot{x}^{(1)} + \gamma\dot{x}^{(1)} + \omega_0^2 x^{(1)} = -eE(t)/m \quad (2.78)$$

$$\ddot{x}^{(2)} + \gamma\dot{x}^{(2)} + \omega_0^2 x^{(2)} + a(x^{(1)})^2 = 0 \quad (2.79)$$

$$\ddot{x}^{(3)} + \gamma\dot{x}^{(3)} + \omega_0^2 x^{(3)} + 2ax^{(1)}x^{(2)} = 0 \quad (2.80)$$

$$\vdots \quad (2.81)$$

2. BASICS OF OPTICS

The first equation reproduces the familiar solution from the Lorentz oscillator

$$x^{(1)}(t) = x^{(1)}(\omega_1)e^{-i\omega_1 t} + x^{(1)}(\omega_2)e^{-i\omega_2 t} + c.c. \quad (2.82)$$

with amplitudes

$$x^{(1)}(\omega_j) = -\frac{e}{m} \frac{E_j}{D(\omega_j)} \quad (2.83)$$

and the complex denominator function $D(\omega_j) = \omega_0^2 - \omega_j^2 - i\omega_j\gamma$. Using the relation

$$P^{(1)}(\omega_j) = \epsilon_0 \chi^{(1)}(\omega_j) E(\omega_j) = -Nex^{(1)}(\omega_j), \quad (2.84)$$

we reproduce the linear susceptibility

$$\chi^{(1)}(\omega_j) = \frac{N(e^2/m)}{\epsilon_0 D(\omega_j)}. \quad (2.85)$$

To now solve the equation for the second order correction term $x^{(2)}(t)$, we have to insert the equation for $x^{(1)}(t)$ into 2.79. This leads to an inhomogenous differential equation, where the source term on the right hand side describes second-harmonic generation ($2\omega_1$ and $2\omega_2$), sum- ($\omega_1 + \omega_2$) and difference- ($\omega_1 - \omega_2$) frequency generation as well as optical rectification for zero frequency.

For example, second-harmonic generation is described by the equation

$$\ddot{x}^{(2)} + \gamma\dot{x}^{(2)} + \omega_0^2 x^{(2)} = \frac{-a(eE_1/m)^2 e^{-2i\omega_1 t}}{D^2(\omega_1)} \quad (2.86)$$

that can be solved by using the ansatz $x^{(2)}(t) = x^{(2)}(2\omega_1)e^{-2i\omega_1 t}$. With this ansatz, we obtain

$$x^{(2)}(2\omega_1) = \frac{-a(e/m)^2 E_1^2}{D(2\omega_1)D^2(\omega_1)} \quad (2.87)$$

which gives us an expression for the nonlinear susceptibility describing second-harmonic generation by using

$$P^{(2)}(2\omega_1) = \epsilon_0 \chi^{(2)}(2\omega_1, \omega_1, \omega_1) E(\omega_1)^2 = -Nex^{(2)}(2\omega_1). \quad (2.88)$$

We finally obtain

$$\chi^{(2)}(2\omega_1, \omega_1, \omega_1) = \frac{N(e^3/m^2)a}{\epsilon_0 D(2\omega_1)D^2(\omega_1)}. \quad (2.89)$$

So far, we have only considered the nonlinear effects of second order. From the above equation, we again see that for an observation of these effects, a nonvanishing a and therefore a non-centrosymmetric medium is required. Effects of third order can be obtained in an analogous way by solving the equation for $x^{(3)}$ but will not be presented here. The interested reader might consult reference [22].

2.6.3 Nonlinear Optics of Metals

Optical second-harmonic generation from a metal surface was first discovered in 1965 [24] and extensively studied experimentally in the years after. Early work on the theoretical side was based on the free-electron model formulated by Jha [25]. Within this model, the nonlinear polarization varying at twice the fundamental frequency ω has the form

$$P_{\text{NL}}^{(2)} = \underbrace{\alpha(E_1 \times H_1)}_{\text{bulk term}} + \underbrace{\beta E_1 \nabla \cdot E_1}_{\text{surface term}} \quad (2.90)$$

where E_1 and H_1 represent the electric and magnetic fields at the fundamental frequency and the coefficients α and β have been determined as [26]

$$\alpha = \frac{ie^3 n}{4m_e^2 e c \omega^3}, \quad (2.91)$$

$$\beta = \frac{e}{8\pi m_e \omega_{\text{pl}} \omega^2}, \quad (2.92)$$

where m_e and e are the mass and the charge of an electron, and n is the electron density. The plasma frequency is $\omega_{\text{pl}} = \sqrt{4\pi n e^2 / m_e}$. The first term is the magnetic dipole term and represents a contribution from within the volume of the metal originating from the Lorentz force. In contrast, the second term is the magnetic quadrupole term and is nonzero only near the surface of the metal.

While this model could provide some estimates of the contributing mechanisms, its mathematical flaws and limitations have been discussed by several authors [27, 28, 29, 30]. For example, the permittivity $\epsilon(\omega)$ within this model is given by [26]

$$\epsilon(\omega) = 1 - \frac{e^2 n}{m \omega^2}. \quad (2.93)$$

This real and negative permittivity is not a valid description for real metals. Because the permittivity depends on the electron density n , it shows a transition from a negative value within the metal volume to a positive value $\epsilon(\omega) = 1$ in the vacuum where the electron density is zero. In the transition region at the surface the permittivity vanishes at the boundary. Here, the normal component of the electric field tends to infinity due to the continuity relations. This is a clearly unphysical behavior. Rudnick and Stern [29] also pointed out the need for a more careful analysis of the metal-vacuum interface.

2. BASICS OF OPTICS

In the 1980s, a hydrodynamic model relevant for nonlinear optical effect in metals was formulated by Sipe *et al.* [31]. Later, it was slightly modified by Schaich and Corvi [32]. The main idea of describing the electrons through an electron density $n_e(\mathbf{r}, t)$ and a velocity field $\mathbf{v}_e(\mathbf{r}, t)$ is also the basis for more recent theories and numerical calculation schemes for the nonlinear response of metals, metal particles, and metamaterial structures [33, 34, 35].

2.6.3.1 The Nonlinear Drude Model

The nonlinear Drude model, as described by Liu *et al.* [34], can be viewed as a generalization of the linear Drude model to the nonlinear case. The electrons within the metal are treated as a fluid, described by the electron density $n_e = n_e(\mathbf{r}, t)$ and velocity $\mathbf{v}_e(\mathbf{r}, t)$. These quantities together with the fields \mathbf{E} and \mathbf{B} are connected via the cold-plasma equations

$$\frac{\partial n_e}{\partial t} + \nabla \cdot (n_e \mathbf{v}_e) = 0, \quad (2.94)$$

$$\frac{\partial \mathbf{v}_e}{\partial t} + (\mathbf{v}_e \cdot \nabla) \mathbf{v}_e = \frac{q_e}{m_e} (\mathbf{E} + \mathbf{v}_e \times \mathbf{B}), \quad (2.95)$$

and the Maxwell equations

$$\nabla \cdot \mathbf{B} = 0 \quad (2.96)$$

$$\epsilon_0 \nabla \cdot \mathbf{E} = \rho \quad (2.97)$$

$$\frac{\partial \mathbf{B}}{\partial t} = -\nabla \times \mathbf{E} \quad (2.98)$$

$$\epsilon_0 \frac{\partial \mathbf{E}}{\partial t} = \frac{1}{\mu_0} \nabla \times \mathbf{B} - \mathbf{j} \quad (2.99)$$

with the electron mass m_e , the electron charge q_e , the permittivity ϵ_0 and permeability μ_0 of the vacuum. The charge density ρ and the current density \mathbf{j} are defined as

$$\rho = q(n_e - n_0), \quad (2.100)$$

$$\mathbf{j} = q_e n_e \mathbf{v}_e, \quad (2.101)$$

with the positive ion density n_0 .

We can now rewrite the cold-plasma equations using the charge density 2.100 and current density 2.101. Equation 2.94 then reads

$$\frac{\partial \rho}{\partial t} = -\nabla \cdot \mathbf{j}. \quad (2.102)$$

The term on the left-hand side in equation 2.95 is the convective derivative known from fluid mechanics. It is a derivative taken with respect to a moving coordinate system and has the general form

$$\frac{D}{Dt} = \frac{\partial}{\partial t} + \mathbf{v} \cdot \nabla, \quad (2.103)$$

where \mathbf{v} represents the velocity of the fluid. Applied to the current density \mathbf{j} this results in an identical representation of equation 2.95

$$\frac{\partial \mathbf{j}}{\partial t} + \sum_k \frac{\partial}{\partial x_k} \frac{\mathbf{j} j_k}{q_e n_e} = \frac{q_e}{m_e} (q_e n_e \mathbf{E} + \mathbf{j} \times \mathbf{B}) - \frac{1}{\tau} \mathbf{j}, \quad (2.104)$$

where a phenomenological time constant τ was introduced to describe the current decay due to Coulomb scattering.

The final set of equations, that has to be solved using a numerical scheme, is then given by [33]

$$\frac{\partial \mathbf{B}}{\partial t} = -\nabla \times \mathbf{E} \quad (2.105)$$

$$\frac{\partial \mathbf{E}}{\partial t} = \frac{1}{\epsilon_0 \mu_0} \nabla \times \mathbf{B} - \frac{1}{\epsilon_0} \mathbf{j} \quad (2.106)$$

and

$$\frac{\partial \mathbf{j}}{\partial t} = -\frac{1}{\tau} \mathbf{j} + \epsilon_0 \omega_{pl}^2 \mathbf{E} + \frac{q_e}{m_e} (\rho \mathbf{E} + \mathbf{j} \times \mathbf{B}) - \sum_k \frac{\partial}{\partial x_k} \left(\frac{\mathbf{j} j_k}{\rho + \epsilon_0 m_e \omega_{pl}^2 / q_e} \right) \quad (2.107)$$

where $\omega_{pl}(\mathbf{r}) = \sqrt{q_e^2 n_0(\mathbf{r}) / (\epsilon_0 m_e)}$ denotes the space-dependent plasma frequency. Equation 2.102 can be obtained by applying the divergence to the Maxwell equation 2.105. The charge density ρ can be viewed as a function of the electric field since each occurrence of ρ can be replaced by

$$\rho = \epsilon_0 \nabla \cdot \mathbf{E}. \quad (2.108)$$

We can see that the last two terms in equation 2.107 introduce the nonlinearity to the system. The first two terms describe the linear Drude model as can be seen by writing equation 2.37 in terms of the current density. This results in

$$\frac{\partial \mathbf{j}}{\partial t} = -\frac{1}{\tau} \mathbf{j} + \epsilon_0 \omega_{pl}^2 \mathbf{E}. \quad (2.109)$$

2.7 Optical Metamaterials

We have seen, that the response of a material to light waves can be described by using effective material parameters ϵ_r and μ_r which neglect microscopic inhomogeneities. The effective medium description is valid, as long as the wavelength of light is much larger than the microscopic structure of the material. But this also makes it possible to synthesize materials with a tailored optical response by engineering subwavelength building blocks and arrange them in a lattice with a subwavelength period. The optical properties are therefore not solely determined by the materials used for the blocks, but also by the shape of each block. This material class is called photonic or optical metamaterials and is able to show optical properties not found in natural existing materials.

One of the most prominent optical phenomena that can be implemented with the photonic metamaterial concept is a negative index of refraction and was already theoretically investigated by Veselago in 1968 [1]. For a negative real part of the index of refraction, the real parts of ϵ and μ both have to be negative as well in the same spectral region. While the former is given for metals at their plasma frequency the latter is not found in natural materials for optical frequencies. Therefore, clever designs for a metamaterial fundamental building block have to be invented to achieve a magnetic response at optical wavelengths. The invention of the split ring resonator by Pendry [3] and the experimental proof of principle by Smith et al. [36] served as a prototype for a magnetic building block.

2.7.1 The Split-Ring Resonator

We will now take a closer look on the design of a metamaterial building block to achieve a magnetic dipole moment at optical frequencies, namely the split-ring resonator (SRR). In essence, it is a simple U-shaped metal structure where external electric and magnetic fields can induce an oscillating ring current within the structure. This ring current then causes a magnetic dipole moment.

In that way, the SRR resembles the working principle of a LC-circuit, where the wire represents on winding of a coil with the inductance \mathbf{L} and the gap between the wires forms a capacitor with the capacitance \mathbf{C} (see figure 2.4 (b)). The eigenfrequency of the circuit is given by

$$\omega_{LC} = \frac{1}{\sqrt{LC}}. \quad (2.110)$$

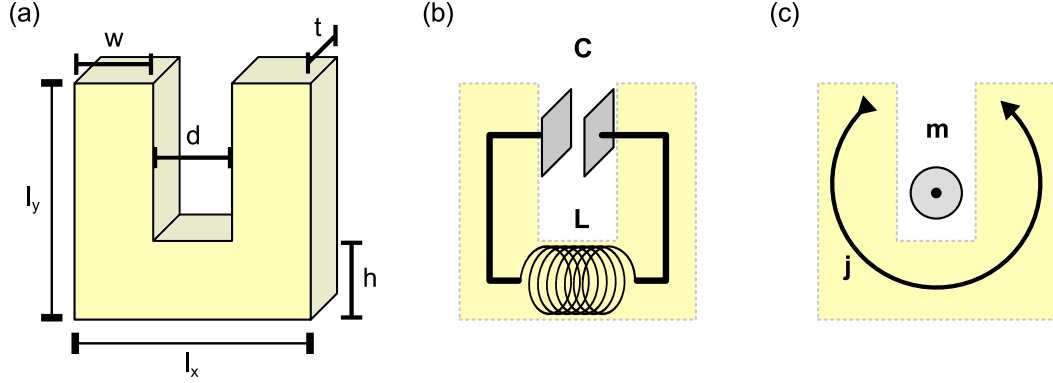


Figure 2.4: SRR and LC-circuit analogy - The U-shaped metal structure with its geometrical dimensions is depicted in (a) while (b) emphasizes the analogy of the structure with a LC-circuit. A magnetic dipole moment \mathbf{m} is connected with the oscillating current \mathbf{j} within the SRR (c).

To bring this frequency into the optical spectral region, the capacitance and inductance therefore need to be very small. The eigenfrequency can be expressed in terms of the dimensions of the SRR in figure 2.4 (a) by using the formula for the capacitance of a plate capacitor

$$C = \epsilon_0 \epsilon_r \frac{\text{plate area}}{\text{plate distance}} = \epsilon_0 \epsilon_r \frac{(l_y - h)t}{d}, \quad (2.111)$$

and the inductance of a coil having one winding

$$L = \mu_0 \frac{\text{coil area}}{\text{coil length}} = \mu_0 \frac{l_x l_y}{t}. \quad (2.112)$$

This gives the eigenfrequency

$$\omega_{LC} = \frac{c_0}{\sqrt{\epsilon_r l_x l_y}} \sqrt{\frac{d}{l_y - h}} \propto \frac{1}{\text{area}}, \quad (2.113)$$

with $c_0 = 1/\sqrt{\epsilon_0 \mu_0}$ as the vacuum speed of light.

For the special case of an quadratic SRR with $l_x = l_y = l$ and $h = w = d$ we can estimate the dimensions using equation 2.113. For a resonance frequency of $2\pi \times 200 \times 10^{12}$ 1/s which corresponds to a wavelength of $\lambda_0 = 2\pi c_0/\omega_0 = 1.5 \mu\text{m}$ we then obtain for $\epsilon_r = 1$ the dimensions $l = 150 \text{ nm}$ and $w = 50 \text{ nm}$ [37].

This result is interesting because we can see that the dimensions of the magnetic building blocks are clearly smaller than the wavelength of light that they were designed for ($\lambda_0 = 1.5 \mu\text{m}$). Therefore they can be arranged in a periodic

2. BASICS OF OPTICS

lattice with subwavelength lattice constants. That way, a medium with effective optical parameters can be implemented, the basic idea of metamaterials. It is also obvious that for a fabrication of such small metal structures sophisticated nano-fabrication techniques are needed.

2.7.1.1 Excitation Configurations

In the last chapter, we have alluded that a magnetic resonance within a SRR can be excited through external electric and magnetic fields. What exact field component of the incoming light couples to the resonance of the SRR depends on the excitation configuration, that is the orientation of the SRR relative to the external fields. The incoming linear-polarized light wave is characterized by its propagation direction and the polarization direction. With respect to the propagation direction, which is determined through the wave vector \mathbf{k} , three basic configurations of the SRR relative to the wave vector can be distinguished. For each of the three configurations, two additional arrangements of the polarization direction can be differentiated.

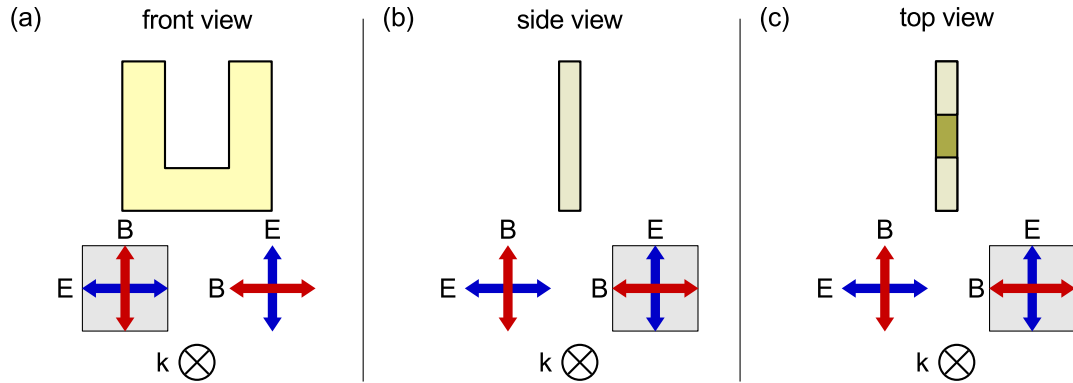


Figure 2.5: Excitation configurations of a SRR - The three different excitation configurations of the SRR relative to the wave vector \mathbf{k} are shown. For each configuration, only one polarization direction (as emphasized by the grey box) of the incoming light can excite the magnetic resonance.

In figure 2.5 (a) the electric component of the incoming light couples to the capacitor of the LC-circuit to excite the ring current while in configurations (b) and (c) the magnetic component couples to the coil. For most experimental studies of the magnetic resonance of SRR arrays, configuration (a) is chosen [6, 38] because the fabrication can be done rather easy using 2D pattern techniques

like electron-beam lithography or focussed ion beam milling [39]. Configuration (b) has only recently been implemented for resonance frequencies in the THz range [40]. Earlier studies used modified SRR designs such as cut-wire and plate pairs [41]. This thesis will also focus on the most common excitation configuration 2.5 (a) of planar split-ring resonators arrays.

2.7.1.2 Higher-Order Resonances

We have seen that the LC-circuit model provides a simple description of the magnetic resonance of a SRR. However, experimental and theoretical studies [6] revealed the existence of additional resonances with higher frequencies than the fundamental magnetic resonance rendering the LC-circuit model invalid for an adequate description of those higher order excitations.

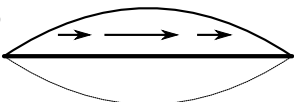
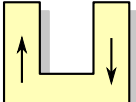
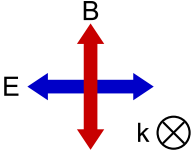
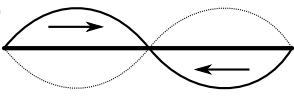
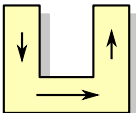
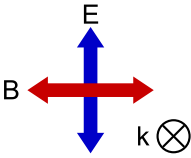
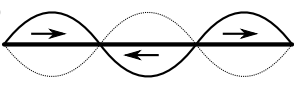
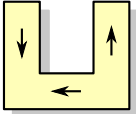
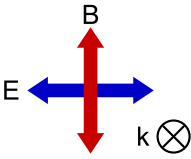
Antenna modes	SRR modes	Excitation polarization
(a.1)  fundamental mode	(b.1)  magnetic mode	horizontal 
(a.2)  first-order mode	(b.2)  vertical-electric mode	vertical 
(a.3)  second-order mode	(b.3)  horizontal-electric mode	horizontal 

Figure 2.6: Eigenmodes of a straight antenna compared to an SRR - The fundamental mode (a.1), first-order mode (a.2) and second-order mode (a.3) of a straight antenna are depicted. For a direct comparison, the corresponding eigenmodes (b.1), (b.2), (b.3) of a split-ring resonator are depicted. The red and blue arrows indicate the polarization direction of the exciting plane wave and black arrows represent the direction of the electric current.

To explain these resonances, we can model the SRR as a folded wire antenna. Unfolding this U-shaped wire leaves us with a simple half wave antenna where

2. BASICS OF OPTICS

we know that a resonant excitation displays standing waves. The wavelength of these standing waves is determined by the length l of the antenna:

$$\lambda_n = n \cdot 2 \cdot l. \quad (2.114)$$

Here the integer n denotes the order of harmonics with $n = 1$ describing the fundamental mode.

Within this fashion, figure 2.6 shows the antenna modes and their equivalent plasmonic excitation in the SRR. The fundamental mode for $n = 1$ then corresponds to the magnetic mode of the SRR. The higher order modes for $n = 2, 3$ are then describing the vertical-electric and the horizontal-electric mode of the SRR, respectively. From this model, we can also infer on the current distribution of the SRR visualized by the black arrows. In the third column, the corresponding configuration for an excitation of the SRR resonance is depicted.

Although this model can explain the existence of higher order resonances, it predicts the wrong spectral position of the resonance wavelengths for SRR in the optical region. If we recall the arm-length of our SRR (150 nm) as we estimated the magnetic resonance wavelength at 1.5 μm within the LC-circuit model, and now use 2.114 to estimate the fundamental order wavelength gives us a result of $\lambda = 2 \cdot 3 \cdot 150 \text{ nm} = 900 \text{ nm}$. In addition, the spectral position of the higher order resonances is also not exactly located at integer multiples of the fundamental resonance frequency as the simple theory predicts as can be seen in experimental results of reference [6]. The same behavior can be found for other nano antenna systems in the visible [42, 43] where the scaling behavior from classical antenna theory is not valid anymore. The reason is the finite electrical conductivity of the metal at optical frequencies. The strong dispersion of the metal changes its electrical length drastically over the range of resonance wavelengths.

3

Materials and Methods

All samples used in this thesis are variations of metallic nanostructures, particular variation of split-ring resonators. In this chapter, we will have a closer look on the steps which are necessary to obtain such structures, and on their subsequent characterization.

3.1 Sample Fabrication

Substrates

The fabrication process starts with the choice of the right substrate. In general, the substrate has to provide mechanical support for the nanostructures. It also must be inert to the chemicals, *i.e.* developers and removers, which are used in the following fabrication steps. Depending on the application, suitable optical properties must also be demanded. In case of the SRR arrays, which were fabricated for the SHG experiments, the substrate should be spectrally flat, *i.e.* no resonances, in the wavelength ranges of the SRR resonances. Commercial available polished quartz plates ¹ provide high transmission in a broad wavelength range (200 nm to 2000 nm wavelength). Because electron-beam lithography plays a major role in the fabrication process, suitable substrates should be electrically conductive to avoid charging effects of the sample. Unfortunately, suprasil plates are electrical isolators, so a thin conductive layer of indium tin oxide (ITO) is applied to the surface by an electron-beam evaporation process. This layer with

¹Planparallelplatten aus Suprasil, Bernhard Halle Nachfl. GmbH, Berlin, 10 mm × 10 × 1mm

3. MATERIALS AND METHODS

a thickness of 5 nm provides an electron drain during the electron-beam writing process, while at the same time the substrate's transparency is maintained. For the split-ring resonators on a gallium arsenide substrate, no conducting layer was needed. A more detailed description of the substrates used in this case can be found in chapter 4.1.

In case of the metamaterial-bolometer application, a high thermal isolation of the detector area is required. The choice of substrate came down to silicon-nitride (SiNi) membranes, which are commercial available ¹ as membranes for transmission-electron microscopy. These membranes with a thickness of 30nm and an area of 100 $\mu\text{m} \times 100 \mu\text{m}$ provide good mechanical support while on the same time offering good thermal isolation. They are also suitable for electron-beam lithography without further preparation, because the membranes' support is made of silicon, which is a good electron drain.

For further processing, the substrates need to be clean. In case of the suprasil plates, wiping off the surface with a soft tissue and acetone is adequate. The Silicon Nitride substrates are already very clean out of the box and can be further processed right away. Mechanical cleaning, anyhow, would not be possible, because the membrane windows are easily destroyed by mechanical stress.

Electron-Beam Lithography

The technique of electron-beam writing allows for high resolution patterning of a polymer film on a substrate. It is often used to fabricate masks for subsequent material deposition, but can also be used to make etching masks or to directly pattern waveguides. The choice of polymer film, the so called resist, of course depends on the application. For material deposition, polymethyl methacrylate (PMMA) is often used.

During the writing process, a focused electron beam is scanned over the sample's surface. When the electron beam hits the polymer layer, it locally changes the resist's chemical properties. In case of PMMA, the exposed areas become soluble to a developer and can be removed that way.

A mixture of methylisobutylketone (MIBK) and isopropyl alcohol (IPA) with a ratio of 1:3 serves as a well experienced developer [44] and was used in this thesis. It should be noted that there are other chemical mixtures available though. The

¹Silison Ltd., Northhampton (Uk)

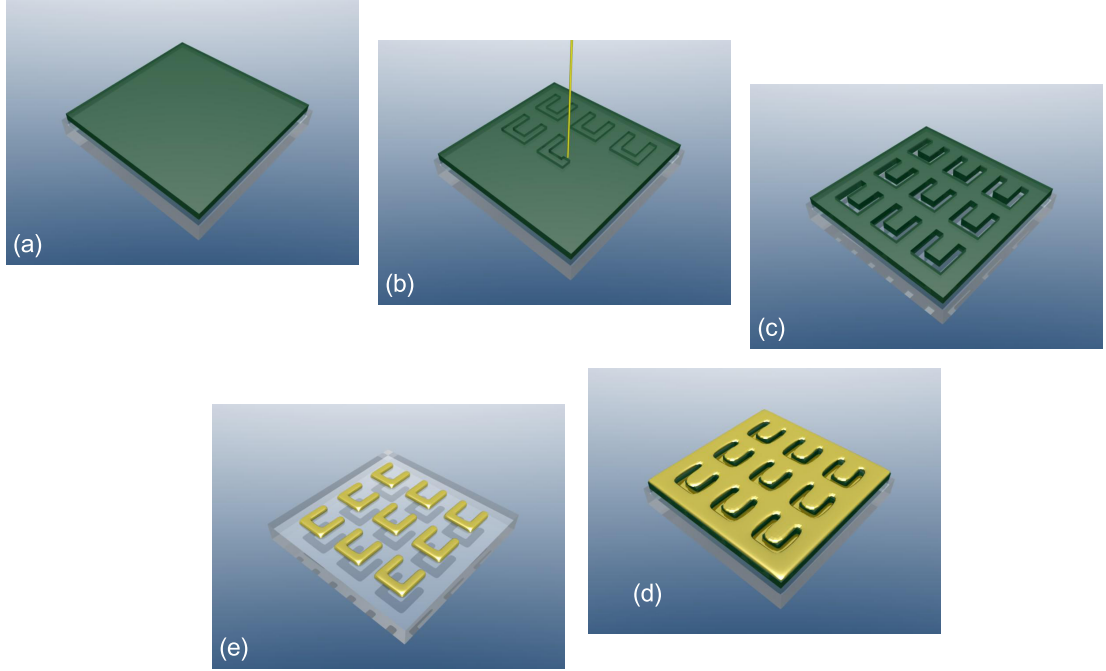


Figure 3.1: Sample fabrication steps - (a) PMMA layer on sample after spin coating, (b) electron beam writing, (c) developing, (d) thin film evaporation of gold, (e) final sample after lift off

thin resist layer is applied on the sample via spin coating. Thereby, a droplet of liquid resist is placed on the clean substrate, which is then spun at high rotation speeds in a spin coater. Due to the centrifugal forces, the polymer droplet dispenses over the substrate's surface, which results in a thin, even polymer film. A following heating process of the sample removes the remaining solvent, leaving a solid polymer layer.

For applications in this thesis, the PMMA resist ¹ was spun at 5000 rpm for one minute, resulting in a thickness of the layer of about 200 nm. After the spinning process, the sample was baked at 165°C for 45 minutes to remove the solvent and solidify the resist. It is then ready for the actual electron-beam writing process.

The samples for the metamaterial metal-bolometer were fabricated using a two-resist system. First, a more sensitive layer of PMMA ² was spun onto the substrate using the same procedure as already described. Then after a baking

¹PMMA 950K A4, MicroChem Corp., Newton (USA)

²PMMA 600K A4, MicroChem Corp., Newton (USA)

3. MATERIALS AND METHODS

procedure of 45 minutes at 165°C, the less sensitive PMMA ¹ layer was applied with the same subsequent baking process on top. This double-layer resist system eases the lift-off process by providing a better undercut of the first PMMA layer.

The electron beam writing of the Split-Ring resonator variants was done using an electron beam lithography system from RAITH ² which consists of a modified scanning-electron microscope (SEM) with an added external pattern generator. This generator allows for precise control of the beam's position relative to the sample. The desired patterns can be designed via a software tool readily available as part of the system. This system provides acceleration voltages for the electron beam of up to 30 kV while providing superior resolution of the beam.

Electron-Beam Evaporation

After the template has been developed, the metal layer can be applied on the mask. This is done with a electron evaporation system. The system allows a variety of materials to be evaporated. Heating of the target is done with shining an electron beam onto. Absorption of the electrons kinetic energy leads to a localized heating of the target. In this thesis, thin films of materials like magnesium fluoride (MgF₂) and gold were deposited with this technique.

Bolometer Fabrication

Because of the electrical connections which are necessary to connect the bolometer to the outside world, additional fabrication steps are needed for the bolometer samples. For easy exchange of the samples in the vacuum chamber, the sample is glued on an IC-carrier ³. The carriers provide mechanical stability and robust electrical connectivity. They were modified in the workshop where a hole was drilled in the bottom. This allows for a transmission spectroscopy setup. The gold pads on the sample are connected to the IC carrier via wire-bonding of aluminum wires.

¹PMMA 950K A4, MicroChem Corp., Newton (USA)

²e_LINE from Raith GmbH, Dortmund

³PartNo.:SB01611, Universal Enterprise, www.ue.com.hk

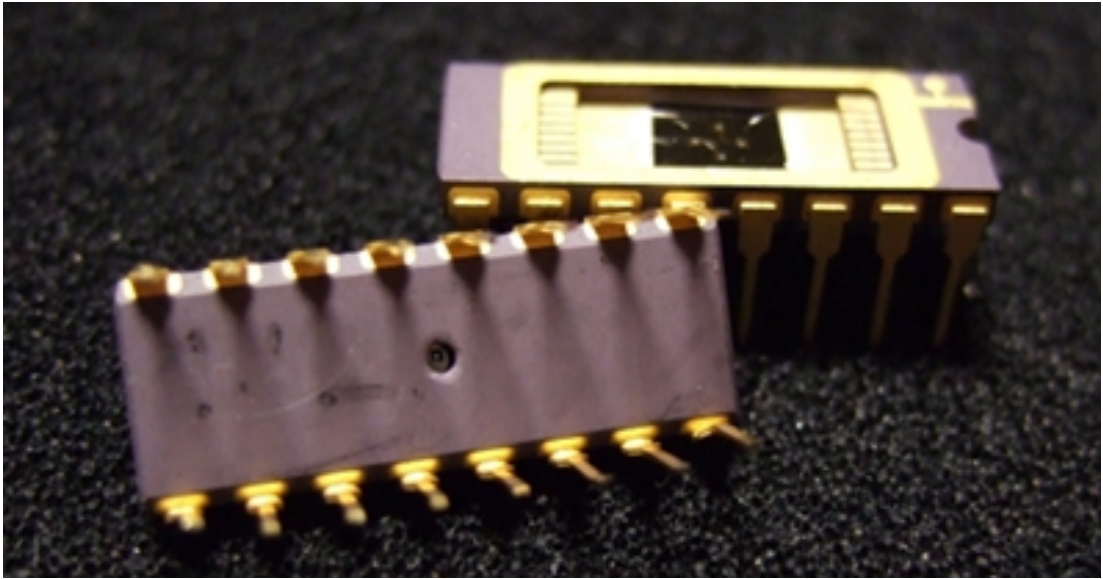


Figure 3.2: Two IC carriers - The fabricated bolometer sample is glued on the carrier and electrically connected to the pins via wire bonding. The carrier in the front is flipped around to see the modification on the bottom. A small hole (diameter 1mm) was drilled in the support to allow for transmission spectroscopy of the sample.

3.2 Sample Characterization

3.2.1 Linear Optical Characterization

The linear optical resonance properties of our fabricated metal nanostructures can easily be characterized by using a Fourier-transform-infrared spectrometer (FTIR). The system used in this thesis is commercial available from Bruker Optik¹ and comes with an optical microscope attached. That way its pretty easy to visual localize the areas on the sample to be characterized. Two cassegrain lenses are used to focus the light from a halogen lamp on the sample and collect the light to forward it on the detector. With a combination of linear polarizers, measurements of polarization dependent spectra can be obtained. This set-up allows to measure transmission and reflection spectra in a broad wavelength range from 0.4 μm up to 5 μm through the use of two different detectors, depending on the desired spectral range. For the visible spectral range (0.4 μm - 1.2 μm

¹Bruker Equinox 55 and Bruker Hyperion 1000, Bruker Optik GmbH, www.bruker.com

3. MATERIALS AND METHODS

wavelength), a silicon based detector is available, while for the infrared region (0.9 μm - 5 μm) a liquid-nitrogen cooled indium-antimonide detector is used.

Numerical Transmission/Reflection Spectra Calculation

For calculation of transmission and reflection spectra of the metallic nanostructures, a 3D electro-magnetic simulation tool for high frequency components was used. The commercial-available software-tool CST Microwave Studio ¹ provides a convenient tool for 3D modeling of metal-dielectric structures and subsequent analysis of electromagnetic high frequency behavior. It is based on a finite-integration time-domain method. For a calculation of reflection and transmission spectra, a waveguide geometry is used. The time-domain solver gives back the S-parameter values for both ports. From these values, the transmission and reflection spectra can be obtained. In the simulation domain, also near field monitors can be added to get the distributions of the magnetic and electric fields in the vicinity of the nanostructure.

¹MWS, CST Computer Simulation Technology AG, www.cst.com

4

Nonlinear Optical Experiments

Within this chapter a series of experimental studies on the second-harmonic generation (SHG) from split-ring resonators is presented. In the first section we treat the experimental and theoretical investigation of second-harmonic generation from arrays of split-ring resonators on crystalline gallium arsenide (GaAs) substrate.

In the second section, the experimental results of nonlinear optical-spectroscopy on second-harmonic generation from split-ring-resonator arrays is presented. These experiments were motivated by previous nonlinear optical experiments on SRR arrays [45, 46, 47] and related structures [48, 49] that were all performed at fixed fundamental frequency. To gain more insight in the nonlinear mechanism that drives SHG from metal structures we have extended the experiments to nonlinear optical spectroscopy using a tunable light source for the excitation of the structures. The first set of samples reveals pronounced SHG resonances and we continued the study with a second set of samples in which the fundamental SRR resonance frequencies are lithographically tuned while leaving the higher-order resonances fixed. The obtained spectroscopic data immediately clarify the role of higher-order resonances as the nonlinear source while the higher-order resonances merely reabsorb the SHG light. This data set can also provide a test ground for future microscopic theories regarding the underlying nonlinear mechanism.

The last section of this chapter presents the results of optical experiments on second-harmonic generation from split-ring-resonator square arrays where the lattice constant of each array was varied. As a result, a non-monotonic dependence of the conversion efficiency on the lattice constant was found. This finding is

4. NONLINEAR OPTICAL EXPERIMENTS

interpreted in terms of a competition between dilution effects and linewidth or near-field changes due to interactions among the individual elements in the array.

4.1 SHG from Split-Ring Resonators on GaAs Substrate

In the original publication on the concept of the SRR by Pendry *et al.* [3] it was already suggested to obtain an enhanced nonlinear optical response through insertion of a nonlinear material in the gap of the SRR. The electric field is concentrated in this area under resonant excitation of the SRR. This makes a nonlinear response of the inserted material more efficient. However, a precise placement of a nonlinear optical material in the gap region of a nanoscopic resonator is a technical challenge.

Recent experimental studies of plasmonic nanostructures in combination with nonlinear optical materials used a slightly different concept. They brought the entire structures in direct contact with the nonlinear optical material [50, 51]. Here, we used the same concept and placed the SRR arrays directly on a nonlinear substrate to overcome the technical difficulties. At the same time we were aiming to achieve a more efficient frequency compared to SRR on a simple glass substrate [45].

The wafers were ordered with both faces of the wafer optically polished. This allowed us to see through the substrate using an infrared camera. This is a necessity for the localization of the right SRR arrays when the sample is placed in the optical setup. Using a diamond cutter, the wafers were cut into small pieces which then served as substrates for the subsequent electron beam writing process (as described in chapter 3). After that, a 25 nm thin gold layer was deposited serving as the metal for the SRR.

4.1 SHG from Split-Ring Resonators on GaAs Substrate

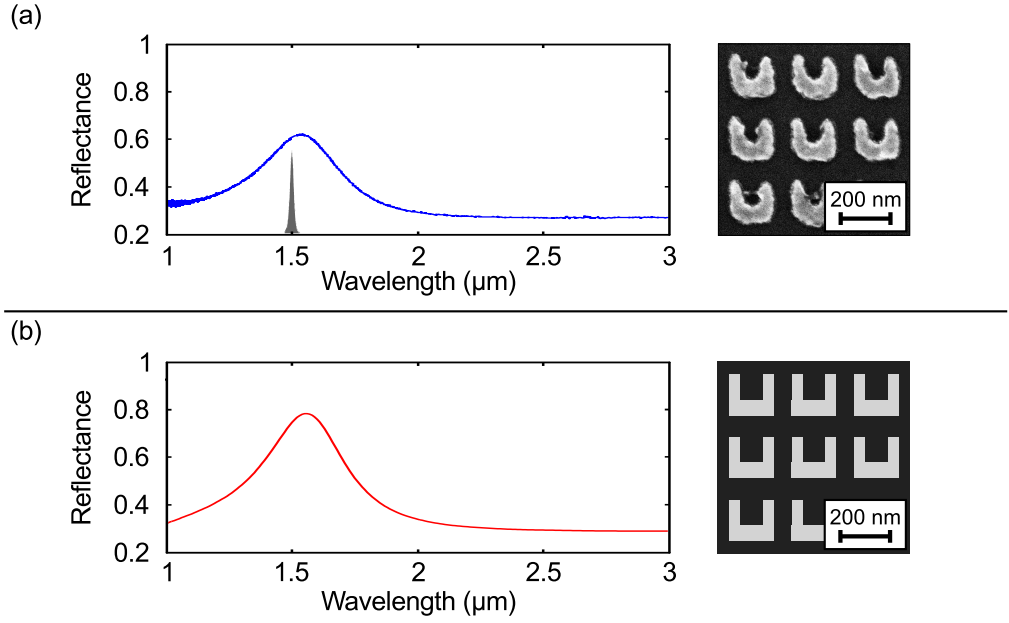


Figure 4.1: Linear optical characterization - Measurement (a) and simulation (b) of the normal incidence reflection spectra of a selected SRR array on GaAs substrate as taken from the air side. The incident light is linearly polarized along the horizontal direction. The narrow gray area illustrates the exciting laser spectrum centered at 1.5 μm . The scanning electron micrograph on the right-hand side of (a) shows the SRR from the sample, in (b) the corresponding dimensions used for the theoretical calculations is shown. (figure from [52])

In our first experiments, we encountered that the SHG signal from the gold SRRs on the GaAs substrate steadily decreased with time during the intense laser irradiation. We ascribe this effect to a heat induced inter-diffusion of gold and the GaAs substrate. The inter-diffusion effect is well known in the context of Schottky barrier formation [53]. In our context, this might have led to a substantial change of the material properties of the substrate and the SRR. To get rid of this effect we deposited a 10 nm thin film of magnesium fluoride (MgF_2) right underneath the gold SRR serving as a diffusion barrier. With this measure, the SHG signal stayed stable during the whole measurement time, which typically spanned several days. The footprint of our fabricated SRR arrays were $60 \mu\text{m} \times 60 \mu\text{m}$.

Before the nonlinear optical experiments were conducted, a linear optical char-

4. NONLINEAR OPTICAL EXPERIMENTS

acterization of the fabricated samples was necessary to select the arrays having a magnetic resonance centered around 1.5 μm . This wavelength corresponds to our laser excitation wavelength of the following SHG experiments. Compared to earlier experiments of SRR on glass substrates [45, 46], the SRR had to be about 30 % smaller to achieve a magnetic resonance at the fundamental laser wavelength. This is due to the higher refractive index of the GaAs compared to the glass substrate.

4.1.1 Nonlinear Optical Characterization

For the measurement of the second-harmonic generation we have used a setup as sketched in figure 4.2. A commercial available ¹ optical-parametric oscillator (OPO) was employed as a light source delivering pulses at a repetition rate of 86 MHz with a pulse duration of 170 fs. The OPA was tuned to 1.5 μm wavelength and its output power was typically 90 mW.

The OPA needs to be pumped by a titanium sapphire (Ti:Sa) laser to make the optical parametric oscillation work. We used the Tsunami ² that emits pulses with a length of 120 fs at 810 nm, at a repetition rate of 86 MHz. The Tsunami itself is again pumped by a green (532 nm) diode-pumped solid-state laser ³, operating in continuous wave mode. The green light is obtained by a frequency conversion of the neodym vanadate laser medium, originally emitting at a wavelength of 1064 nm. The light from the OPA is then fed into the optical setup via two mirrors that allow a precise and reproducible tuning of the beam's position and angle via the beam walking technique. The beam passes a combination of a half-wave plate and a polarizer that is adjusted to pass horizontal polarized light. Because the beam from the OPO is also horizontally linearly polarized, rotating the half-wave plate changes the direction of polarization and consequently modifies the power that is available after the polarizer. For the experiments, we adjusted the power to approximately 45 mW.

After the polarizer, a lens focusses the light onto the sample that is attached to the sample holder . This results in a size of the gaussian spot of 60 μm on the sample's surface as measured by a knife-edge technique. The SHG signal from

¹OPAL, SpectraPhysics Inc.

²Tsunami, SpectraPhysics Inc.

³Verdi V18, Coherent

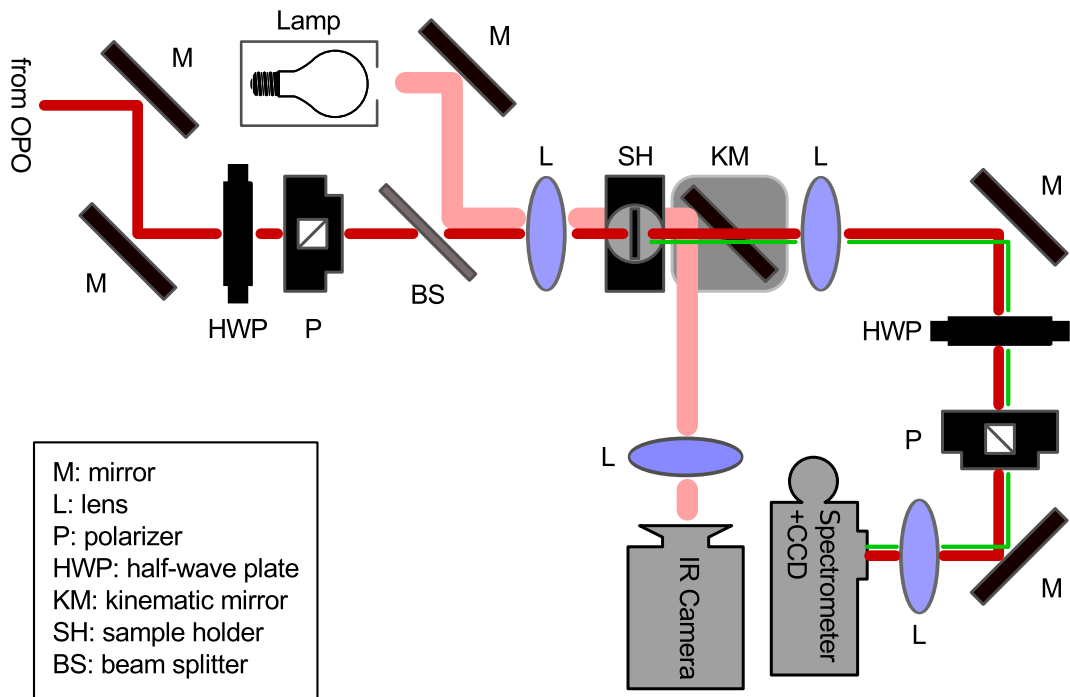


Figure 4.2: Sketch of the optical setup - The sketch represents the optical setup used for the nonlinear optical study of the SRR arrays on GaAs substrates. A detailed description can be found in the text.

4. NONLINEAR OPTICAL EXPERIMENTS

the SRR array is emitted at 750 nm where the GaAs substrate is absorbing the light. We therefore mounted the samples with the SRR side facing towards the detector. The exciting light is then impinging from the substrate side and the SHG is emitted into the air side. In turn, the excitation wavelength is in a spectral range where the GaAs is transparent. After the sample holder, a removable mirror is placed. When this mirror is present in the set-up and the lamp is turned on, an image of the sample is projected onto a CCD infrared camera. This makes is very easy to navigate the SRR arrays relative to the laser beam by adjusting the sample holder. During the measurements, the lamp is of course turned off and the mirror is removed from the beam path.

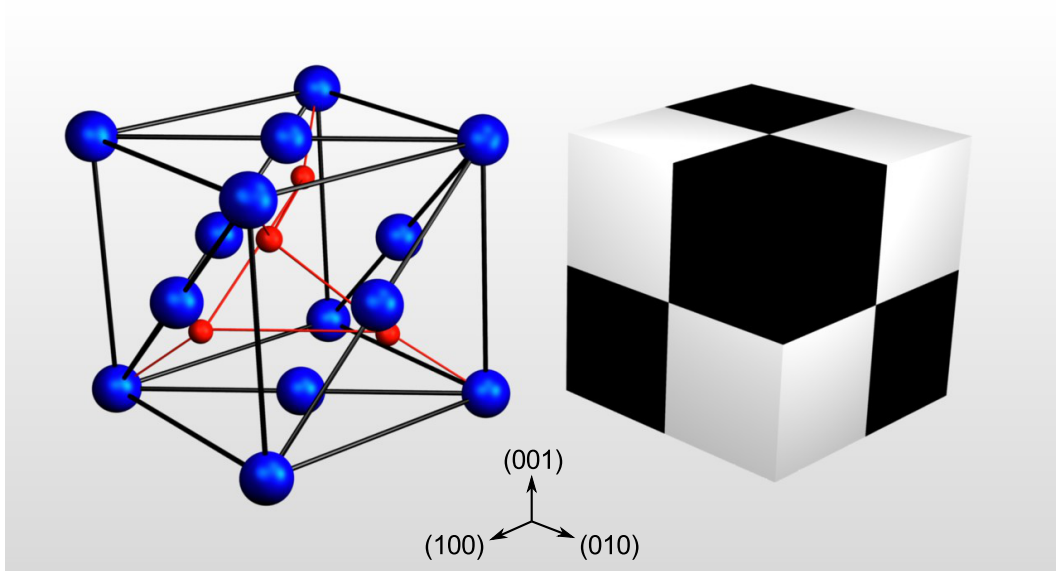


Figure 4.3: GaAs crystal structure - On the left-hand side, the crystal structure of GaAs which crystallizes in the zinc-blende structure is depicted. The blue balls illustrate the gallium atoms while the red balls show the position of the arsen atoms in the unit cell. On the right-hand side, the crystal is schematically represented by a "checker-board cube". (figure from [52])

The emitted SHG is then collimated via another lens and directed towards a combination of a half-wave plate and a polarizer. In this combination, a rotation of the half-wave plate allows an easy analyzation of the polarization direction of the emitted second-harmonic light. This transmitted light is then picked up and focussed by another lens in front of the detector. As the detector unit, a grating

spectrometer ¹ in combination with a charge-coupled device (CCD) camera ² attached to the spectrometer was used. The spectrometer spectrally disperses the SHG signal and images its output on the CCD chip. The spectral shape and intensity of the signal can then be monitored by a read out of the chip's data using a computer system.

4.1.2 Experimental Results and Discussion

In the experiments, we have used wafers with two different crystal grow directions as a substrate for the SRR arrays. That means, that for one configuration the surface normal of the substrate is pointing along the (100) direction of the crystals principle axis. In the other configuration it is pointing along the (110) direction. In figure 4.3 the unit cell of the crystal is presented together with a schematic representation, a so called checker-board cube, to illustrate the symmetry of the cell.

In figure 4.4 three different configurations and their corresponding measurement results are presented. In the left column, the orientation of the crystal relative to the SRR is shown as illustrated by the checkerboard cube that allows a direct comparison with figure 4.3. The fundamental beam is propagating along the $+z$ direction, as the measured SHG light does. The polarization direction of the incident beam is along the x axis which corresponds to a horizontal excitation of the SRR as illustrated by the red arrow.

For each configuration we compared the SHG signal from the arrays with the corresponding measurement off field, *i.e.* the bare substrate. In configuration figure 4.4 (a), the signal from the array is about 40 times stronger than the bare substrate. The polarization direction is determined by the symmetry of the SRR and in agreement with previous experiments [45, 46, 47].

In strong contrast to this result, the emerging SHG in configuration figure 4.4 (b) is nearly horizontal polarized (along the x direction) and also stronger about one order of magnitude than for configuration figure 4.4 (a). The off-field signal in this configuration is about 50 times weaker. From this findings we conclude that the measured horizontal component of the SHG signal for figure 4.4 (b) stems specifically from the interplay of the crystalline GaAs substrate and the

¹Chromex 250i, Chromex Inc.

²LN CCD-1340/44-EHR, Princeton Instruments

4. NONLINEAR OPTICAL EXPERIMENTS

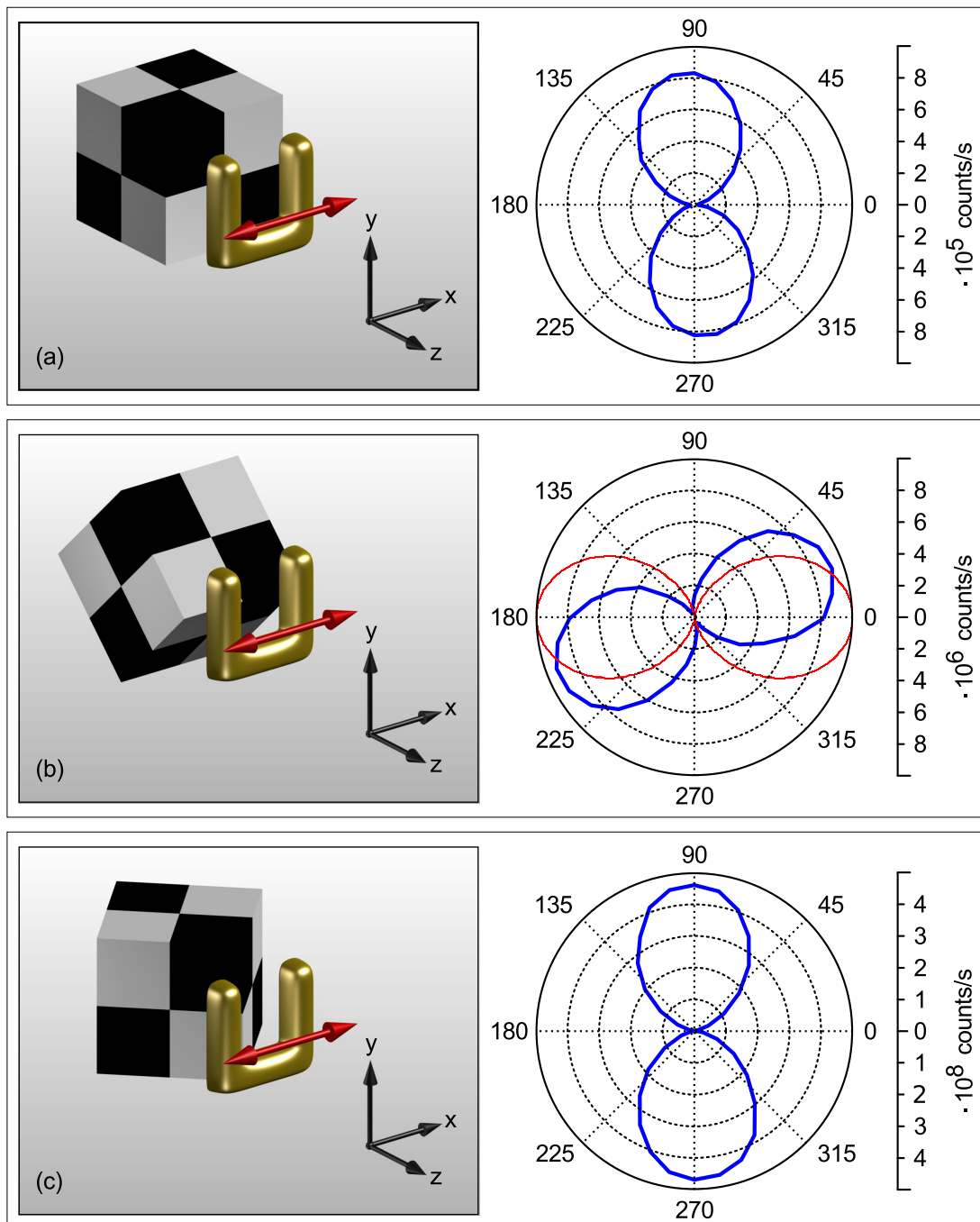


Figure 4.4: Measurement of the SHG - Polarization analysis from the three different samples: (a) shows the (100) GaAs configuration and (b),(c) the (110) configuration. The orientation of the crystal relative to the SRR is illustrated in the left column. The right column shows the measured polar diagrams (blue curves). The experiments in (b) can be directly compared with the results from the theoretical calculations (shown as red curve in the diagram). (figure from [52])

4.1 SHG from Split-Ring Resonators on GaAs Substrate

SRR. The slight rotation of the figure eight could be explained by an additional vertically polarized contribution from the bare SRR [45, 46, 47]. In addition, the SHG signals from the SRR on the GaAs substrate in this configuration are a factor of 25 larger than those on a glass substrate that have been previously measured [45, 46, 47].

In configuration figure 4.4 (c), the signal levels are much higher compared to figure 4.4 (a) and (b). Here, the SHG signal is dominated by a SHG signal that originates from the GaAs substrate because the measurement off field revealed a very strong SHG emission polarized along the y direction.

Although in both substrate configurations the same material is present, one cannot expect the same results regarding the SHG from the substrate under normal incidence of the fundamental light. The difference between both substrate configuration is a rotated crystal, which of course changes the form of the nonlinear tensor $\chi^{(2)}$.

From symmetry inspections, the only nonvanishing $\chi^{(2)}$ tensor elements in our laboratory frame of reference are [22] (corresponding to the (100) wafer configuration)

$$\chi_{xyz}^{(2)} = \chi_{yxz}^{(2)} = \chi_{zxy}^{(2)} = \chi_{xzy}^{(2)} = \chi_{yxz}^{(2)} = \chi_{zyx}^{(2)}. \quad (4.1)$$

We need to take only those elements in account that produce a nonlinear polarization that is polarized either in the x or y direction or both and can additionally be excited by our fundamental beam, that is polarized along the x direction. It is immediately clear that for this configuration no emission of SHG from the substrate is expected. Our experimental results in figure 4.4 (a) confirm this.

For an inspection of the relevant tensor elements for the (110) wafer configuration we need to transform the bulk $\chi^{(2)}$ tensor components using a transformation matrix as already described in the basics section. To get from configuration figure 4.4 (a) to (b) we rotate the crystal by 45° along the x axis of the laboratory frame. This is described by the set of Euler angles with $\alpha = 0, \beta = \pi/4, \gamma = 0$. The non-vanishing tensor components that are responsible for a nonlinear polarization along the $(x-y)$ direction then read

$$P_x^{(2)} = \epsilon_0 \chi_{xzz}^{(2)} E_z E_z - \epsilon_0 \chi_{xyy}^{(2)} E_y E_y, \quad (4.2)$$

$$P_y^{(2)} = \epsilon_0 \chi_{yxy}^{(2)} E_x E_y - \epsilon_0 \chi_{yyx}^{(2)} E_y E_x, \quad (4.3)$$

4. NONLINEAR OPTICAL EXPERIMENTS

with $\chi_{xzz}^{(2)} = \chi_{xyy}^{(2)} = \chi_{yxy}^{(2)} = \chi_{yyx}^{(2)}$.

From this result we can immediately explain the result of measurement figure 4.4 (c). This configuration corresponds to the situation where we would have excited the substrate with vertical polarized light and the strong field component E_y of the incoming light would cause a nonlinear polarization along the x direction.

But the most interesting case is found in 4.4 (b), where the near fields of the SRR must be responsible for a nonlinear polarization along the y direction. To test this assumption, we did a numerical simulation of the near-fields. The result is shown in figure 4.5. The near-fields were obtained using a home-built finite-difference time-domain (FDTD) computer program to solve the linear Maxwell equations for our experimental geometry as shown in figure 4.1, where also the corresponding reflectance spectrum is presented.

The gold of the SRR was described by the linear free-electron Drude model using a plasma frequency of $\omega_{pl} = 2\pi \times 2.2 \times 10^{15}$ 1/s and collision frequency $\omega_{coll} = 2\pi \times 1.72 \times 10^{13}$ 1/s to account for phenomenological damping effects. The refractive index of the GaAs substrate was taken as $n_{\text{GaAs}} = 3.37$ and for the 10 nm thin MgF_2 layer, $n_{\text{MgF}_2} = 1.34$ was used.

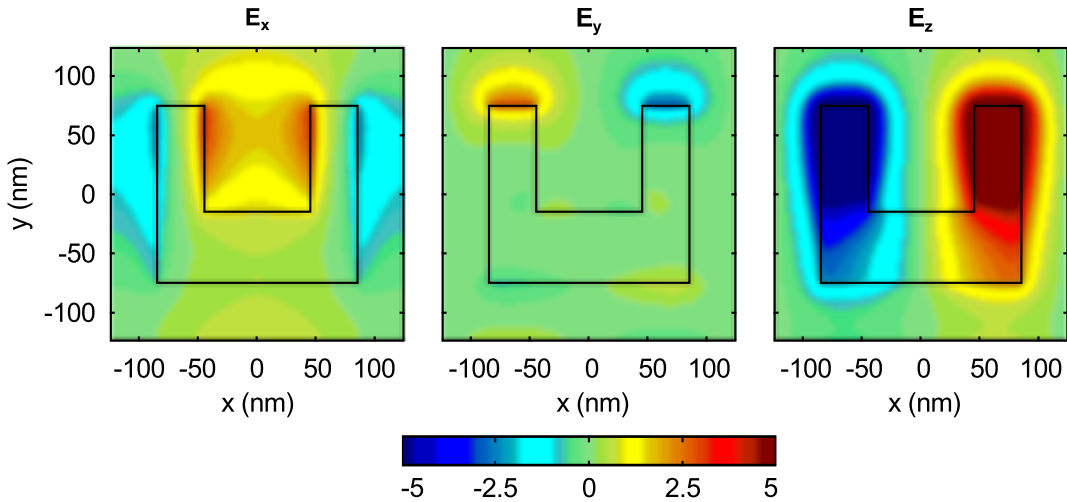


Figure 4.5: Snapshot of the local electric field - The field components shown are located underneath the SRR inside the GaAs for a excitation at 1.5 μm wavelength using a 170 fs Gaussian pulse. All components are equally normalized to the incident electric-field amplitude in the GaAs. (figure from [52])

4.1 SHG from Split-Ring Resonators on GaAs Substrate

With these field data at hand, we calculated the effective transverse SHG polarization $\langle P_x^{(2)} \rangle$ and $\langle P_y^{(2)} \rangle$ as a spatial average over one unit cell using 4.3. By visual inspection of figure 4.5 it becomes clear that $\langle P_y^{(2)} \rangle \propto \langle E_x E_y \rangle = 0$, whereas in contrast $\langle P_x^{(2)} \rangle \propto \langle E_z E_z - E_y E_y \rangle \neq 0$. The emerging SHG is therefore expected to be horizontally polarized, *i.e.* along the x direction (see the red curve in figure 4.4 (b)). It is also apparent from the near field plots (4.5), that the emerging SHG signal is driven mainly by the dominating axial component E_z . Without any SRRs on the substrate present, the incident E_x component alone cannot generate a SHG signal at all. Because we have neglected nonlinearities from the SRRs metal, we also get strict zero SHG signal for the bare SRR. The calculated SHG signal arises solely from the combined system of SRR and the GaAs substrate.

4.1.3 Conclusions

With these experiments, we have studied the SHG generation from SRR arrays on a crystalline GaAs substrate. The special crystal structure of the GaAs allows for different orientations of the SRR relative to the crystal's unit cell where basically three configurations can be distinguished. In the first configuration, the SHG response of the combined system is determined by the SRR alone and the GaAs serves merely as a high-refractive index substrate. The second configuration is dominated by the response of the GaAs substrate and the presence of the SRR array on top leads to a reduced intensity of the SHG. The third configuration reveals an interplay of the optical near-fields of the SRR and the GaAs substrate.

4.2 SHG Spectroscopy on Split-Ring-Resonator Arrays

In our nonlinear optical spectroscopy experiments we have studied the SHG from split-ring-resonator arrays on glass substrates. The resulting spectroscopic data helps in clarifying the role of higher-order resonances. It can provide a much more sensitive future testing ground for microscopic theories of the underlying mechanism compared to fixed wavelength experiments that were conducted before [45, 46, 47].

4.2.1 Sample Fabrication and Linear Optical Characterization

The fabrication of the gold SRR samples is already described in detail in 3.1. The footprint size of the SRR arrays on the glass substrate is $200\ \mu\text{m} \times 200\ \mu\text{m}$. The thickness of the gold film was about 30 nm for all fabricated samples. For the configuration of the single SRRs within the array we used a lithographic tuning method as illustrated in 4.6 to produce different samples.

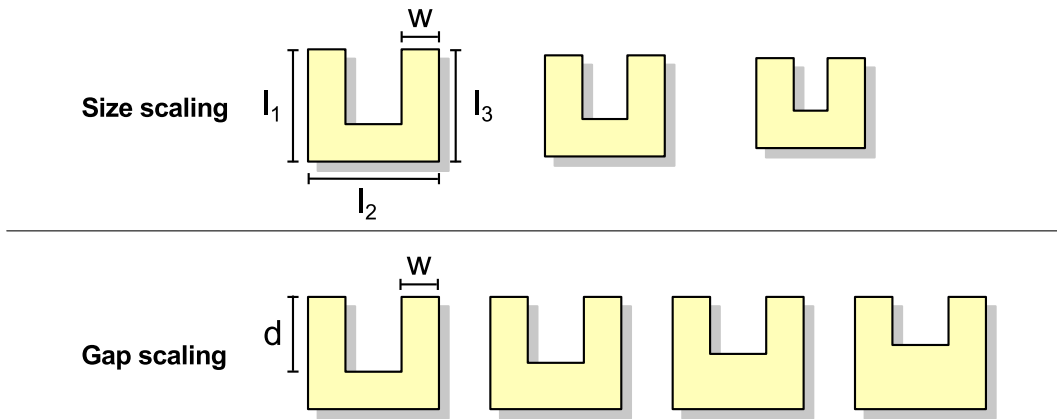


Figure 4.6: Lithographic tuning - In the top row, the size of the SRR is reduced while keeping the arm-width w constant. In the bottom row the size and arm-width is kept constant but the gap depth d is reduced. The magnetic resonance wavelength is decreased for both scaling methods from left to right.

4.2 SHG Spectroscopy on Split-Ring-Resonator Arrays

In case of size scaling of the SRR, the arm width and the thickness of the gold film was kept constant. The lengths l_1, l_2, l_3 were scaled down proportionally to reduce the overall size of the SRR. This leads to a decrease of the spectral positions of the fundamental magnetic and higher-order electric resonances.

Another tuning method used was the scaling of the gap depth d . Here, the arm-width w and the size of the SRR as well as the thickness of the gold film were kept constant and only the depth of the gap d was modified. This affects the spectral position of the fundamental magnetic resonance leaving the higher-order electric resonances spectrally fixed.

Both tuning methods were employed on our samples and their linear extinction spectra were measured with an FTIR to select those arrays with the appropriate resonance positions. In figure 4.8 three configurations where size scaling was employed were selected and their scanning electron micrographs are depicted. The corresponding linear extinction spectra show an increase of the magnetic resonance wavelength from the top to the bottom configuration. It can also be seen that the higher order resonances also move in their spectral position. In figure 4.9, the four selected SRR configurations for the gap scaling are presented. Here, the magnetic resonance wavelength decreases from the top to the bottom configuration while the higher order resonances are nearly fixed in their spectral position.

4.2.2 Nonlinear Optical Characterization

The setup for the nonlinear optical spectroscopy of the SRR arrays is sketched in figure 4.7. An optical parametric amplifier (OPA) ¹ was employed as a tunable light source delivering pulses with a duration of about 150 fs at a repetition rate of 1 kHz. The emission wavelength can be tuned in the range of 1.2 μm up to 1.56 μm via a manual adjustment. The OPA itself is pumped by a regeneratively amplified Ti:Sa femtosecond laser ² with a repetition rate of 1 kHz.

The output from the OPA is first filtered using a double-side-polished silicon wafer piece to remove any residual light below a wavelength of 1.1 μm that may leave the device. Then the vertical polarized beam hits a periscope to lower the

¹OPA 800 CF, SpectraPhysics Inc.

²Hurricane, SpectraPhysics Inc.

4. NONLINEAR OPTICAL EXPERIMENTS

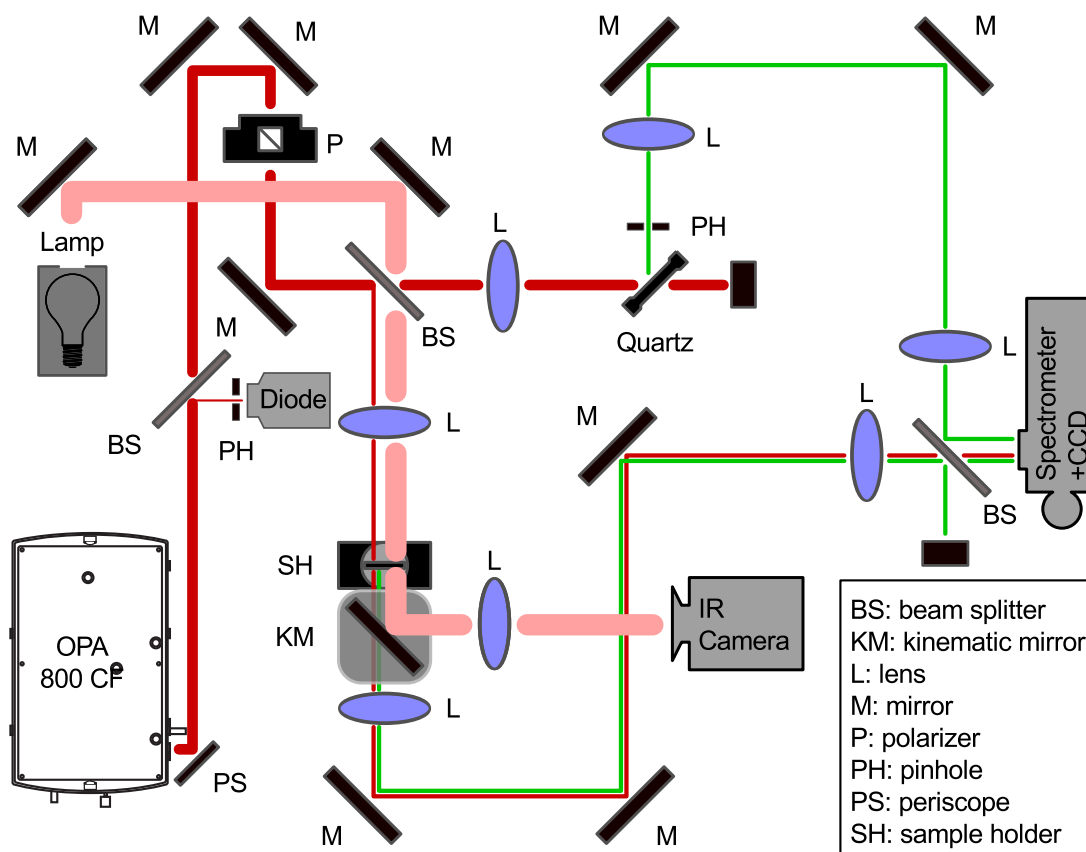


Figure 4.7: Optical setup for nonlinear optical spectroscopy - The sketch represents the optical setup used for the nonlinear optical spectroscopy experiments. A detailed description can be found in the text.

4.2 SHG Spectroscopy on Split-Ring-Resonator Arrays

beam to the height of the mirrors and lenses on the table. This measure also changes the polarization of the beam to a horizontal polarization direction.

A beam splitter reflects a small portion of the emitted light onto a photodiode with a pinhole in front. The output of the diode is monitored on an digital oscilloscope. Maximizing the signal from the diode via adjusting the OPA and the mirrors of the periscope provides a way to reproducibly couple the beam into the optical setup.

The beam from the OPA is then sent through a polarizer to provide an excellent horizontal polarized beam that afterwards hits another beam splitter. The much lower intensity reflection from the splitter is focused on the sample using a lens, resulting in a Gaussian spot with a diameter of 60 μm (measured with a knife edge technique). The sample itself is mounted on the sample holder that allows for a fine adjustment of the position of the sample in all three space dimensions relative to the incoming beam. At the laser powers used (below 500 μW average power, equivalent to 0.5 μJ pulse energy, or 3.3 MW peak power equivalent to about 100 GW cm^{-2} peak intensity on the sample). We find no deterioration of the SHG signal from the gold SRR samples during our measurements that usually ran over several days. Another lens is then used to defocus and collimate the fundamental and SHG light again and sent it on its way to the detector. A lens finally focusses the beams again into the detector system, consisting of grating spectrometer that is connected to a sensitive liquid-nitrogen cooled silicon CCD camera.

When the OPA is tuned through its wavelength range, its average power, its pulse duration, its beam divergence, as well as its spot diameter can change. This in return leads to a substantially change in the focus conditions on the SRR sample, strongly altering the SHG signal intensity. To handle this behavior we normalize the SHG signal from the SRR array to the SHG that is obtained from the surface of a quartz crystal plate.

This crystal plate is located in a second arm of our experimental setup and is excited by the much more intense portion of the fundamental light that is transmitted through the beam splitter. The lens, that is focussing the light on the quartz crystal, is identical to the one used for focussing the light on the sample. This measure provides the same focus conditions on the sample and the crystal. The quartz crystal is mounted under an angle of approximately 45° relative to

4. NONLINEAR OPTICAL EXPERIMENTS

the incident beam. We have chosen a quartz crystal as a reference material due to its optical nonlinearity and resistance against high power excitation. It will also show no significant spectral dependence because its band gap lies in the UV region at around 8.4 eV [54] which corresponds to 148 nm wavelength. The quartz has a thickness of 5 mm, a footprint dimension of 2 cm \times 2 cm and is optically polished on both faces ¹.

The reflected SHG from the surface of the crystal is selected by a pinhole and then defocussed and collimated by a lens. This lens is again equal to the one used to defocus the SHG emitted from the sample itself. The SHG from the reference arm finally focused into the spectrometer and CCD camera combination. By accurately adjusting the relative position of the two beams at the spectrometer entrance slit, both SHG signals can be measured and monitored at the same time by the 400 \times 1340 pixels of the CCD. Each beam is detected on a area of the CCD chip with a height of 200 pixels. The software ² allows to read out both regions of interest to get the SHG emission spectra of the sample and the reference at the same time. The SHG intensity for each channel is then obtained by integrating over the spectral peak.

With this setup, we have obtained reproducible experimental results that are presented in figure 4.8 and 4.9. The normalization is the same for all samples and experimental conditions and given by

$$I_{\text{SHG, normalized}} = \frac{I_{\text{SHG, sample}}}{I_{\text{SHG, reference}}} \quad (4.4)$$

This allows for a direct comparison of the signal strengths in figures 4.8 and 4.9.

4.2.3 Experimental Results and Discussion

In figure 4.8 (a) - (c), the measured second-harmonic-generation spectra from three different SRR configurations, where size scaling was employed, are shown. As already stated, the incident fundamental laser beam is linearly polarized along the horizontal direction. This corresponds to the red double arrow depicted in the scanning-electron micrographs shown as insets in the figures. Due to the symmetry of the SRR, the SHG emerges with vertical linear polarization as defined by the blue double arrows, shown in the same micrographs.

¹z-cut quartz; Boston Piezo-Optics Inc.

²WinSpec, Princeton Instruments

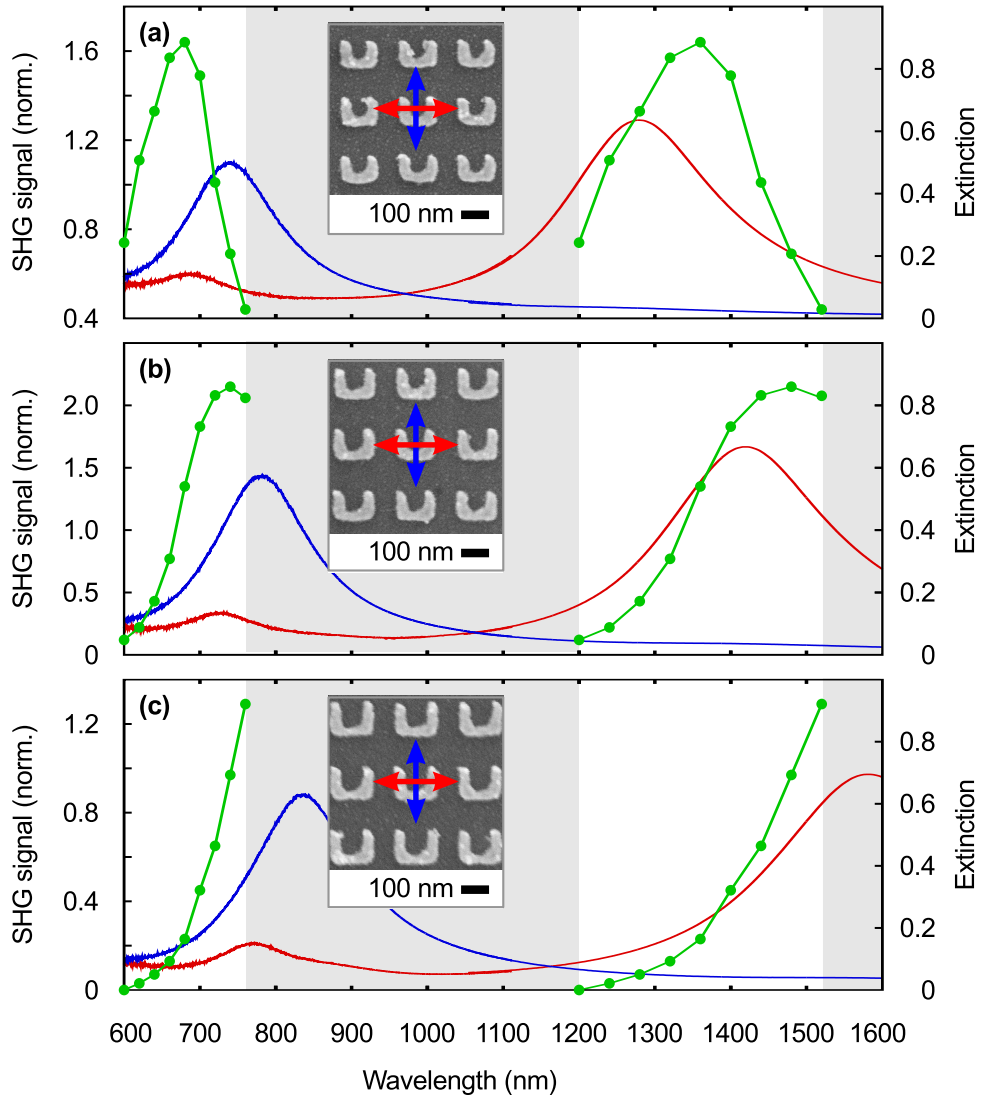


Figure 4.8: Linear and nonlinear measurements on the size scaled samples - Second-harmonic-generation spectra (dots connected by green straight curves as guides to the eye) obtained for the set of three different size scaled samples. The linear extinction spectra (solid blue and red lines) are color coded to their corresponding polarization direction as indicated by the blue and red arrows. (figure from [55])

4. NONLINEAR OPTICAL EXPERIMENTS

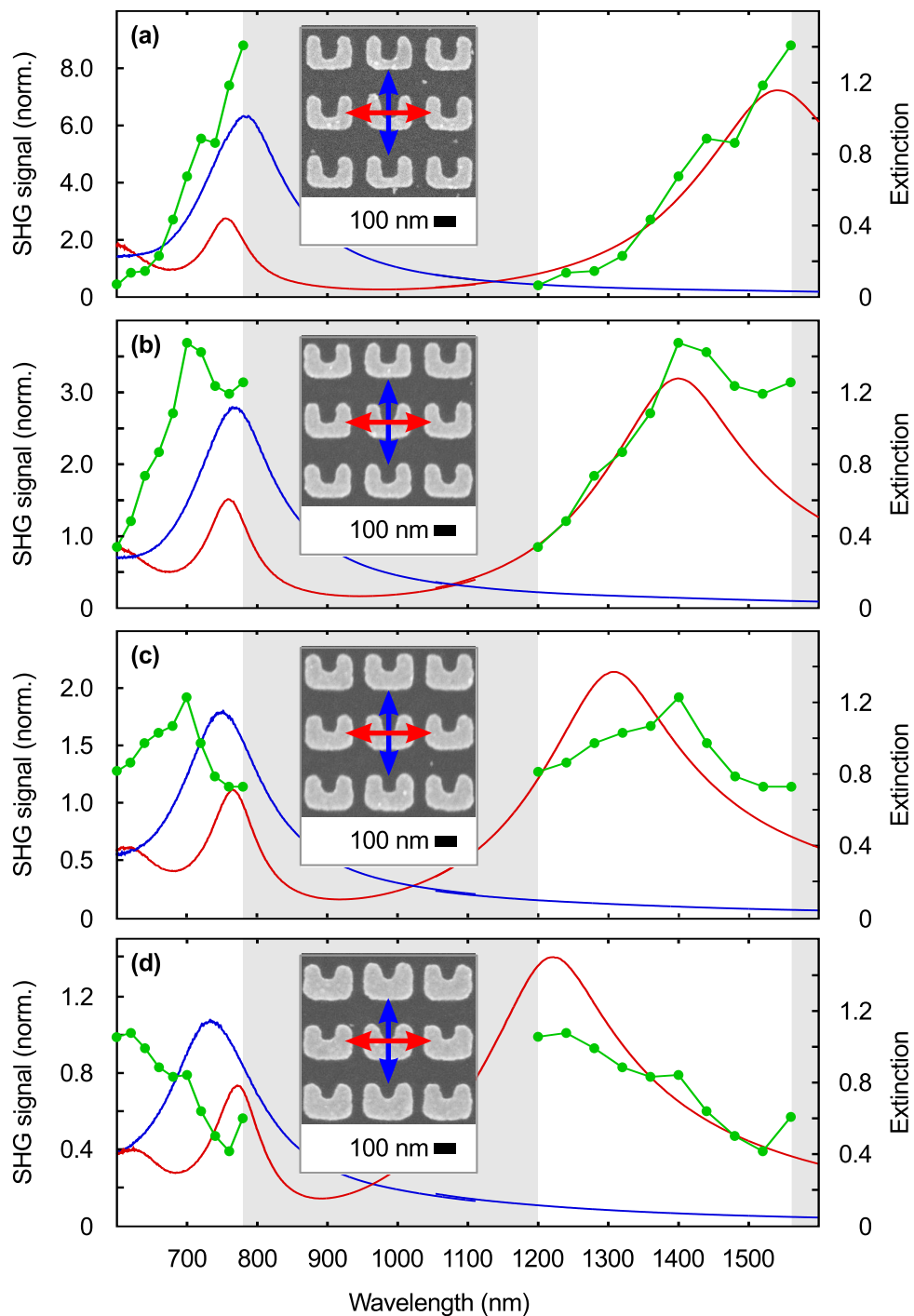


Figure 4.9: Linear and nonlinear measurements on the gap scaled samples - The color coding of the plots is equal to figure 4.8 for an easy comparison. (figure from [55])

4.2 SHG Spectroscopy on Split-Ring-Resonator Arrays

Each SHG data point is intentionally plotted twice in the same spectrum. First, the SHG signal is plotted as a function of the fundamental laser wavelength and second, it is plotted as a function of half of that wavelength. This allows a direct comparison of the SHG spectrum with the linear extinction spectra in these spectral regions. The normal-incidence linear-extinction (negative decadic logarithm of the measured transmittance) spectra are plotted in red and blue curves for horizontal and vertical incident linear polarization, respectively. The grey areas hide the wavelength ranges, that are of no interest with regards to the second harmonic generation, either because these are located outside the tuning range of the OPA (1.2 μm - 1.56 μm) or outside the SHG emission range. Figure 4.9 (a)-(d) shows four experimental results for the set of gap-scaled SRR arrays using the same design of plots.

As already discussed 2.7.1, split-ring resonators show several distinct resonances of which the fundamental magnetic mode has the longest wavelength. The next-higher-order resonances are roughly at twice the frequency of the fundamental magnetic resonance frequency leaving room for speculations about double-resonance conditions. The previous fixed-wavelength experiments [45, 46, 47] could also not clarify the role of the higher-order resonances. For a further analysis of this aspect, we have thus plotted all of our SHG signal data to appear twice in the plots.

One can see in figure 4.8, that the SHG signal reveals a maximum that shifts to longer wavelengths when the size of the SRR is increased, hence shifting the SRR linear resonance positions. From this data, it is not clear whether the SHG maximum correlates with the SRR fundamental magnetic resonance frequency, with the higher-order electric resonances, or with both.

To further investigate this aspect, a second set of samples was fabricated. By systematically changing the shape of the SRR through scaling of the gap-depth d (see figure 4.6), a lithographic tuning of the magnetic resonance relative to the higher-order resonance could be achieved. As can be seen from figure 4.9, the higher-order electric resonances stay approximately fixed while the spectral position of the magnetic resonance is blue shifted from the top to the bottom configuration. These samples also exhibit SHG resonances, however, the comparison with their corresponding linear extinction spectra shows that the SHG maximum is generally not at the same position as the higher-order resonances.

4. NONLINEAR OPTICAL EXPERIMENTS

This can be seen in figure 4.9 (b), where the linear extinction for vertical polarization (blue) peaks about 770 nm wavelength. At this wavelength, the vertically polarized SHG signal (green) exhibits a minimum. The same holds true in 4.9 (c) and (d) with very little spectral shift. In contrast, the linear extinction maximum for vertical polarization (red) in figure 4.9 gradually shifts accordingly. We interpret this behavior as an indication that the fundamental SRR resonance acts as the nonlinear source and that the higher-order SRR resonances reabsorb the generated vertically polarized SHG.

4.2.4 Conclusions

We have performed nonlinear optical spectroscopy on arrays of lithographically tuned gold SRR. From the resulting spectra, a resonance of the second-harmonic generation can be clearly identified. This maximum correlates well with the fundamental resonance but not with the higher-order resonances. The experiment and its results extends and complements very well the previous fixed wavelength experiments [45, 46, 47].

4.3 Collective Effects in Second-Harmonic Generation from Split-Ring-Resonator Arrays

In the last section, we have studied the influence of the spectral position of the resonances on the efficiency of second-harmonic generation conversion. In this section, we investigate the role of the spacing between individual SRR of the array on the conversion efficiency. A design strategy for the most efficient second-harmonic conversion could be to pack the individual SRR as densely as possible. With our experimental results and theoretical investigations we show that collective effects of the individual SRR substantially alter this picture. An optimal behavior is rather found at some intermediate packing density of the individual SRR.

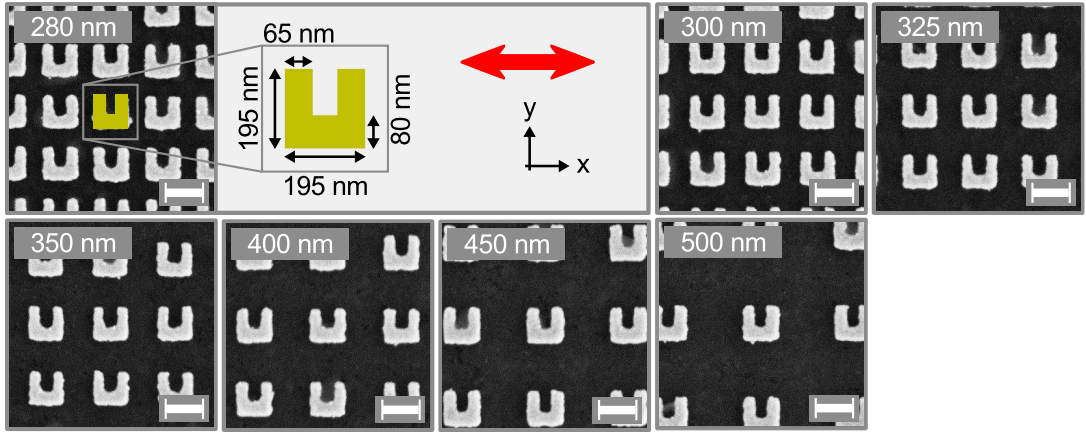


Figure 4.10: SEM images of the selected arrays - The top-view scanning-electron micrographs of the selected gold split-ring resonator arrays are presented that were used for the experiments. The thickness for the gold film is 30 nm and the lattice constant a is indicated for each case. The footprint for each square array is $100 \mu\text{m} \times 100 \mu\text{m}$. Scale bars representing a length of 200 nm are placed as inserts in each micrograph. The yellow SRR illustrates the geometrical dimensions that were used for the theoretical calculations for all a . (figure from [56]).

4.3.1 Sample Fabrication and Linear Optical Characterization

For the experiments we have fabricated samples that exhibit a magnetic resonance at around $1.4 \mu\text{m}$. The individual SRR are arranged on a square lattice with a

4. NONLINEAR OPTICAL EXPERIMENTS

lattice constant a . To study the effect of packing, or equivalently to study the second-harmonic generation (SHG) efficiency versus a , a large set of samples was fabricated in which the electron-beam exposure dose was varied for each of the different lattice constants ($a = 280, 300, 325, 350, 400, 450\text{nm}$). From this set we pick those arrays that exhibit a nearly constant resonance wavelength of about $1.4\ \mu\text{m}$ for their magnetic resonance.

In figure 4.10 one can see that the resulting size variations for the different arrays are extremely small. This aspect is important because resulting changes in the individual SRR properties (e.g., damping) would be an artifact (see also [57]). All arrays have a footprint of $100\ \mu\text{m} \times 100\ \mu\text{m}$ and a gold film thickness of $30\ \text{nm}$.

The measured linear-optical extinction spectra for normal incidence of light are plotted in figure 4.11 on a false color scale. The peak extinction of the fundamental resonance at $1.4\ \mu\text{m}$ wavelength decreases monotonic with increasing lattice constant. This behavior is expected from the dilution and consistent with previous results [57] and can also be found for the higher-order resonance centered around $750\ \text{nm}$ wavelength. Small wiggles in the resonance positions are due to small size variations of the SRR among the different arrays.

4.3.2 Experimental Results and Discussion

Panel (c) of figure 4.11 reveals the measured SHG signal versus center wavelength of the incident laser pulses and versus lattice constant, again depicted on a false-color scale. The experimental setup as well as the normalization method was the same used for the earlier experiment 4.2. In a sharp contrast to the linear optical data, the SHG signals show a non-monotonic behavior versus lattice constant. The SHG signal in figure 4.11 (c) at $1395\ \text{nm}$ excitation wavelength first rises from normalized levels of 1.3 at $280\ \text{nm}$ lattice constant to SHG levels of 3 at $400\ \text{nm}$ lattice constant. For yet larger lattice constants, the SHG decreases and reaches a level of 0.8 at $500\ \text{nm}$ lattice constant. To rule out any effects from the slightly varying SRR resonance wavelength, we have taken complete SHG spectra for each lattice constant.

At each lattice constant, we find the same general non-monotonic behavior. The decay of the SHG signal at very large lattice constants is determined by the decreasing number of oscillators per area or per volume. After all, zero SRR density

4.3 Collective Effects in Second-Harmonic Generation from Split-Ring-Resonator Arrays

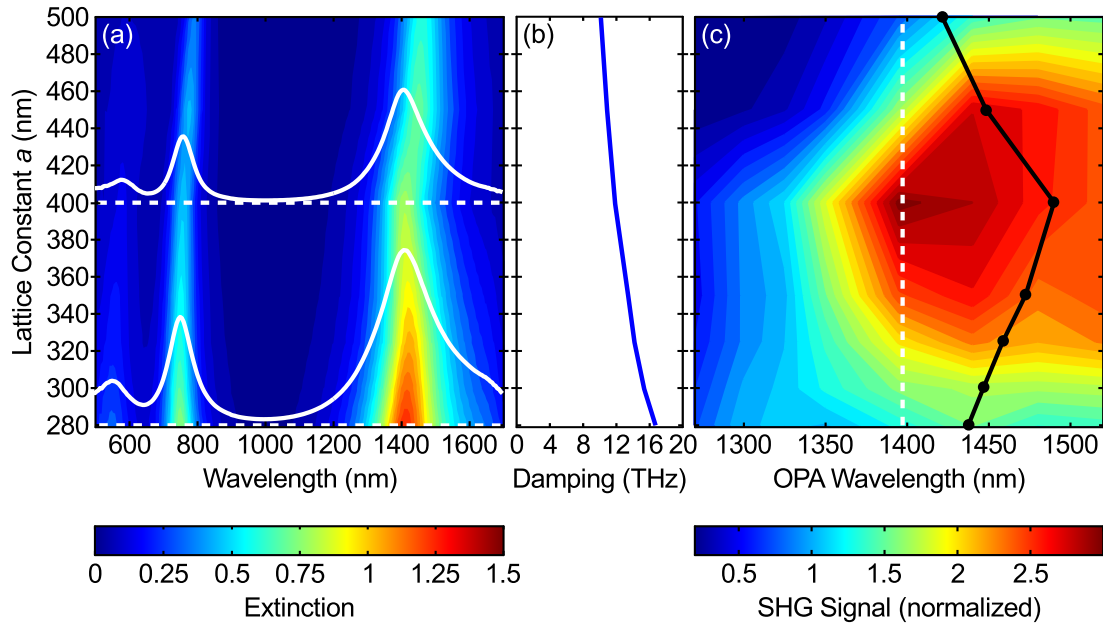


Figure 4.11: Experimental results - (a) Normal-incidence, linear-optical extinction versus wavelength and versus lattice constant a of the SRR square arrays, plotted on a false-color scale. Two selected cuts through these data are shown by the white curves. The white dashed horizontal lines are the respective zero levels. (b) Damping versus lattice constant as obtained from Lorentzian fits to the data in (a). (c) Second-harmonic generation (SHG) signal from the same SRR arrays versus incident fundamental wavelength of the optical-parametric amplifier (OPA) and versus a . The SHG signal is normalized to a quartz reference and plotted on a false-color scale. A selected cut through these data versus lattice constant a is shown by the black curve. The white dashed vertical line is the zero level. note the non-monotonic behavior of the SHG, whereas the linear properties in (a) show a monotonic decay with increasing a . (figure and caption from [56])

4. NONLINEAR OPTICAL EXPERIMENTS

will surely lead to zero SHG from the SRR arrays. By inspecting equation 2.89, this dilution corresponds to a scaling of the second-order nonlinear polarization $\propto 1/a^2$; hence, the SHG signal intensity scales $\propto 1/a^4$. In the opposite limit of very small a , the SRR eventually touch. This is expected to happen at $a = 195$ nm as can be seen from figure 4.10). For this configuration, the SRR resonance disappears, and both, the extinction and the SHG signal are expected to decrease.

However, as becomes clear from the extinction spectra in figure 4.11 (a), a well-defined SRR resonance is observed for all lattice constants investigated. Even at the smallest lattice constant of $a=280$ nm, no drop of the extinction with decreasing a is found. The initial rise of the SHG signal versus lattice constant for small a must, thus, have a different origin.

Intuitively, one might be tempted to suspect some sort of diffractive effect, e.g. brought about by the Wood (or Rayleigh) anomaly [58]. Fortunately, closely similar samples have recently been characterized in detail in linear-optical experiments [57] (also see [59]). For normal incidence of light at the fundamental resonance wavelength, the Wood anomaly occurs at lattice constants larger than about 900 nm. Therefore, diffraction of the incident light into the SRR plane can be ruled out under the present conditions. Diffraction of the SHG signal would also lead to a decrease rather than to the observed initial increase in the (zeroth-order) forward direction but may well contribute to the expected decay of the SHG signal at larger lattice constants.

The optical experiments in [57] also revealed a pronounced decrease of the linewidth of the SRR resonance with increasing lattice constant. For the present samples, the damping γ as obtained from Lorentzian fits to the data shown in figure 4.11 (a) decreases from $\gamma=16$ THz at $a=280$ nm nearly linearly to $\gamma=10$ THz at $a=500$ nm (see figure 4.11 (b)). This dependence can be interpreted as being due to a retarded long-range interaction among the SRR in the arrays [57].

By again recalling equation 2.89, we see that the linewidth of the resonance also enters sensitively into the second-order nonlinear-optical susceptibility $\chi^{(2)}$. In addition, the amplitude of local-field-enhancement increases with decreasing damping as this strongly influences the quality factor of the resonance, leading to an increase of the overall SHG intensity. Moreover, the spatial distribution of the local SRR fields also enters sensitively into the SHG conversion efficiency.

4.3 Collective Effects in Second-Harmonic Generation from Split-Ring-Resonator Arrays

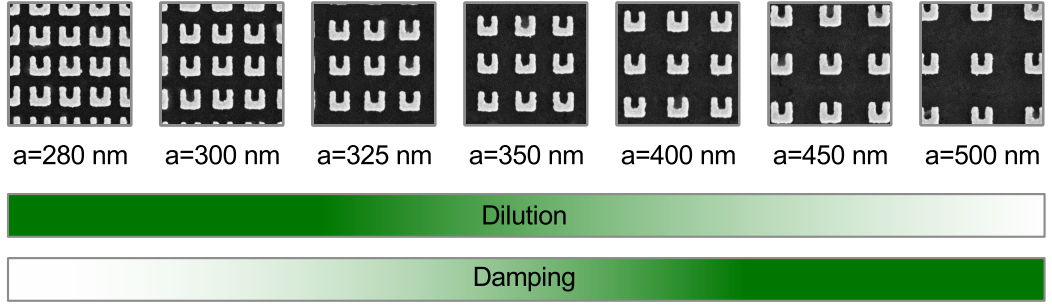


Figure 4.12: Illustration of the competing effects - With increasing lattice constant, the number of SRR per unit area decreases. This dilution effect leads to a decreasing SHG signal strength as illustrated by the green gradient in the top bar. On the other hand, an increase in lattice constant reduces the damping of the fundamental resonance that leads to an increase of the SHG signal (green gradient in the bottom bar).

Combined with the trivial dilution effect discussed above, these aspects can qualitatively explain the measured non-monotonic behavior of the SHG signal versus lattice constant.

To test this qualitative reasoning quantitatively and to rule out any experimental artifacts, we have performed numerical calculations using the discontinuous Galerkin time-domain method [60, 61] for the experimentally investigated gold split-ring-resonator square arrays. We describe the optical response of the metal by the state-of-the-art hydrodynamic Maxwell-Vlasov theory [33, 62]. Its linear limit corresponds to the Drude free-electron model, for which we have chosen a plasma frequency $\omega_{\text{pl}} = 1.33 \times 10^{16} \text{rad/s}$, a collision frequency $\omega_{\text{col}} = 8 \times 10^{13} \text{rad/s}$, and a background dielectric constant of $\epsilon_{\infty} = 9.84$. The refractive index of the glass substrate is taken as $n = 1.46$. The geometric SRR parameters (which are the same for all lattice constants a) are according to the yellow SRR in figure 4.10.

The current density \mathbf{j} was used in the form (see also supplementary material [56])

$$\frac{\partial \mathbf{j}}{\partial t} = \frac{n_0 e^2}{m_e} \mathbf{E} - \gamma \mathbf{j} - \frac{e}{m_e} [(\nabla \cdot \mathbf{E})(E) + \mathbf{j} \times \mu_0 \mathbf{H}] + \frac{1}{en_e} (\mathbf{j} \cdot \nabla) \mathbf{j} + \frac{e}{m_e} \nabla p, \quad (4.5)$$

where the first two terms represent the linear Drude model with the plasma frequency $\omega_{\text{pl}} = \sqrt{n_0 e^2 / (\epsilon_0 m_e)}$ and the damping constant γ . The number density of the ionic cores is represented by n_0 and e is the elementary charge and m_e

4. NONLINEAR OPTICAL EXPERIMENTS

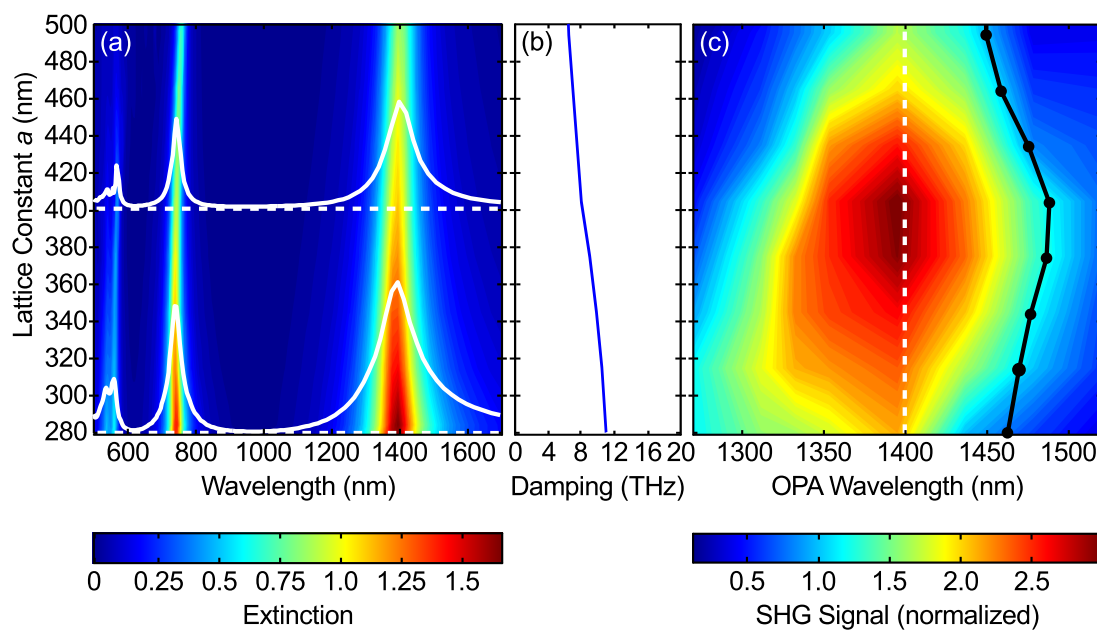


Figure 4.13: Results of the theoretical calculations - The calculations correspond to the experiment in figure 4.11. The representation is the same, allowing for direct comparison. The geometrical parameters used for split-ring resonators are shown at the top of figure 4.10. Panel (c) uses the hydrodynamic Maxwell-Vlasov theory to describe the nonlinear response of the gold split-ring resonators. (figure from [56])

4.3 Collective Effects in Second-Harmonic Generation from Split-Ring-Resonator Arrays

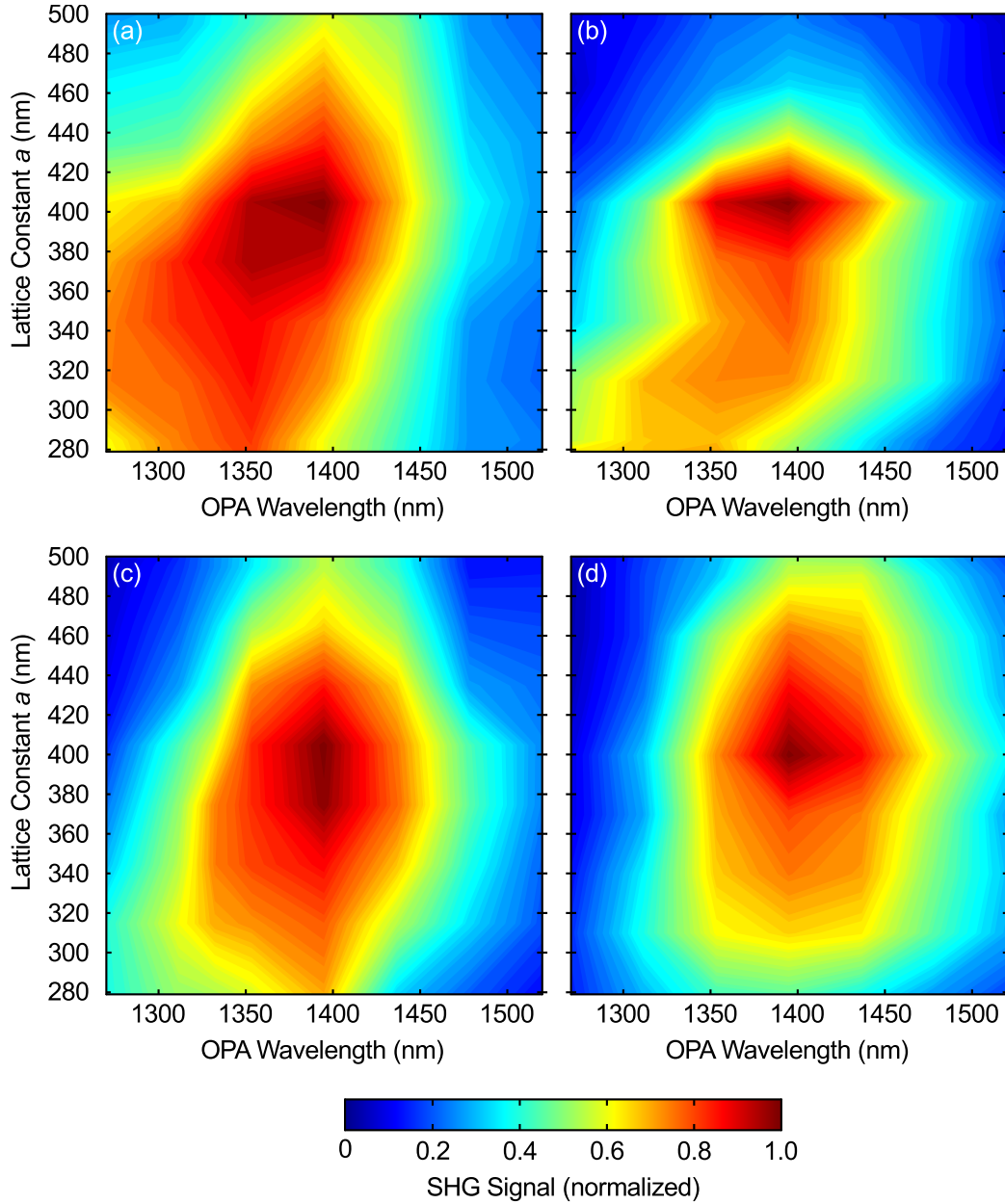


Figure 4.14: Comparison of the different nonlinear models - SHG signal versus incident fundamental wavelength and versus lattice constant a for different nonlinear approaches. (a) complete hydrodynamic Maxwell-Vlasov theory, (b) uses only the Fermi pressure term ∇p within the Maxwell-Vlasov theory. In (c) and (d) a simple generic model with a single nonlinear susceptibility tensor component $\chi_{yy}^{(2)}$ and $\chi_{yxx}^{(2)}$, respectively. (supplementary material from [56])

4. NONLINEAR OPTICAL EXPERIMENTS

the mass of the electron. ϵ_0 and μ_0 represent the dielectric constant and the vacuum permeability, respectively. The nonlinearity is induced by the electric and magnetic Lorentz force terms, a convective acceleration term $(\mathbf{j} \cdot \nabla)\mathbf{j}$, and the semi-classical electron-gas Fermi pressure p , that is a function of the electron number density n_e :

$$p = \frac{1}{5}(3\pi^2)^{\frac{2}{3}} \frac{\hbar}{m_e} n_e^{\frac{5}{3}}. \quad (4.6)$$

Figure 4.13 (a) shows a calculated linear-optical extinction spectra. These calculations reproduce the experimentally observed monotonic decrease of the extinction peak and of the damping (see figure 4.13 (b)) with increasing lattice constant a . The nonlinear SHG calculations are depicted in 4.13 (c). We find a pronounced maximum of the SHG signal versus lattice constant at about $a = 400$ nm throughout the entire spectral resonance. This non-monotonic behavior versus lattice constant nicely reproduces the experimental findings shown in figure 4.11 (c). Thus, the numerical results strongly support the above qualitative reasoning in that the SHG signal is strongly influenced by collective effects via the SRR damping as well as via the SRR near-field distributions.

Since the detailed microscopic mechanism of the metal nonlinearity is still subject to debates we have also performed calculations using other models for the nonlinearity. In particular, this includes a simple generic treatment with an effective instantaneous second-order nonlinear susceptibility for the gold SRR

$$P_i^{(2)} = \epsilon_0 \chi_{ijk}^{(2)} E_j E_k. \quad (4.7)$$

This nonlinear polarization is non-zero for the gold SRR and zero elsewhere within the simulation domain. For the simulations, two different cases with non-zero components of the nonlinear susceptibility tensor $\chi_{yyy}^{(2)}$ and $\chi_{yxx}^{(2)}$. All other elements of the tensor are set to zero.

In figure 4.14 a comparison of the SHG signal strength versus wavelength of the fundamental light and versus lattice constant for the different nonlinear models is presented. All of the simulation results exhibit a similar qualitative behavior, in particular they all show the non-monotonic behavior of the SHG signal versus lattice constant. The resulting signal maximum occurs around a lattice constant of about 400 nm in all cases.

4.3 Collective Effects in Second-Harmonic Generation from Split-Ring-Resonator Arrays

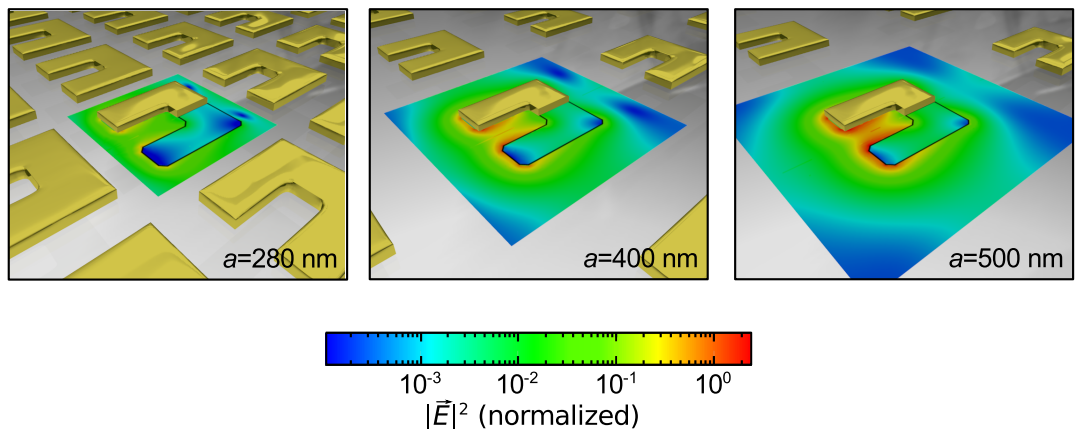


Figure 4.15: Calculated near-field distributions - The distributions for three different lattice constants a as obtained from numerical calculations with parameters as in figure 4.13. The square modulus of the electric-field vector, $|\vec{E}|^2$, at the fundamental SRR resonance frequency is shown on a logarithmic false-color scale. The normalization is the same for all three panels. For clarity, half of the golden SRR in one unit cell is rendered transparent. For the lattice constants shown, an increase of the SRR lattice constant a leads to an increase of the strength of the near and internal fields and to a larger SHG far-field signal. At yet larger lattice constants, this trend is reversed by the trivial dilution effect. (from [56])

4. NONLINEAR OPTICAL EXPERIMENTS

These results confirm the fundamental nature of the reported non-monotonic behavior. However, none of these calculations is able to precisely reproduce the asymmetry of the spectral SRR resonance shown in figure 4.11 (c).

In figure 4.15, the origin of the collective effects as already qualitatively discussed above is illustrated. Indeed, the SRR near fields within one unit cell at the fundamental resonance frequency depends on the lattice constant. Stronger near fields lead to stronger internal currents and hence to larger SHG signals. Once the SRR are separated by more than the extent of their near-fields, these fields no longer increase with increasing a and the SHG signal eventually decreases due to the trivial dilution effect.

4.3.3 Conclusions

In our experiment, we have observed a non-monotonic behavior of the resonant second-order nonlinear conversion efficiency in SRR arrays versus packing density. The theoretical modeling indicates, that this finding is a rather general phenomenon based on collective effects among the metamaterial building blocks and that should occur in many nonlinear metamaterials. Thus, future experiments aiming at achieving large effective optical nonlinearities should keep these collective effects in mind.

5

Thermal Detectors

In this chapter, an introduction to the basics of thermal detectors is given. This provides the foundation for the metamaterial bolometer experiment in the next chapter. Basically, two main types of detectors can be distinguished for the detection of electromagnetic radiation in the infrared spectral region. The first type is represented by the group of quantum detectors, where light is directly converted into free electrons in the conduction band of a semiconductor material. Dependent on the semiconductor used and the detector setup, these devices work either as a photoresistor (indium antimonide InSb), a photovoltaic cell (indium arsenide InAs) or a photodiode (germanium Ge). These type of detectors offer a high detection performance combined with a fast response speed, but their photosensitivity is wavelength dependent [63] and they often have to be cooled for accurate measurements.

The second type of infrared detectors is represented by the thermal detectors [64]. Here, the detection process is initiated by an absorption of radiation power and a subsequent conversion into thermal energy. This leads to a heating and a temperature increase of the detector that is then measured. In essence, this kind of detector is a radiation heated thermometer. These detectors can be tailored to respond to a broad range of wavelengths and offer a good performance at room temperature operation. Conceptually, thermal detectors can be used to detect any kind of radiation energy as long as a thermalization through absorption is possible within the detector material.

We will now take a closer look on the basic working principle of a thermal detector. The detector schemes differ by the way the temperature increase is

5. THERMAL DETECTORS

read out [65]. Table 5.1 gives an overview of the physical detection mechanisms and their implementations. In case of the thermocouple, the connection of two

physical effect	detector type
seebeck effect	thermocouple or thermopile
pyroelectricity	pyroelectric sensor
pressure change	golay cell
resistance change	bolometer

Table 5.1: The four physical mechanisms for thermal detector implementations

different metal or metal alloy wires leads to a potential difference at the open ends of the circuit. The potential difference depends on the temperature difference between the connection point and the open ends (Seebeck effect) and can therefore be used to infer on the temperature change of the detector. A connection of additional thermocouples in series is called a thermopile and increases the potential difference between the open ends.

The pressure and volume of a gas depends strongly on the temperature as described by the ideal gas law. This effect is used within a pneumatic detector or golay cell [66]. Here, the detector chamber is filled with a gas and sealed with a deformable membrane. Radiation striking the detector then heats the gas inside the chamber. The gas warms up and the membrane is deformed due to the increased internal pressure. By measuring the deformation of the membrane, one can therefore infer on the absorbed radiation.

Another physical mechanisms that can be used within a thermal detector is the temperature dependent electric polarization that can be found in some crystals (e.g., deuterate triglycine sulfate (dTGS), lithium tantalate (LiTaO₃), lead zinc titanate (PZT)). Within this pyroelectric effect, the change of polarization with temperature alteration is accompanied with an electrical current that is measured to infer on the temperature change.

One of the first implementations of a thermal detector goes way back to the end of the 19th century. In 1880 Samuel P. Langley used the property of metals to change their electrical resistance as a function of temperature as a measure to detect the absorption of infrared radiation [67]. This working principle is the basis for all modern bolometer implementations. As detector materials, metals

and semiconductors which exhibit a strong dependence of their electrical resistance on temperature are used. By using thin films of the materials, the thermal mass can be kept low enhancing the response time of the detector [68, 69, 70]. Bolometers can work under room temperature conditions and normal air pressure, but top performance is obtained under low temperature conditions and vacuum. Compared to quantum detectors, their response time is rather low [71].

5.1 Thermal Model

To understand the detection mechanism in more detail, the temperature increase due to absorption of radiation can be modeled using the heat diffusion equation. A thermal detector consists of an absorber with heat capacity C_{th} that is connected to the heat sink at Temperature T_0 via a thermal conductance G_{th} . Radiation striking the absorber then leads to heating of the absorber element which results in an elevated temperature T_1 .

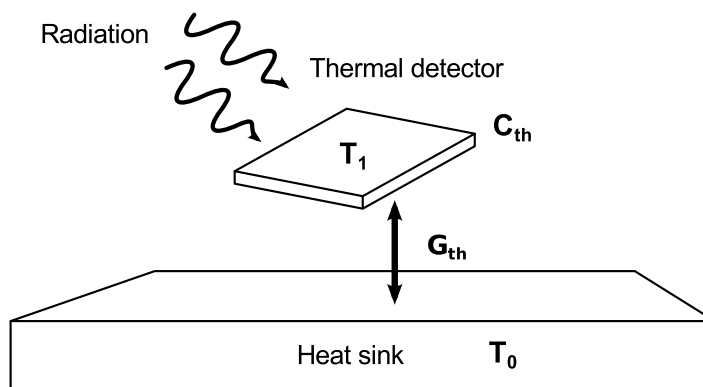


Figure 5.1: Sketch of a thermal detector - The absorptive element is thermally connected to a heat sink described by a thermal conductivity G_{th} . The absorption of radiation leads to a temperature increase $\Delta T = T_1 - T_0$ of the detector which is measured.

This thermal system can be modeled by solving the corresponding heat balance equation

$$C_{th} \frac{d\Delta T}{dt} + G_{th} \Delta T = \epsilon \Omega \quad (5.1)$$

5. THERMAL DETECTORS

where C_{th} defines the detectors thermal capacity and G_{th} depicts the total thermal conductivity of the detector to its surroundings.

When thermal radiation of power Ω modulated with the angular frequency ω

$$\Omega = \Omega_0 e^{i\omega t} \quad (5.2)$$

strikes the detector, the temperature increase ΔT is given as a solution [72] to equation 5.1

$$\Delta T = \frac{\epsilon \Omega_0 e^{i\omega t}}{G_{\text{th}} + i\omega C_{\text{th}}} = \frac{\epsilon \Omega_0}{G_{\text{th}} \sqrt{1 + \omega^2 \tau_{\text{th}}^2}}. \quad (5.3)$$

The time constant τ_{th} is given by

$$\tau_{\text{thermal}} = \frac{G_{\text{th}}}{C_{\text{th}}} \quad (5.4)$$

and describes the temperature increase of the detector after a signal applied for time t

$$\Delta T = \frac{\Omega_0}{G_{\text{th}}} e^{-t/\tau_{\text{th}}}. \quad (5.5)$$

Obviously the detector temperature increases linearly with the amount of absorbed energy $\epsilon \Omega_0$.

5.1.1 Heat Exchange Mechanisms

Materials reach their thermal equilibrium through three basic heat exchange mechanisms, namely conduction, convection and radiation [73]. All these mechanisms add up to the overall thermal conductance G_{th} of the bolometer.

$$G_{\text{th}} = G_{\text{conduction}} + G_{\text{convection}} + G_{\text{radiation}} \quad (5.6)$$

As we have seen, the thermal conduction strongly affects the performance of the bolometer. To achieve the highest temperature increase of the detector for a given amount of absorbed energy the thermal conductivity has to be as low as possible. In the next section, we will give an overview over the various physical mechanisms affecting the overall thermal conductivity.

Thermal Conduction

When two bodies at different temperature are in thermal contact, heat flows from the body at higher temperature to the one at the lower temperature. In solid materials, the heat flow is due to vibrations of the molecules in the lattice or by lattice vibrations itself, the phonons. Free electrons can also carry heat and contribute to the heat transfer. The collision and diffusion of molecules are responsible for the heat conduction in gases and liquid materials.

The mathematical law of heat conduction is known as Fourier's law. In its differential form, the local heat flux density \mathbf{q} [$W \cdot m^{-2}$] is proportional to the magnitude of the temperature gradient

$$\mathbf{q} = -\kappa \nabla T, \quad (5.7)$$

where the minus sign illustrates the fact, that heat flows from the higher temperature area to the lower temperature. The thermal conductivity κ [$W \cdot K^{-1} \cdot m^{-1}$] characterizes the materials ability to conduct heat and is often treated as a constant. Generally, the thermal conductivity is temperature dependent, but can be approximated as constant over a broad range of temperatures for the most common materials.

To get a representation of the thermal conductance, we consider the heat Q flowing through a cross-section area A [m^2] of a rod of length d . Fourier's law can be reduced to a one-dimensional representation

$$q_z = -\kappa \frac{dT}{dz} \quad (5.8)$$

which eases the calculation. The integral form of the above equation then has the form

$$\frac{\partial Q}{\partial t} = \int_A q_z dA = -\kappa \int_A \frac{dT}{dz} dA. \quad (5.9)$$

Integrating of the above equation leads to

$$\frac{\Delta Q}{\Delta t} = \kappa \frac{A}{\Delta z} \Delta T, \quad (5.10)$$

where ΔT is the temperature difference and Δz is the distance d between both ends. The thermal conductance G_{th} [W/K] is then

$$G_{th} = \frac{\kappa A}{d}. \quad (5.11)$$

5. THERMAL DETECTORS

The electrical analog of the Fourier law is Ohm's law. This can immediately be seen from equations 5.10 and 5.11 when directly comparing them with Ohm's law

$$\dot{Q} = G \cdot \Delta T \leftrightarrow I = \frac{1}{R} \Delta U. \quad (5.12)$$

From this we can draw analogies between thermal and electrical quantities as presented in table 5.2. Due to this analogies it is possible to use circuit theory for solving static and even dynamic heat conduction problems [74]. In the context of bolometers this is exploited to model the thermal behavior of the detector using simulation tools for standard electronic circuits [75, 76].

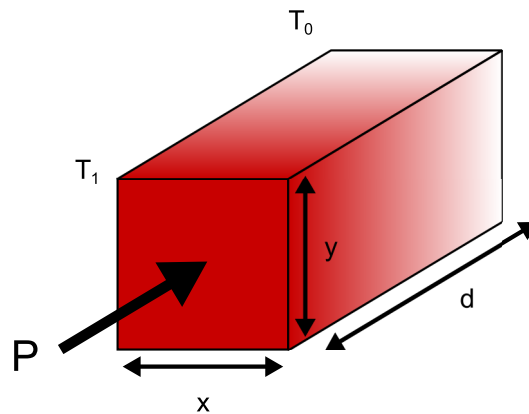


Figure 5.2: Thermal resistance - Thermal resistance $R_{th} = d/(\kappa \cdot A)$ of a block with thickness d and cross sectional area $A = x \cdot y$. The thermal power $P = \dot{Q}$ leads to a temperature difference $\Delta T = T_1 - T_0$

Convection

The heat transfer through convection can only be found in viscous materials like fluids or gases. In contrast to heat conduction, the molecules collectively move to transport the heat accompanied by a transfer of mass. In the context of thermal detectors, convection effects are often eliminated by operating the detectors in a vacuum environment on the same time also reducing the thermal conduction through the gas. More details on the mechanisms of convection can be found in [73]

Radiation

A third way to exchange energy with the surroundings is through the emission of thermally emitted photons. The intensity of such an energy flux depends on the temperature of the emitting body. The spectral energy density for a perfect absorber is given through Planck's law

$$\rho(\lambda, T) = \frac{8\pi hc}{\lambda^5 (e^{hc/\lambda k_B T} - 1)}, \quad (5.13)$$

with the Planck constant h , the speed of light c , the thermal energy $k_B T$, and the wavelength λ of light. In case of a deviation from a perfect absorber, Planck's law will be modified by the factor $\epsilon(\lambda)$, describing the emissivity as a function of the emitting wavelength. According to Kirchhoff's law of thermal radiation, emissivity and absorption are equal and will strongly depend on the material. Albeit this effect is the ultimate performance limit of a thermal detector design, in practical applications the heat transfer by conduction is the dominating process, especially in the context of bolometers [77, 78].

5.1.2 Thermal Capacity

The thermal capacity or heat capacity is the thermal quantity affecting the dynamic behavior of the detector. To maintain a short response time, the thermal capacity of the detector design should be as low as possible. The thermal capacity C_{th} is directly proportional to the relevant detector volume V [cm³], to the density of the material ρ [g/cm³] and to a proportionality factor of the specific heat c [Ws/g · K]:

$$C_{th} = c \cdot \rho \cdot V = m \cdot c. \quad (5.14)$$

The thermal capacity of a body of mass $m = \rho \cdot V$ corresponds to the quantity of heat needed to heat the body by 1°C. By again using the analogy of electrical and thermal quantities we can compare the thermal capacity with the electrical capacity:

$$\Delta T \cdot C_{th} = P \cdot t = Q \leftrightarrow \Delta U \cdot C_{el} = I \cdot t = Q. \quad (5.15)$$

For a fast detector response it is therefore necessary to reduce the mass of the detector by using a small detector volume and/or low density materials.

5. THERMAL DETECTORS

Table 5.2: The analogies between electric and thermal quantities

Current $I = \dot{Q}$	Heat flow \dot{Q}
Voltage difference ΔU	Temperature difference ΔT
Electrical conductance G_{el}	Thermal conductance G_{th}
Electrical resistance $R = 1/G_{\text{el}}$	Thermal resistance $R_{\text{th}} = 1/G_{\text{th}}$
Capacitance C_{el}	Thermal capacity C_{th}

6

Metamaterial Metal Bolometer

Metamaterial resonances are the basis for their extraordinary material properties. These resonances are usually based on plasmonic excitations of the metal-based structures. Unfortunately, causality connects these resonances with large imaginary parts of the corresponding dielectric function leading to losses [79, 80], often unwanted in technical applications of metamaterials [81].

But the metamaterial community has searched for ways to profit from the inherent absorption and came up with the idea of the perfect absorber, neither transmitting or reflecting light in a delimited range of frequencies. This concept was investigated both theoretically and experimentally [12, 15, 16, 82, 83] and has led to applications in the context of plasmonic sensors [13]. The absorption of metamaterials was also used to tailor the thermal-emission behavior of the material. It makes use of Kirchhoff's law of thermal radiation that connects the wavelength-specific absorption and emission properties of a material [15]. Recently, a metamaterial structure was used to build an Schottky photodiode with tailorable built-in spectral filters [84]. The accessible wavelength range is limited by the height of the involved Schottky barrier for the semiconductor-metal interface. Several other experimental works have focussed on the absorption of metamaterials and their use in sensing [14, 85, 86].

Based on the idea of the metamaterial metal-based bolometer, a flexible device for the detection of infrared radiation can be implemented. We used a slightly modified split-ring resonator structure which allowed us to not only tailor the spectral absorption behavior of the structure, but also use the metal of the structure as a thermistor. That way, a wavelength and polarization-sensitive device

6. METAMATERIAL METAL BOLOMETER

for the detection of radiant energy in the infrared spectral region was build and characterized.

The following chapter first discusses the basics of metal bolometers in general. Then, the thermal characterization of the bolometer device is addressed. Finally, the full experimental characterization of the fabricated device is presented.

6.1 Basics of Metal Bolometers

In the case of a resistive bolometer, the temperature dependent change of a metal's resistance is used to measure the temperature increase of the detector. Metals like gold or platinum have a sufficient high temperature coefficient of resistance (TCR). The temperature dependent resistance of the metal is described with

$$R(T) = R_0(1 + \alpha(T - T_0)), \quad (6.1)$$

where R_0 is the electrical resistance at the reference temperature T_0 . The temperature coefficient of resistance (TCR) $\alpha [K^{-1}]$ has positive values for metals. In the case of negative temperature coefficient (NTC) materials, heating of the material decreases its resistance, a behavior found in semiconductor bolometers.

The most simple setup of bolometer operation is illustrated in figure 6.1. Here the bolometer is connected in series with a load resistor R_L with a much higher resistance than the bolometer resistance $R_B(T)$. This allows an operation of the bolometer under a constant bias current condition. By measuring the bolometers resistance change, one then can infer on the absorbed optical power. We will now take a closer look on how to model the behavior of the detector.

When the bolometer is biased with a constant current I_b , electrical power P_e is dissipated within the device. This leads to a temperature increase of the bolometer through the process of Joule's heating. The average temperature \bar{T} of the bolometer is determined by the thermal insulation G_{th} . The corresponding heat balance equation without optical input power present is given by [87]

$$G_{th}(\bar{T} - T_a) = P_e = I_b^2 R_b = I_b U_b \quad (6.2)$$

where T_a and U_b denote the ambient temperature and the voltage accross the bolometer, respectively. The sensor's resistance at the average temperature is given by

$$R_b = R_{b0}[1 + \alpha_0(\bar{T} - T_0)]. \quad (6.3)$$

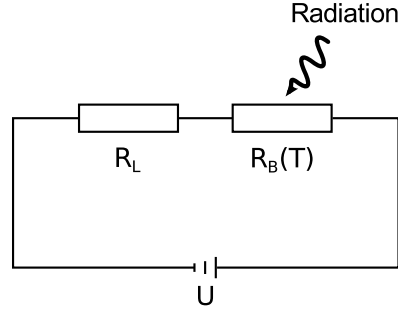


Figure 6.1: Simple electric circuitry - The bolometers electrical resistance $R_B(T)$ is in series with the load resistance R_L . The load resistance is chosen to fulfill $R_L \gg R_B(T)$ to maintain a constant bias current through the bolometer.

To study the effect of the optical input power modulated with the angular frequency ω

$$\Omega(t) = \Omega_0 e^{i\omega t} \quad (6.4)$$

striking the detector, the lumped bolometer equation [87] has to be solved:

$$C_{th} \frac{dT}{dt} + G_{th}(T - T_a) = I_b^2 R_b + \epsilon \Omega(t). \quad (6.5)$$

As a reminder, C_{th} denotes the heat capacity of the detector and ϵ is the spectral absorbance. Using equation 6.3 and the resistance at the ambient temperature T_a

$$R_a = R_{b0}[1 + \alpha(T_a - T_0)] \quad (6.6)$$

we can rewrite equation 6.5

$$H \frac{dT}{dt} + (G_{th} - I_b^2 R_{b0} \alpha_0)(T - T_a) = I_b^2 R_a + \epsilon \Omega(t). \quad (6.7)$$

As we are interested in the temperature perturbation ΔT caused by the optical signal we write $T = \bar{T} + \Delta T$ and substitute this into the last equation. We also deduct the static terms and finally arrive at [87]

$$H \frac{d\Delta T}{dt} + (G - I_b^2 R_{b0} \alpha_0) \Delta T = \epsilon \Omega(t). \quad (6.8)$$

The spectral thermal responsivity is obtained as a solution to the above equation as

$$R_{Th} = \frac{\epsilon}{G_{th} - I_b^2 R_{b0} \alpha_0} \frac{1}{\sqrt{1 + \omega^2 \tau^2}}, \quad (6.9)$$

6. METAMATERIAL METAL BOLOMETER

where the effective time constant is

$$\tau = \frac{C_{\text{th}}}{G_{\text{th}} - I_b^2 R_{b0} \alpha_0}. \quad (6.10)$$

When characterizing the performance of a bolometer, often the electrical responsivity \mathfrak{R} is used:

$$\mathfrak{R} = \frac{dU_b}{d\Omega(t)} = \frac{dU_b}{dR} \cdot \frac{dR}{dT} \cdot \frac{dT}{d\Omega(t)} \quad (6.11)$$

$$= I_b \cdot R_{b0} \alpha_0 \cdot R_{Th}. \quad (6.12)$$

Inserting equation 6.9 finally results in

$$\mathfrak{R} = \frac{\epsilon I_b R_{b0} \alpha_0}{G_{\text{th}} - I_b^2 R_{b0} \alpha_0} \cdot \frac{1}{\sqrt{1 + \omega^2 \tau^2}}. \quad (6.13)$$

Due to the effect of the electro-thermal feedback mechanism, the effective thermal conductivity $G_{\text{eff}} = G_{\text{th}} - I_b^2 R_{b0} \alpha_0$ differs from the thermal conductivity G_{th} . The effect of Joule's heating also limits the magnitude of the bias current. For a metal bolometer with $\alpha_0 > 0$, a current of $I_b = \sqrt{G_{\text{th}}/(R_{b0} \alpha_0)}$ leads to a divergence of the responsivity, called the thermal runaway. The magnitude of the bias current is therefore limited for practical applications to $I_{b,max} \approx 0.5 \sqrt{G_{\text{th}}/(R_{b0} \alpha_0)}$ [88].

6.2 Thermal Characterization of the Bolometer

The thermal conductance G_{th} is the most important parameter for the evaluation of the performance of a bolometer. The measurement of the thermal conductance can be achieved by generating heat in the detector and simultaneously measuring the increase in temperature. As a heat source, the absorption of thermal radiation could be used. But this bolometric method is rather complicated, because the accurate measurement of the absorbed optical power is difficult. Another way to experimentally determine the thermal conductance can be done by the DC method. Here the device is biased with a constant current and the effect of the dissipation of electrical power within the bolometer is exploited as a heat source. Using the relation

$$G_{\text{th}} \Delta T = I_b^2 R_b \quad (6.14)$$

6.2 Thermal Characterization of the Bolometer

combined with the temperature dependence of the resistance, one obtains

$$\frac{R_b \cdot R_{b0}}{R_b - R_{b0}} = -\frac{\alpha}{G} I^2. \quad (6.15)$$

Using this relation, a measurement of the resistance of the bolometer as a function of the bias current squared, reveals the factor α/G_{th} .

To deduce the thermal conductance from the above measurement, the TCR α must be known to deduce the thermal conductance G_{th} which can be easily obtained from a separate measurement [89]. The device is externally heated, starting from the temperature T_0 , and the change in resistance $\Delta R = R(T) - R_0$ together with the temperature $T > T_0$ is logged. Plotting the function 6.1

$$\Delta R = \alpha(T - T_0) \quad (6.16)$$

reveals the TCR α by linear curve fitting.

The DC method has some major drawback. When evaluating G_{th} from equation 6.15, its accuracy is very sensitive to changes in the reference temperature T_0 . Due to small denominator $R_b - R_{b0}$, tiny changes in the environmental temperature lead to a variation within R_b and in turn to a large error in determining G_{th} . For an accurate measurements the reference temperature in the vicinity of the detector should therefore be monitored carefully using an additional temperature sensor.

To overcome these drawbacks, we have used the so-called 3ω method for the characterization of our bolometer. In addition, this method also allows the characterization of the dynamical behavior of the bolometer, *i.e.* the time constant τ .

The 3ω Method

The concept of the 3ω method is based on using an AC current to feed a thin metal strip that acts both as a heater and temperature sensor [90, 91]. The current is sinusoidally oscillating at the fundamental frequency ω . Due to the dissipation of electrical energy within the metal strip, the temperature is oscillating at twice the fundamental frequency 2ω . The linear dependence of the strips resistance on the temperature 6.1 leads to an oscillation of the resistance with the frequency 2ω . This in turn leads to a voltage oscillation across the strip having a component

6. METAMATERIAL METAL BOLOMETER

at 3ω . Measuring this voltage oscillation allows one to characterize the thermal environment of the heater, namely the thermal insulation or thermal conductance [92, 93]. In addition, this method also allows the determination of the thermal capacity of the heated material when also the frequency dependence of the voltage oscillation is measured [94].

As shown in reference [95], this principle can be applied to the characterization of a metal bolometer. They have used a combination of a constant current together with an oscillating current. Here we use their derivation but use only an AC current $I_b = I \cdot \cos(\omega t)$ to bias the bolometer. The heat balance equation then reads

$$C_{th} \frac{dT}{dt} + [G_{th} - I^2 \cos^2(\omega t) \cdot \alpha_0 R_{b0}] \cdot (T - T_0) = \frac{I^2 R_{b0}}{2} \cos(2\omega t). \quad (6.17)$$

The temperature oscillation $\Delta T = T - T_0$ can be solved analytically from the above equation as [95]

$$\Delta T = e^{-k(t)} \int e^{k(t)} \cdot I^2 \frac{R_{b0}}{2C_{th}} \cos(2\omega t) dt + c_0 e^{-k(t)} \quad (6.18)$$

where $k(t)$ is given by

$$k(t) = \frac{1}{C_{th}} (G_{th} - \frac{1}{2} \cdot I^2 \alpha_0 R_{b0}) t - I^2 \alpha_0 \frac{R_{b0}}{4C_{th}\omega} \sin(2\omega t). \quad (6.19)$$

The integration constant c_0 depends on the initial condition and quickly vanishes in several thermal time constants. It is therefore valid to assume a steady-state condition where $c_0 = 0$. For the further discussion we set $G_{eff} = G_{th} - 1/2 \cdot I^2 \alpha_0 R_{b0}$ and neglect the last term in 6.19 to obtain the time dependent temperature oscillation

$$\Delta T = \frac{I^2 R_{b0}}{2G_{eff} \sqrt{1 + (2\omega\tau)^2}} \cos(2\omega t + \phi) \quad (6.20)$$

with the time constant $\tau = C_{th}/G_{eff}$.

The voltage across the bolometer then is given by

$$U_b(t) = I_b(t) \cdot R_b(t) \quad (6.21)$$

$$= I \cos(\omega t) \cdot R_{b0} (1 + \alpha_0 \Delta T) \quad (6.22)$$

and together with 6.20 we have finally

$$U_b(t) = R_{b0}I \cos(\omega t) + \frac{I^3 R_{b0}^2 \alpha_0}{4G_{eff} \sqrt{1+(2\omega\tau)^2}} \cos(\omega t + \phi) \quad (6.23)$$

$$+ \underbrace{\frac{I^3 R_{b0}^2 \alpha_0}{4G_{eff} \sqrt{1+(2\omega\tau)^2}}}_{U_{b,3\omega}} \cos(3\omega t + \phi). \quad (6.24)$$

The frequency component of the voltage $U_{b,3\omega}$ that oscillates with three times the fundamental frequency is of special interest. Its magnitude directly relates to the effective thermal conductance G_{eff} and from its frequency dependent behavior we can also determine the effective time constant τ .

6.3 Experimental Setup

The characterization of the metamaterial bolometer was done with the experimental setup sketched in figure 6.2. For the optical characterization we have used an optical parametric oscillator (OPO) ¹ as a tunable narrow band light source. The tuning range of the OPO is from 1.2 μm up to 1.8 μm . The beam passes a half-wave plate and a polarizer. By turning the half-wave plate and keeping the polarizer position fixed, the power of the OPO impinging on the sample can be adjusted. In addition, by turning the polarizer, the polarization angle can be arbitrarily adjusted. This allows a polarization dependent spectroscopy of the sample without the need to turn the sample itself.

To monitor and set the appropriate power on the sample, a movable power meter can be placed right after the polarizer which is removed right before the measurement. The beam from the OPO is then focussed on the sample to a spot size of approximately 30 μm , using a lens L. The sample is placed inside a vacuum chamber with windows at both sides to allow the transmission of the laser beam. The chamber is mounted on a translation stage that allows for a manual adjustment of the position of the sample relative to the laser beam. A feed-through wiring allows the electrical connection of the sample to the outside world. In addition, a rotary-vane vacuum pump is connected to the chamber for an evacuation of the chamber. A camera allows an imaging of the sample and

¹Inspire, Spectra-Physics

6. METAMATERIAL METAL BOLOMETER

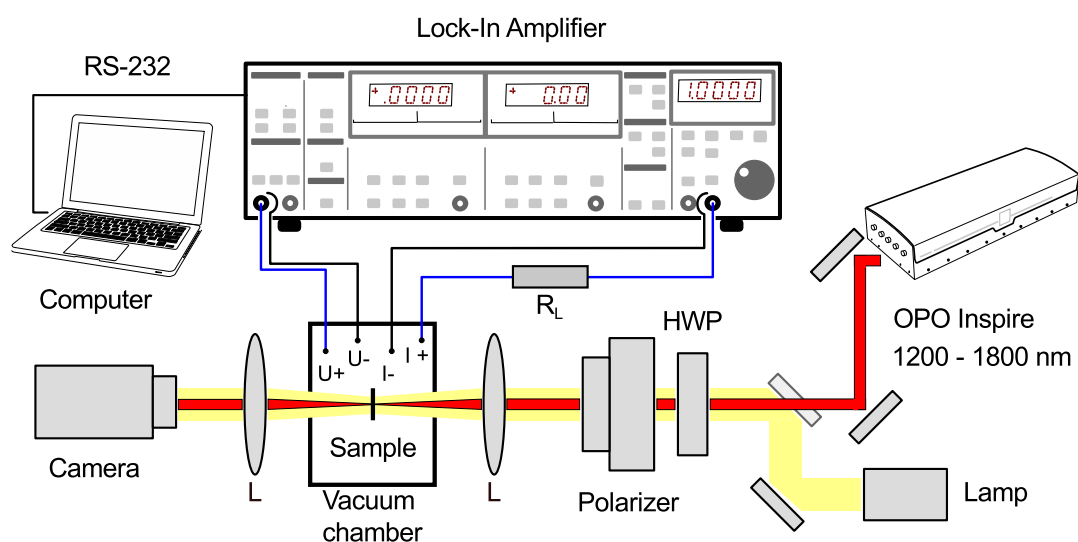


Figure 6.2: Sketch of the experimental setup -

provides an easy way to control the position of the sample relative to the laser beam.

The electrical measurement of the bolometer and the logging of the corresponding data is implemented using a lock-in amplifier ¹. We used the amplifier's own built-in oscillator to feed a current through the bolometer. A load resistor R_L , much larger than the bolometer's resistance, was used to provide an AC current source for the four-terminal sensing of the bolometer's resistance. By using an AC current, we circumvent effects of electromigration. The very thin bolometer wires are expected to be very sensitive to effects of electromigration associated with a DC current [96, 97]. The voltage drop over the bolometer is then measured using the amplifier input. In combination with a computer that is connected via RS-232 and is running Matlab ², an easy and automated measurement routine for the characterization of the bolometer could be implemented.

Resistance Measurement

Measuring the resistance of a simple resistor is normally done using a multimeter with two leads. The multimeter forces a test current through the leads and the

¹SR 830, Stanford Research Systems

²Matlab, The MathWorks, Inc.

resistor and then reads the voltage drop across the wires and calculates the resistance according to Ohm's law. The measured resistance is therefore the sum of the lead resistance, the resistance of the resistor itself, and the contact resistance of the leads. For larger resistors, the result is dominated by the resistance of the resistor. But if the resistance to be measured is low (in the range of 100Ω or lower [98]), there is a problem due to inaccurate readings because the resistance of the leads can not be neglected anymore. The drawbacks of this so called two-wire method can be overcome with the four-wire or four-terminal sensing method. Here, two wires are used to feed the test current through the resistor under test. A second pair of leads, the sense leads, is used to measure the voltage drop across the device under test. This method is also suitable for measuring sheet resistance of very thin films. In our experiments, the resistance of the bolometer structure is measured using a pad geometry that is suitable for measurements with the four-wire method.

Four-Terminal Sensing Setup

To see why the four-wire setup drops the resistance of leads and contacts, the geometry of the contact pads and the equivalent circuit are presented. The bolometer resistance R_B is connected in series with the lead and contact resistances, that are represented by R_{L1} and R_{L2} . The lead and contact resistance and internal resistance R_U of the voltage measuring instrument are connected parallel to the resistance of the bolometer. According to Kirchhoff's laws we can write for the current at the green connection

$$U_B = I_B \cdot R_B = (I - I_U) \cdot R_B \quad (6.25)$$

and the voltages in the loop

$$U_B = U + U_{U1} + U_{U2} = I_U \cdot (R_{U1} + R_{U2} + R_U) \quad (6.26)$$

. Setting both equations equal yields

$$(I - I_U) \cdot R_{\text{Probe}} = I_U \cdot (R_{U1} + R_{U2} + R_U) \quad (6.27)$$

$$I_U = \frac{I \cdot R_B}{R_{U1} + R_{U2} + R_U + R_B} \quad (6.28)$$

The measured voltage is

$$U = I_U \cdot R_U \quad (6.29)$$

6. METAMATERIAL METAL BOLOMETER

and therefor

$$U = \frac{I \cdot R_B \cdot R_U}{R_{U1} + R_{U2} + R_U + R_B}. \quad (6.30)$$

To see that this is equal to $U = I \cdot R_B$ we write

$$U = I \cdot R_B \cdot (1 - \alpha) \quad (6.31)$$

and find

$$\alpha = 1 - \frac{R_U}{R_{U1} + R_{U2} + R_U + R_B} \quad (6.32)$$

$$= \frac{R_{U1} + R_{U2} + R_B}{R_{U1} + R_{U2} + R_U + R_B}. \quad (6.33)$$

For a sufficient high innenwiderstand R_U we find that $\alpha \ll 1$ and therefore

$$U = I \cdot R_B \quad (6.34)$$

$$R_B = \frac{U}{I} \quad (6.35)$$

is valid.

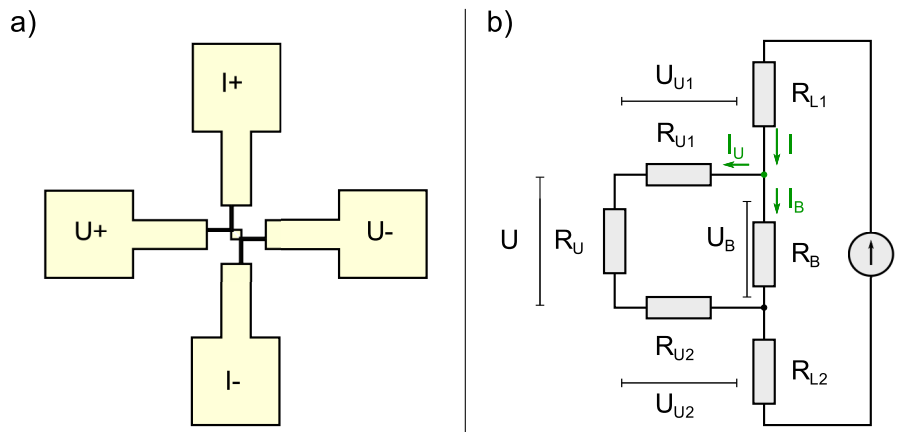


Figure 6.3: Four-terminal sensing - In a): sketch of the pad geometry used to contact the bolometer structure; b) equivalent circuit of the geometry

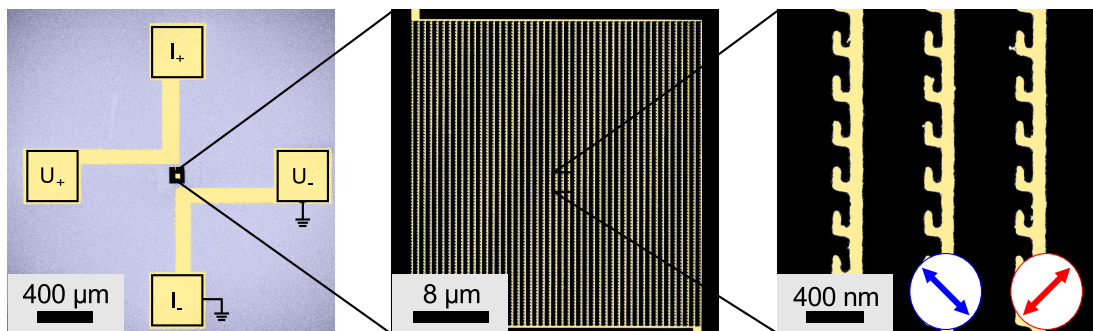


Figure 6.4: Metamaterial metal-based bolometer - Scanning electron micrographs of one of the fabricated devices in different magnifications as indicated by the black scale bars. The active area including the connected resonant polarization-sensitive gold absorber elements is located on a 30 nm thin SiN membrane (black). The arrows on the right-hand side indicate the orientation of the linear eigen-polarizations used in the optical experiments in figure 6.5. (figure and caption from [99])

6.4 Experimental Results

In figure 6.4 the corresponding bolometer design is shown. The scanning electron micrographs show the 40nm thin gold nanostructures that are placed on a 30nm thin, commercial available silicon-nitride (SiN) membrane¹. Fabrication of the structure was done using the electron-beam lithography process with a two-resist system. This measure enhances the undercutting effect on the thin membrane and improves the lift-off process. The membrane has a footprint of $100\ \mu\text{m} \times 100\ \mu\text{m}$ and serves for mechanical support. It also provides a good thermal isolation of the bolometer structure as it strongly reduces the conduction of heat. Thin films of silicon-nitride or silicon-dioxide are often used in the context of microbolometers, thermal detectors or microcalorimeters, as these materials provide good thermal insulation and good mechanical stability [64, 100, 101, 102, 103, 104]. The sensor part, consisting of a grid array of modified split-ring resonators, is placed in the middle of the membrane and has a footprint of $35\ \mu\text{m}$. This array is then electrically connected to four large bond pads in the outer region of the substrate which is supported by the underlying silicon substrate. The substrate is finally glued in on an IC-carrier and processed as already described in the materials and methods section in chapter 3.

¹Silson Ltd. UK

6. METAMATERIAL METAL BOLOMETER

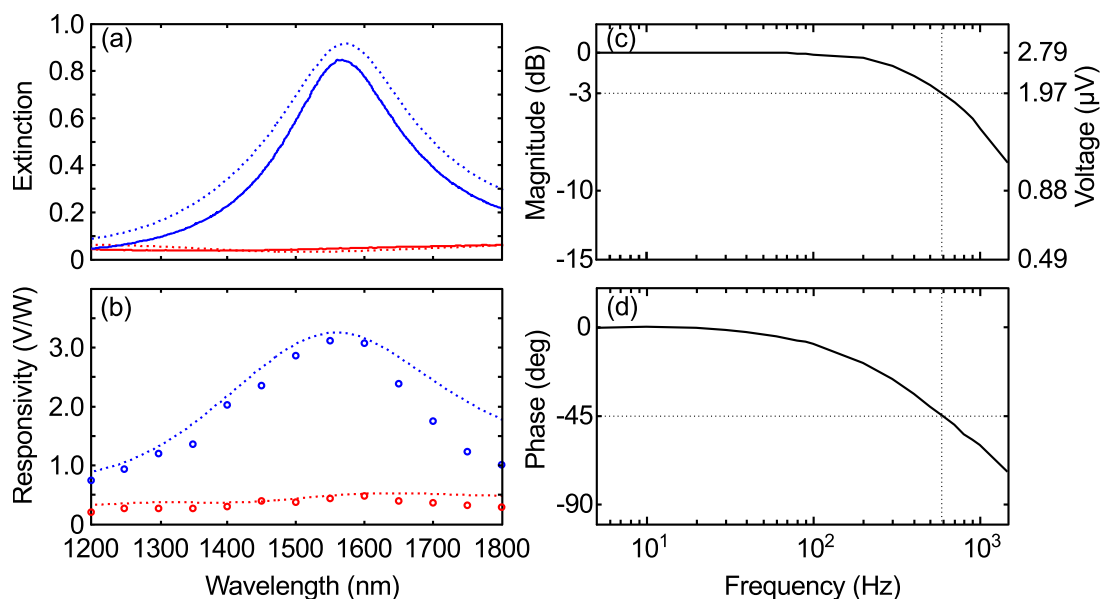


Figure 6.5: Optical and electrical characterization of the metamaterial bolometer - (a), Measured (solid curves) and calculated (dashed curves) extinction spectra for the two linear polarizations indicated by the blue and red arrows in figure 6.4. (b), Measured (dots) and calculated (dashed) bolometer responsivity for an rms current of 50 μA . The calculated responsivity is obtained from the calculated absorbance spectra and the measured thermal conductance G . (c), The thermal conductance and the bolometer time constant are obtained from the depicted measured voltage at the third harmonic of the modulation frequency measured versus modulation frequency. The bolometer time constant of $134 \mu\text{s} = 1/(2 \cdot 2\pi \cdot 596 \text{ Hz})$ results from the -3 dB decay (see left vertical logarithmic scale and dashed lines). (d), Corresponding measured phase.(figure and caption from [99])

The first step towards the full characterization of the bolometer is the measurement of the extinction which is the negative decadic logarithm of the intensity transmittance spectra. Using the standard Fourier-transform spectrometer, the spectra are obtained for light impinging from the SiN membrane side normal to the membrane. Interestingly, the measurements have revealed two linear eigen-polarizations that are diagonally oriented with respect to the SRR arms. In figure 6.5 (a) the measured spectra for the two eigen-polarizations is plotted. The color coding of the curves corresponds to the arrows in figure 6.4.

These measurements are the basis for the further optical characterization. The extinction spectra clearly show a spectral and polarization dependent resonance. To reveal the connected absorption, a direct measurement of the spectral and polarization dependent responsivity of the bolometer is needed. The sample is therefor placed inside the vacuum chamber of the setup providing pre-vacuum conditions with a pressure of about 1 mbar. This prevents the heat transport via air and enhanced the responsivity of the bolometer.

In figure 6.5 (b), the measured responsivity (dots) versus wavelength, for a bias current of $I = 50 \mu\text{A}$ that oscillates at 1 kHz, is presented. The laser power of the OPA, impinging on the sample, is adjusted to $50 \mu\text{W}$ for all wavelengths and polarization directions. One can clearly see the pronounced resonance for one linear polarization (blue dots), whereas there is very little signal found for the orthogonal linear polarization (red dots). These results show that the bolometer signal is governed by light absorption in the metal nanostructure and a subsequent heating of the metal. The corresponding bolometer voltage change is induced by the resistance change of the metal.

To fully characterize the bolometer according to the responsivity 6.13, the TCR α_0 , the effective thermal conductance G_{eff} and the detector's time constant need to be determined. The measurement of the TCR was done by heating the bolometer using a hot plate and simultaneously measure the temperature of the plate and the resistance of the bolometer 6.6. From this fit we deduce a TCR of $\alpha_0 = 0.0024 \text{ 1/K}$. This value matches the values reported in literature for thin gold films of similar thickness [105].

By measuring the third harmonic component $U_{b,3\omega}$ 6.24 of the bolometer voltage versus the modulation frequency, the effective thermal conductance $G_{\text{eff}} = 4.85 \cdot 10^{-6} \text{ W/K}$ can be deduced. For the determination of the time constant we

6. METAMATERIAL METAL BOLOMETER

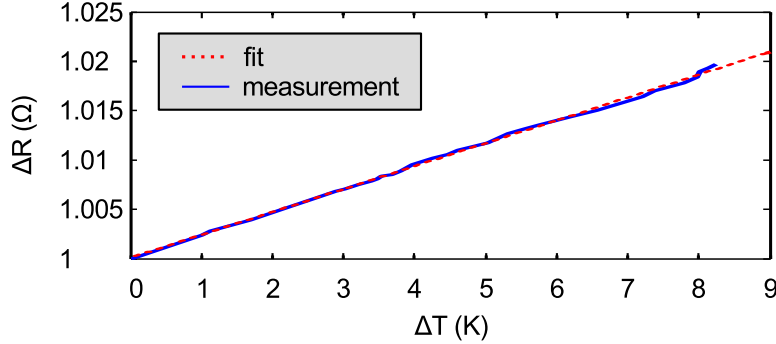


Figure 6.6: Measurement of the TCR - Plot of the measured resistance change $\Delta R = R - R_0$ versus temperature change $\Delta T = T - T_0$ of the bolometer. The fit to the measured data reveals the TCR $\alpha_0 = 0.0024$ 1/K.

used the analogy of an thermal low pass filter. From equation 6.24 we can see, that the third harmonic voltage resembles the voltage of an RC-circuit that acts as an low-pass filter

$$U_{b,3\omega}(\omega) = U_{b,3\omega} \cdot \frac{1}{\sqrt{1 + \omega^2 \tau^2 / 4}} \quad (6.36)$$

where $U_{b,3\omega} = I^3 R_{b0}^2 \alpha_0 / (4G_{\text{eff}})$. When plotting the gain in dB as

$$\text{Gain} = 20 \cdot \log \left(\frac{U_{b,3\omega}(\omega)}{U_{b,3\omega}} \right) \quad (6.37)$$

we can get the time constant from the -3dB point within the bode plot. This cutoff frequency corresponds to $f_c = 1/(2\pi 2\tau)$. The bolometer time constant is determined as 134 μs . We have also plotted the phase of the voltage signal. The phase shift of -45 degrees corresponds very well to the cut-off frequency, in accordance with the theory of a low-pass filter. These results are shown in figure 6.5(c),(d).

The bolometer performance is not only characterized by its responsivity but also by the noise of the bolometer and its read-out electronics. Our experimental setup was not optimized for a low noise measurement and an experimental characterization of the noise characteristics was not done. In the context of thin-metal-film bolometer it is known that ultimate performance is limited by the Johnson-noise of the metals resistance [77]. When we assume a Johnson-noise-limited performance, the resistance of our bolometer of $R = 300 \Omega$ under room-

temperature operation results in a noise-equivalent power of $6.7 \cdot 10^{-10} \text{W}/\sqrt{\text{Hz}}$ allowing the detection of faint signals in the range of nW.

The measured data is the basis for our further theoretical studies. Using the software package CST Microwave Studio, numerical calculations were conducted to evaluate the spectral tuning capabilities of the metamaterial bolometer concept. For the simulations of the metal behavior the free-electron Drude model with a plasma frequency $\omega_{pl} = 1.37 \cdot 10^{16} \text{ rad/s}$ was used. The damping was accounted using a collision frequency of $\omega_{col} = 2.2 \cdot 10^{14} \text{ rad/s}$. From the electron micrographs in figure 6.4, the geometrical parameters could be extracted. The gold thickness for the simulations was chosen as 40 nm in accordance with the experiment. The refractive index of the 30 nm thin SiN membrane was set to $n = 1.96$. In figure 6.5 (a), the calculated extinction spectra are shown as dashed curves. From these data, we calculate the spectral absorbance $\epsilon = 1 - T - R$ using the corresponding transmission T and reflection spectra R from Microwave Studio. This finally allows the calculation of the spectral responsivity of the bolometer using equation 6.13 together with the previously experimentally determined values. In figure 6.5 (b) the results are plotted as dashed lines. Obviously, the spectral resonant behavior as well as the polarization dependence are qualitatively well reproduced.

The good qualitative agreement is the starting point for the evaluation of the tunability of the resonant bolometer response. A broad spectral tuning range is key for the implementation of broadband spectrometers. For the theoretical investigation, we scale the lateral features of the structure while keeping the metal thickness constant. This measure fixes the bolometers thermal mass per unit area. In figure 6.7 the corresponding calculations of the absorbance ϵ are presented where the linear polarization is oriented relative to the structure as indicated by the blue arrow in figure 6.4. The right configuration corresponds to the feature size that was used to calculate the responsivity of our experimentally fabricated bolometer. Starting from this configuration we increased the lateral features in steps of factors of two. As can be seen, a tuning between roughly 1 μm up to 10 μm wavelength is possible.

6. METAMATERIAL METAL BOLOMETER

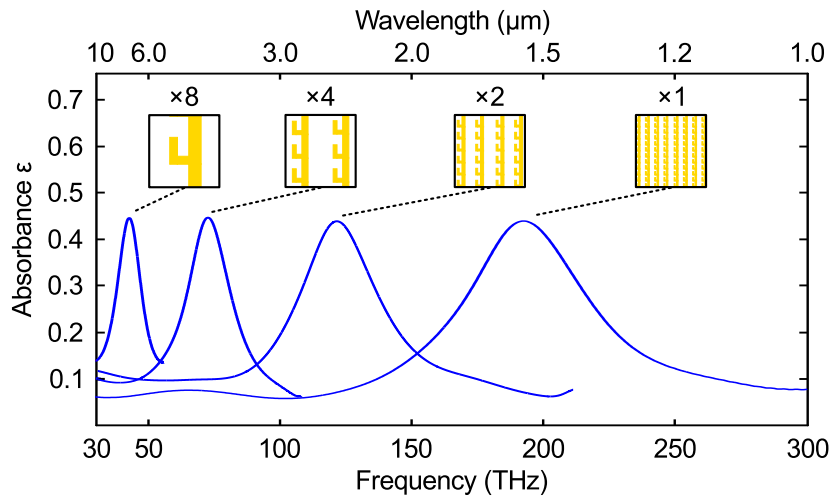


Figure 6.7: Calculations on bolometer tunability - For reference, the highest frequency resonance corresponds to the parameters of figure 6.5. For the other three structures, all lateral dimensions are increased in steps of factors of two (see insets), while fixing the metal thickness, hence fixing the bolometer thermal mass. Importantly, the fundamental absorber resonances can be shifted towards significantly longer wavelengths, while maintaining the peak absorbance. (figure and caption from [99])

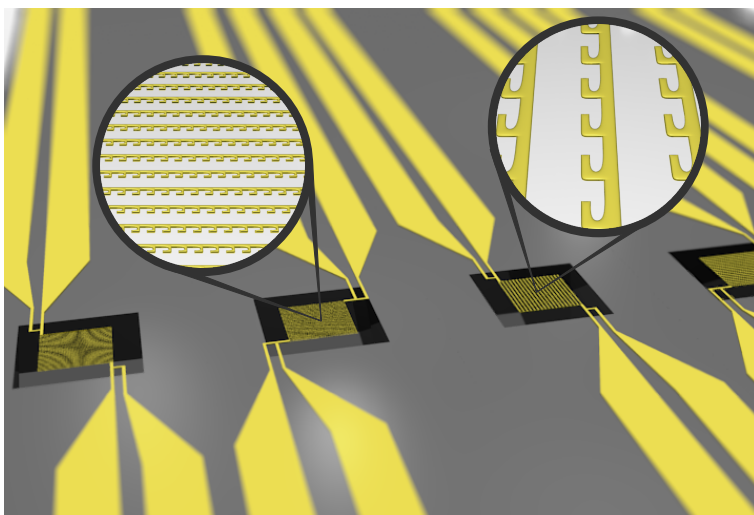


Figure 6.8: Envisioned bolometer array architecture - This concept allows for integrated broadband spectroscopy and polarimetry without the need for any external dispersive element or any polarizer. (figure and caption from [99])

6.4.1 Conclusions

The proof-of-concept of a metamaterial metal-based bolometer takes advantage of the resonant absorption accompanied by the excitation of plasmonic resonances within gold nanostructures. That way, a spectral and/or polarization filter can be built into the bolometer without the need of external dispersive elements. On this basis, an integrated broadband metamaterial metal-based bolometer spectrometer array can be envisioned, as illustrated in figure 6.8. The presence of the rotated elements would simultaneously allow for analyzing the polarization state of light.

6. METAMATERIAL METAL BOLOMETER

7

Conclusions and Outlook

The first part of the experimental work presented in this thesis focussed on the second-harmonic generation from gold split-ring resonator arrays. Earlier work on this topic has revealed a strong nonlinear optical response from this metamaterial building block [45, 46, 47]. With these results as a starting point, we explored the idea of Pendry [3], who pointed out the possible extraordinary nonlinear optical response of a SRR having a nonlinear optical material placed into the gap region of the SRR. The concentration of the electric field within the gap region might lead to an enhanced nonlinear response. We slightly modified this idea, and placed the gold SRR on a substrate possessing itself a strong nonlinear optical response of second order, namely gallium arsenide (GaAs). The orientation of the SRR relative to the GaAs crystallographic axes and the incident light polarization was varied systematically. As a result, we did find a configuration where the overall signal strength of the SHG was approximately a factor of 25 times larger than those from SRR arrays on glass substrates, when referenced to the same incident laser intensity. In addition, an analyzation of the polarization of the emitted SHG light revealed a nonlinear contribution that originates specifically from the interplay of the local fields of the split-ring resonators with the bulk GaAs second-order nonlinear-susceptibility tensor. These results were also in good agreement with a theoretical modeling of this system. A simple near-field simulation of the resonantly excited SRR was used as the source for a calculation of the nonlinear polarization of second order within the GaAs crystal. Through a spatial averaging of this polarization over the whole unit cell, we were able to identify the main component of the nonlinear polarization contributing to the

7. CONCLUSIONS AND OUTLOOK

measured SHG signal.

For the next experiment, a new setup suitable for nonlinear optical spectroscopy was built. The setup used an optical parametric oscillator as a tunable light source and consisted of a sample and a reference arm. While previous second-harmonic-generation experiments on gold split-ring-resonator arrays were all limited to a fixed excitation wavelength [45, 46, 47], using this new setup, a full second-harmonic spectroscopy study on SRR arrays could be conducted. For the set of samples, the technique of a lithographic tuning of the spectral resonance position of the SRR arrays was employed. This technique was already introduced by Klein et al. [45] to overcome the limitation of the fixed excitation wavelength used in their experiment. Here, this tuning was used to study the role of the relative spectral positions of the fundamental magnetic resonance and the higher order resonances of gold SRR arrays on glass substrates on the process of second-harmonic generation. The measured nonlinear spectroscopic data on a first set of samples, where the size of the SRR was scaled, revealed pronounced resonances. The SHG maximum shifts when the resonance positions of the SRR is changed through the lithographic tuning. To clarify the role of the higher-order resonances on the SHG signal, a second set of samples was produced. Here, the shape of the SRR was varied in such a way, that the higher-order resonances of the SRR stay spectrally fixed and only the fundamental magnetic resonance position of the SRR is shifted. The corresponding second-harmonic generation spectra again reveals resonances. However, the SHG maximum correlates with the position of the fundamental SRR resonance and not with the position of the higher-order resonances. This is interpreted as an indication for the fundamental SRR resonance to act as the nonlinear source while higher-order SRR resonances merely reabsorb the generated vertically polarized SHG. The measured spectroscopic data helped in clarifying the role of the higher-order resonances and also provide a sensitive future testing ground for microscopic theories of the underlying physical mechanisms.

In the third experiment on second-harmonic generation from SRR arrays, we have studied the dependence of the conversion efficiency on the lattice constant. The experiment was motivated by the search for the most efficient configuration for frequency conversion with regard to the spacing between individual SRR within the array. Intuitively, one might think that the best conversion efficiency

is achieved by packing the individual building blocks as dense as possible as this maximizes the number of nonlinear emitters per unit area. To test this intuitive reasoning, a set of samples was fabricated, where the spectral position of the resonances of each SRR array was kept constant but the distance between the SRR within each array was systematically modified to change the packing density. This sample was then characterized using the same second-harmonic spectroscopy setup as in the earlier experiment. The experimental result revealed a non-monotonic behavior of the resonant second-order nonlinear conversion efficiency versus the packing density, rendering the intuitive approach for efficient frequency conversion invalid. The maximum conversion efficiency was found for an intermediate lattice constant. A closer inspection of the experimental data revealed two counteracting effects influencing the overall SHG conversion efficiency. By bringing the SRRs closer to each other, the SHG intensity rises because of more nonlinear emitters per unit area. On the other hand, bringing the SRRs closer also increases the damping of the linear fundamental resonance as can be seen from the change in linewidth of the corresponding measured linear extinction spectra. The linewidth enters sensitively into the second-order nonlinear-optical susceptibility $\chi^{(2)}$, a larger damping leads to a smaller resonant $\chi^{(2)}$, thus reducing the conversion efficiency when the SRR are brought closer to each other. Both effects level out at some intermediate lattice constant to provide the maximum SHG conversion efficiency. Numerical calculations using the discontinuous Galerkin time-domain method could reproduce the experimental findings well and allowed to support the qualitative reasoning. These calculations allowed also for an inspection of the SRR electric near-field at the fundamental excitation wavelength. We found that an increase of the lattice constant leads to an increase of the strength of the near and internal fields of the SRR. This leads to a stronger nonlinear response of the SRR and can explain the initial increase of SHG intensity with increasing lattice constant. Then, for yet larger lattice constants, this increase is compensated and dominated by the dilution effect, leading to the observed decrease in SHG signal intensity.

The final experiment aimed on providing a possible application of metamaterials. For many metamaterial applications, the loss that is inherently connected to its plasmonic resonances is an often unwanted by-product. The new concept of a metamaterial-metal based bolometer uses these losses to its advantage. While

7. CONCLUSIONS AND OUTLOOK

the principle of a metal bolometer is known for more than one century, with the new concept, an old idea is enhanced by a new technology. A modified gold split-ring resonator structure was used to not only provide a lithographically tunable resonant absorption over a broad spectral range, but also to measure the temperature increase due to the absorption of light. Furthermore, the structure is also polarization sensitive, allowing for an integrated polarization analysis without the need of external polarizers. The device was fabricated and fully characterized, optically as well as electrically to proof the spectral and polarization dependent responsivity.

In summary, the experimental results of this thesis provide a deeper insight into the mechanisms of nonlinear optics of metamaterials and can be a guide for future nonlinear optical experiments aiming at achieving large effective optical nonlinearities using metamaterials. In addition, a possible application for the absorption within metamaterials was demonstrated with the metamaterial bolometer. Integration of suitable read-out electronics on a chip in combination with the metamaterial bolometer could be the next step towards implementation of a microbolometer arrays using metamaterial absorbers.

References

- [1] V. Veselago, “The electrodynamics of substances with simultaneously negative values of ϵ and μ ,” *Soviet Physics Uspekhi*, vol. 10, no. 4, p. 509, 1968.
- [2] J. Pendry, “Negative refraction makes a perfect lens,” *Physical Review Letters*, vol. 85, no. 18, p. 3966, 2000.
- [3] J. Pendry, A. Holden, D. Robbins, and W. Stewart, “Magnetism from conductors and enhanced nonlinear phenomena,” *IEEE Transactions On Microwave Theory and Techniques*, vol. 47, no. 11, p. 2075, 1999.
- [4] R. Shelby, D. Smith, and S. Schultz, “Experimental verification of a negative index of refraction,” *Science*, vol. 292, no. 5514, p. 77, 2001.
- [5] S. Linden, C. Enkrich, M. Wegener, J. Zhou, T. Koschny, and C. M. Soukoulis, “Magnetic response of metamaterials at 100 terahertz,” *Science*, vol. 306, no. 5700, p. 1351, 2004.
- [6] C. Enkrich, M. Wegener, S. Linden, S. Burger, L. Zschiedrich, F. Schmidt, J. Zhou, T. Koschny, and C. Soukoulis, “Magnetic metamaterials at telecommunication and visible frequencies,” *Physical Review Letters*, vol. 95, no. 20, p. 203901, 2005.
- [7] V. M. Shalaev, “Transforming light,” *Science*, vol. 322, no. 5900, p. 384, 2008.
- [8] J. Pendry, D. Schurig, and D. Smith, “Controlling electromagnetic fields,” *Science*, vol. 312, no. 5781, p. 1780, 2006.

REFERENCES

- [9] U. Leonhardt, “Optical conformal mapping,” *Science*, vol. 312, no. 5781, p. 1777, 2006.
- [10] T. Ergin, N. Stenger, P. Brenner, J. B. Pendry, and M. Wegener, “Three-dimensional invisibility cloak at optical wavelengths,” *Science*, vol. 328, no. 5976, pp. 337–339, 2010.
- [11] C. Soukoulis and M. Wegener, “Past achievements and future challenges in the development of three-dimensional photonic metamaterials,” *Nature Photonics*, vol. 5, no. 9, p. 523, 2011.
- [12] N. Landy, S. Sajuyigbe, J. Mock, D. Smith, and W. Padilla, “Perfect metamaterial absorber,” *Physical Review Letters*, vol. 100, no. 20, p. 207402, 2008.
- [13] N. Liu, M. Mesch, T. Weiss, M. Hentschel, and H. Giessen, “Infrared perfect absorber and its application as plasmonic sensor,” *Nano Letters*, vol. 10, no. 7, p. 2342, 2010.
- [14] A. Tittl, P. Mai, R. Taubert, D. Dregely, N. Liu, and H. Giessen, “Palladium-based plasmonic perfect absorber in the visible wavelength range and its application to hydrogen sensing,” *Nano Letters*, vol. 11, no. 10, p. 4366, 2011.
- [15] X. Liu, T. Tyler, T. Starr, A. Starr, N. Jokerst, and W. Padilla, “Taming the blackbody with infrared metamaterials as selective thermal emitters,” *Physical Review Letters*, vol. 107, no. 4, p. 045901, 2011.
- [16] M. Diem, T. Koschny, and C. Soukoulis, “Wide-angle perfect absorber/thermal emitter in the terahertz regime,” *Physical Review B*, vol. 79, no. 3, p. 033101, 2009.
- [17] S. Maier, *Plasmonics: Fundamentals and Applications*. Springer Berlin Heidelberg, 2007.
- [18] K.-S. Lee and M. El-Sayed, “Gold and silver nanoparticles in sensing and imaging: sensitivity of plasmon response to size, shape, and metal composition,” *The Journal of Physical Chemistry B*, vol. 110, no. 39, p. 19220, 2006. PMID: 17004772.

REFERENCES

- [19] C. Bohren and D. Huffman, *Absorption and scattering of light by small particles*. Wiley Online Library, 1983.
- [20] G. Mie, “Beiträge zur optik trüber medien, speziell kolloidaler metallösungen,” *Annalen der Physik*, vol. 330, no. 3, p. 377, 1908.
- [21] P. Franken, A. Hill, C. Peters, and G. Weinreich, “Generation of optical harmonics,” *Physical Review Letters*, vol. 7, no. 4, p. 118, 1961.
- [22] R. Boyd, *Nonlinear optics*. Academic Press, 2003.
- [23] E. Hartmann, *An Introduction to Crystal Physics*. Cardiff, Wales: University College Cardiff Press, 2001.
- [24] F. Brown, R. Parks, and A. Sleeper, “Nonlinear optical reflection from a metallic boundary,” *Physical Review Letters*, vol. 14, p. 1029, 1965.
- [25] S. Jha, “Theory of optical harmonic generation at a metal surface,” *Physical Review*, vol. 140, no. 6A, p. A2020, 1965.
- [26] S. Jha, “Nonlinear optical reflection from a metal surface,” *Physical Review Letters*, vol. 15, no. 9, p. 412, 1965.
- [27] N. Akhmediev, I. Melnikov, and L. Robur, “Second-harmonic generation by a reflecting metal surface,” *Laser Physics*, vol. 4, no. 6, p. 1194, 1994.
- [28] D. Maystre, M. Neviere, and R. Reinisch, “Nonlinear polarisation inside metals: A mathematical study of the free-electron model,” *Applied Physics A: Materials Science & Processing*, vol. 39, p. 115, 1986. 10.1007/BF00616828.
- [29] J. Rudnick and E. Stern, “Second-harmonic radiation from metal surfaces,” *Physical Review B*, vol. 4, p. 4274, 1971.
- [30] C. Wang, J. Chen, and J. Bower, “Second harmonic generation from alkali metals,” *Optics Communications*, vol. 8, no. 4, p. 275, 1973.
- [31] J. Sipe, V. So, M. Fukui, and G. Stegeman, “Second harmonic generation at metal surfaces,” *Solid State Communications*, vol. 34, no. 7, p. 523, 1980.

REFERENCES

- [32] M. Corvi and W. Schaich, “Hydrodynamic-model calculation of second-harmonic generation at a metal surface,” *Physical Review B*, vol. 33, no. 6, p. 3688, 1986.
- [33] Y. Zeng, W. Hoyer, J. Liu, S. Koch, and J. Moloney, “Classical theory for second-harmonic generation from metallic nanoparticles,” *Physical Review B*, vol. 79, no. 23, p. 235109, 2009.
- [34] J. Liu, M. Brio, Y. Zeng, A. Zakharian, W. Hoyer, S. Koch, and J. Moloney, “Generalization of the fdtd algorithm for simulations of hydrodynamic non-linear drude model,” *Journal of Computational Physics*, vol. 229, no. 17, p. 5921, 2010.
- [35] C. Ciraci, E. Poutrina, M. Scalora, and D. Smith, “Origin of second-harmonic generation enhancement in optical split-ring resonators,” *Physical Review B*, vol. 85, p. 201403, 2012.
- [36] D. Smith, W. Padilla, D. Vier, S. Nemat-Nasser, and S. Schultz, “Composite medium with simultaneously negative permeability and permittivity,” *Physical Review Letters*, vol. 84, no. 18, p. 4184, 2000.
- [37] K. Busch, G. von Freymann, S. Linden, S. Mingaleev, L. Tkeshelashvili, and M. Wegener, “Periodic nanostructures for photonics,” *Physics Reports-Review Section of Physics Letters*, vol. 444, no. 3-6, p. 101, 2007.
- [38] C. M. Soukoulis, “Negative refractive index at optical wavelengths (vol 315, pg 47, 2007),” *Science*, vol. 315, pp. 1077–1077, Feb. 2007.
- [39] C. Enkrich, R. Perez-Willard, D. Gerthsen, J. Zhou, T. Koschny, C. Soukoulis, M. Wegener, and S. Linden, “Focused-ion-beam nanofabrication of near-infrared magnetic metamaterials,” *Advanced Materials*, vol. 17, no. 21, p. 2547, 2005.
- [40] K. Fan, A. Strikwerda, H. Tao, X. Zhang, and R. Averitt, “Stand-up magnetic metamaterials at terahertz frequencies,” *Optics Express*, vol. 19, no. 13, p. 12619, 2011.

REFERENCES

- [41] G. Dolling, C. Enkrich, M. Wegener, J. Zhou, and C. Soukoulis, “Cut-wire pairs and plate pairs as magnetic atoms for optical metamaterials,” *Optics Letters*, vol. 30, no. 23, p. 3198, 2005.
- [42] P. Mühlischlegel, H. Eisler, O. Martin, B. Hecht, and D. Pohl, “Resonant optical antennas,” *Science*, vol. 308, no. 5728, p. 1607, 2005.
- [43] K. Crozier, A. Sundaramurthy, G. Kino, and C. Quate, “Optical antennas: Resonators for local field enhancement,” *Journal of Applied Physics*, vol. 94, no. 7, p. 4632, 2003.
- [44] N.-A. Feth, *Nonlinear Optics of Planar Metamaterial Arrays and Spectroscopy of Individual Photonic Atoms*. PhD thesis, Karlsruher Institut für Technologie, 2010.
- [45] M. Klein, C. Enkrich, M. Wegener, and S. Linden, “Second-harmonic generation from magnetic metamaterials,” *Science*, vol. 313, no. 5786, p. 502, 2006.
- [46] M. Klein, M. Wegener, N. Feth, and S. Linden, “Experiments on second- and third-harmonic generation from magnetic metamaterials,” *Optics Express*, vol. 15, no. 8, p. 5238, 2007.
- [47] N. Feth, S. Linden, M. Klein, M. Decker, F. Niesler, Y. Zeng, W. Hoyer, J. Liu, S. Koch, J. Moloney, and M. Wegener, “Second-harmonic generation from complementary split-ring resonators,” *Optics Letters*, vol. 33, no. 17, p. 1975, 2008.
- [48] S. Kujala, B. Canfield, M. Kauranen, Y. Svirko, and J. Turunen, “Multipole interference in the second-harmonic optical radiation from gold nanoparticles,” *Physical Review Letters*, vol. 98, p. 167403, Apr 2007.
- [49] B. Canfield, H. Husu, J. Laukkanen, B. Bai, M. Kuittinen, J. Turunen, and M. Kauranen, “Local field asymmetry drives second-harmonic generation in noncentrosymmetric nanodimers,” *Nano Letters*, vol. 7, no. 5, p. 1251, 2007.

REFERENCES

- [50] W. Fan, S. Zhang, K. Malloy, S. Brueck, N. Panoiu, and R. Osgood, “Second harmonic generation from patterned gaas inside a subwavelength metallic hole array,” *Optics Express*, vol. 14, no. 21, p. 9570, 2006.
- [51] S. Kim, J. Jin, Y. Kim, I. Park, Y. Kim, and S. Kim, “High-harmonic generation by resonant plasmon field enhancement,” *Nature*, vol. 453, no. 7196, p. 757, 2008.
- [52] F. Niesler, N. Feth, S. Linden, J. Niegemann, J. Gieseler, K. Busch, and M. Wegener, “Second-harmonic generation from split-ring resonators on a gaas substrate,” *Optics Letters*, vol. 34, no. 13, p. 1997, 2009.
- [53] H. Day, A. Christou, and A. Macpherson, “Interdiffusion and schottkybarrierheight variations in au-w(ti)/ngaas contacts,” *Journal of Vacuum Science & Technology*, vol. 14, no. 4, p. 939, 1977.
- [54] W. Stremow and E. Cook, “Compilation of energy band gaps in elemental and binary compound semiconductors and insulators,” *Journal of Physical and Chemical Reference Data*, vol. 2, no. 163, 1973.
- [55] F. Niesler, N. Feth, S. Linden, and M. W., “Second-harmonic optical spectroscopy on split-ring-resonator arrays,” *Optics Letters*, vol. 36, no. 9, p. 1533, 2011.
- [56] S. Linden, F. Niesler, J. Förstner, Y. Grynko, T. Meier, and M. Wegener, “Collective effects in second-harmonic generation from split-ring-resonator arrays,” *Physical Review Letters*, vol. 109, p. 015502, 2012.
- [57] M. Decker, N. Feth, C. Soukoulis, S. Linden, and M. Wegener, “Retarded long-range interaction in split-ring-resonator square arrays,” *Physical Review B*, vol. 84, no. 8, p. 085416, 2011.
- [58] R. Wood, “On a remarkable case of uneven distribution of light in a diffraction grating spectrum,” *Proceedings of the Physical Society of London*, vol. 18, no. 1, p. 269, 1902.
- [59] I. Sersic, M. Frimmer, E. Verhagen, and A. Koenderink, “Electric and magnetic dipole coupling in near-infrared split-ring metamaterial arrays,” *Physical Review Letters*, vol. 103, no. 21, p. 213902, 2009.

-
- [60] J. Hesthaven and T. Warburton, *Nodal Discontinuous Galerkin Methods: Analysis, Algorithms, and Applications*. Springer-Verlag, Berlin, 2008.
- [61] K. Stannigel, M. König, J. Niegemann, and K. Busch, “Discontinuous galerkin time-domain computations of metallic nanostructures,” *Optics Express*, vol. 17, no. 17, p. 14934, 2009.
- [62] A. Akhiezer, I. Akhiezer, R. Polovin, A. Sitenko, and K. Stepanov, *Plasma electrodynamics. Volume I. Linear theory*. Pergamon Press, New York, 1975.
- [63] Hamamatsu, *Characteristics and use of infrared detectors*.
- [64] F. Vöelklein, *Thermal-Based Microsensors*. Springer Berlin Heidelberg, 2006.
- [65] P. Richards, “Bolometers for infrared and millimeter waves,” *Journal of Applied Physics*, vol. 76, no. 1, p. 1, 1994.
- [66] M. Golay, “A pneumatic infra-red detector,” *Review of Scientific Instruments*, vol. 18, no. 5, p. 357, 1947.
- [67] S. Langley, “The bolometer and radiant energy,” in *Proceedings of the American Academy of Arts and Sciences*, vol. 16, p. 342, JSTOR, 1880.
- [68] E. Archbold, “An evaporated gold bolometer,” *Journal of Scientific Instruments*, vol. 34, no. 6, p. 240, 1957.
- [69] W. Blevin and W. Brown, “Large-area bolometers of evaporated gold,” *Journal of Scientific Instruments*, vol. 42, no. 1, p. 19, 1965.
- [70] C. Aiken, W. Carter, and F. Phillips, “The production of film type bolometers with rapid response,” *Review of Scientific Instruments*, vol. 17, no. 10, p. 377, 1946.
- [71] D. Ball, *Field guide to spectroscopy*. SPIE Press, 2006.
- [72] M. Galeazzi and D. McCammon, “Microcalorimeter and bolometer model,” *Journal of Applied Physics*, vol. 93, no. 8, p. 4856, 2003.

REFERENCES

- [73] J. L. IV and J. L. V, *A Heat Transfer Textbook*, vol. 4. Phlogiston Press, 1961.
- [74] I. T. AG, “Thermal resistance theory and practice,” tech. rep., Infineon technologies, 2000.
- [75] S. Stetson, *Pspice Modelling and Parametric Study of Microbolometer Thermal Detectors*. PhD thesis, US Navy Naval Postgraduate School, 2001.
- [76] Y.-M. Chen, J.-S. Shie, and T. Hwang, “Parameter extraction of resistive thermal sensors,” *Sensors and Actuators A: Physical*, vol. 55, no. 1, p. 43, 1996. International Workshop on Thermal Investigations of ICs and Microstructures (THERMINIC Workshop).
- [77] K. Liddiard, “Thin-film resistance bolometer ir detectors,” *Infrared Physics*, vol. 24, no. 1, p. 57, 1984.
- [78] J. Talghader, “Thermal and mechanical phenomena in micromechanical optics,” *Journal of Physics D: Applied Physics*, vol. 37, no. 10, p. R109, 2004.
- [79] M. Stockman, “Criterion for negative refraction with low optical losses from a fundamental principle of causality,” *Physical Review Letters*, vol. 98, no. 17, p. 177404, 2007.
- [80] P. Kinsler and M. McCall, “Causality-based criteria for a negative refractive index must be used with care,” *Physical Review Letters*, vol. 101, no. 16, p. 167401, 2008.
- [81] N. Meinzer, *Coupling Plasmonic Metamaterials to Single-Quantum-Well Gain*. PhD thesis, Karlsruher Institut für Technologie, 2011.
- [82] Y. Avitzour, Y. Urzhumov, and G. Shvets, “Wide-angle infrared absorber based on a negative-index plasmonic metamaterial,” *Physical Review B*, vol. 79, no. 4, p. 045131, 2009.
- [83] H.-T. Chen, J. Zhou, J. O’Hara, F. Chen, A. Azad, and A. Taylor, “Antireflection coating using metamaterials and identification of its mechanism,” *Physical Review Letters*, vol. 105, no. 7, p. 073901, 2010.

REFERENCES

- [84] M. Knight, H. Sobhani, P. Nordlander, and N. Halas, "Photodetection with active optical antennas," *Science*, vol. 332, no. 6030, p. 702, 2011.
- [85] G. Shvets, S. Trendafilov, J. Pendry, and A. Sarychev, "Guiding, focusing, and sensing on the subwavelength scale using metallic wire arrays," *Physical Review Letters*, vol. 99, no. 5, p. 053903, 2007.
- [86] N. Verellen, Y. Sonnefraud, H. Sobhani, F. Hao, V. Moshchalkov, P. Van Dorpe, P. Nordlander, and S. Maier, "Fano resonances in individual coherent plasmonic nanocavities," *Nano Letters*, vol. 9, no. 4, p. 1663, 2009.
- [87] J.-S. Shie, Y.-M. Chen, M. Ou-Yang, and B. Chou, "Characterization and modeling of metal-film microbolometer," *Microelectromechanical Systems, Journal of*, vol. 5, no. 4, p. 298, 1996.
- [88] E. Monticone, L. Boarino, G. Lerondel, R. Steni, G. Amato, and V. Lacquaniti, "Properties of metal bolometers fabricated on porous silicon," *Applied Surface Science*, vol. 142, no. 1, p. 267, 1999.
- [89] P. Eriksson, J. Andersson, and G. Stemme, "Thermal characterization of surface-micromachined silicon nitride membranes for thermal infrared detectors," *Journal of Microelectromechanical Systems*, vol. 6, no. 1, p. 55, 1997.
- [90] D. Cahill and R. Pohl, "Thermal conductivity of amorphous solids above the plateau," *Physical Review B*, vol. 35, no. 8, p. 4067, 1987.
- [91] Cahill, Katiyar, and Abelson, "Thermal conductivity of α -Si:H thin films," *Physical Review B*, vol. 50, no. 9, p. 6077, 1994.
- [92] C. Dames and G. Chen, " 1ω , 2ω , and 3ω methods for measurements of thermal properties," *Review of Scientific Instruments*, vol. 76, no. 12, p. 124902, 2005.
- [93] T. Borca-Tasciuc, A. Kumar, and G. Chen, "Data reduction in 3ω method for thin-film thermal conductivity determination," *Review of Scientific Instruments*, vol. 72, no. 4, p. 2139, 2001.

REFERENCES

- [94] A. Jain and K. E. Goodson, "Measurement of the thermal conductivity and heat capacity of freestanding shape memory thin films using the 3ω method," *Journal of Heat Transfer-Transactions of the Asme*, vol. 130, no. 10, p. 102402, 2008.
- [95] M. Ou-Yang, C. Sheen, and J. Shie, "Parameter extraction of resistive thermal microsensors by ac electrical method," *IEEE Transactions On Instrumentation and Measurement*, vol. 47, no. 2, p. 403, 1998.
- [96] F. O. Hadeed and C. Durkan, "Controlled fabrication of 1-2 nm nanogaps by electromigration in gold and gold-palladium nanowires," *Applied Physics Letters*, vol. 91, no. 12, p. 123120, 2007.
- [97] B. Stahlmecke, *Elektromigration in Gold und Silber Nanostrukturen*. PhD thesis, Universität Duisburg-Essen, 2008.
- [98] I. Keithley Instruments, *Low Level Measurements Handbook*. Keithley Instruments, Inc., 6th edition ed., 2011.
- [99] F. Niesler, J. Gansel, S. Fischbach, and M. Wegener, "Metamaterial metal-based bolometers," *Applied Physics Letters*, vol. 100, no. 20, p. 203508, 2012.
- [100] F. Gonzalez, B. Ilic, and G. Boreman, "Antenna-coupled microbolometers on a silicon-nitride membrane," *Microwave and Optical Technology Letters*, vol. 47, no. 6, p. 546, 2005.
- [101] B. Zink and F. Hellman, "Specific heat and thermal conductivity of low-stress amorphous si-n membranes," *Solid State Communications*, vol. 129, no. 3, p. 199, 2004.
- [102] B. Revaz, B. Zink, D. O'Neil, L. Hull, and F. Hellman, "Numerical simulation of the heat transfer in amorphous silicon nitride membrane-based microcalorimeters," *Review of Scientific Instruments*, vol. 74, no. 10, p. 4389, 2003.
- [103] M. Ahn, Y.-H. Han, and S. Moon, "A novel infrared absorbing structure for uncooled infrared detector," *Current Applied Physics*, vol. 7, no. 6, p. 617, 2007.

REFERENCES

- [104] M. Burzo, P. Komarov, and P. Raad, "Thermal transport properties of gold-covered thin-film silicon dioxide," *IEEE Transactions On Components and Packaging Technologies*, vol. 26, no. 1, p. 80, 2003.
- [105] M. Adamov, B. Perovic, and T. Nenadovic, "Electrical and structural properties of thin gold films obtained by vacuum evaporation and sputtering," *Thin Solid Films*, vol. 24, no. 1974, p. 89, 1974.

REFERENCES

Acknowledgments

The last words of this thesis are dedicated to thanking all the people who contributed to the success of this work.

First and foremost, I thank my supervisor Prof. Dr. Martin Wegener for providing me an excellent environment for research. I value the opportunity he gave to me to work on an interesting scientific topic in his group. He also allowed space for my own ideas and helped them to grow in a successful direction through his profound knowledge and vast experience. His professionalism is an inspiring example I appreciated during working with him.

I also thank Prof. Dr. Stefan Linden who introduced me into the field of metamaterials. His experimental and theoretical knowledge he shared with me allowed me to handle difficulties in the daily lab work. I enjoyed reflecting new ideas in the numerous fruitful discussions we had.

I thank Prof. Dr. Kurt Busch for not only agreeing to co-referee my thesis but also for the successful collaboration with his group, which lead to an interesting publication in the field of nonlinear optics of metamaterials.

Regarding the collaboration during my thesis, I also thank Prof. Dr. Torsten Meier and his group from Paderborn for their theoretical support on our joint publication.

I also want to thank those numerous helping hands for everyday problems. The electronics workshop with Helmuth Lay and Werner Gilde, and the group technician Johann Westhauser were of great help and their rapid response will stay in my memory. The secretary of the Institute of Applied Physics , Renate Helfen, impressed me with her friendly and straightforward way of solving problems and getting things done.

Special thanks goes to Dr. Nils Feth and Dr. Mathias Ruther for their assistance in all technical concerns of electron-beam lithography, lab equipment

REFERENCES

and beyond. In addition, I also thank all the members of the Wegener group for their support and inspirations.

Finally, I wish to express my utmost thanks to all my friends, the members of my family, as well as my girl-friend Andrea for their continuing love and support over the years.